National Library of Canada
Acquisitions and Bibliographic Services Branch
395 Wellington Street
Ottawa, Ontario
K1A 0N4

Bibliothèque nationale du Canada
Direction des acquisitions et des services bibliographiques
395, rue Wellington
Ottawa (Ontario)
K1A 0N4

Your file Votre référence

Our file Notre référence

NOTICE

The quality of this microform is heavily dependent upon the quality of the original thesis submitted for microfilming. Every effort has been made to ensure the highest quality of reproduction possible.

If pages are missing, contact the university which granted the degree.

Some pages may have indistinct print especially if the original pages were typed with a poor typewriter ribbon or if the university sent us an inferior photocopy.

Reproduction in full or in part of this microform is governed by the Canadian Copyright Act, R.S.C. 1970, c. C-30, and subsequent amendments.

AVIS

La qualité de cette microforme dépend grandement de la qualité de la thèse soumise au microfilmage. Nous avons tout fait pour assurer une qualité supérieure de reproduction.

S'il manque des pages, veuillez communiquer avec l'université qui a conféré le grade.

La qualité d'impression de certaines pages peut laisser à désirer, surtout si les pages originales ont été dactylographiées à l'aide d'un ruban usé ou si l'université nous a fait parvenir une photocopie de qualité inférieure.

La reproduction, même partielle, de cette microforme est soumise à la Loi canadienne sur le droit d'auteur, SRC 1970, c. C-30, et ses amendements subséquents.

Canada

UNIVERSITY OF ALBERTA

SIMULATION OF COMPOUND SEMICONDUCTOR HETEROSTRUCTURE BIPOLAR DEVICES

by

WILLIAM CAMERON RUTHERFORD

©

A THESIS SUBMITTED TO
THE FACULTY OF GRADUATE STUDIES AND RESEARCH
IN PARTIAL FULFILLMENT OF THE REQUIREMENTS FOR THE
DEGREE OF
DOCTOR OF PHILOSOPHY

DEPARTMENT OF ELECTRICAL ENGINEERING

EDMONTON, ALBERTA

SPRING, 1995

National Library
of Canada

Acquisitions and
Bibliographic Services Branch

395 Wellington Street
Ottawa, Ontario
K1A 0N4

Bibliothèque nationale
du Canada

Direction des acquisitions et
des services bibliographiques

395, rue Wellington
Ottawa (Ontario)
K1A 0N4

Your file Votre référence

Our file Notre référence

THE AUTHOR HAS GRANTED AN IRREVOCABLE NON-EXCLUSIVE LICENCE ALLOWING THE NATIONAL LIBRARY OF CANADA TO REPRODUCE, LOAN, DISTRIBUTE OR SELL COPIES OF HIS/HER THESIS BY ANY MEANS AND IN ANY FORM OR FORMAT, MAKING THIS THESIS AVAILABLE TO INTERESTED PERSONS.

L'AUTEUR A ACCORDE UNE LICENCE IRREVOCABLE ET NON EXCLUSIVE PERMETTANT A LA BIBLIOTHEQUE NATIONALE DU CANADA DE REPRODUIRE, PRETER, DISTRIBUER OU VENDRE DES COPIES DE SA THESE DE QUELQUE MANIERE ET SOUS QUELQUE FORME QUE CE SOIT POUR METTRE DES EXEMPLAIRES DE CETTE THESE A LA DISPOSITION DES PERSONNE INTERESSEES.

THE AUTHOR RETAINS OWNERSHIP OF THE COPYRIGHT IN HIS/HER THESIS. NEITHER THE THESIS NOR SUBSTANTIAL EXTRACTS FROM IT MAY BE PRINTED OR OTHERWISE REPRODUCED WITHOUT HIS/HER PERMISSION.

L'AUTEUR CONSERVE LA PROPRIETE DU DROIT D'AUTEUR QUI PROTEGE SA THESE. NI LA THESE NI DES EXTRAITS SUBSTANTIELS DE CELLE-CI NE DOIVENT ETRE IMPRIMES OU AUTREMENT REPRODUITS SANS SON AUTORISATION.

ISBN 0-612-01756-7

Canada

UNIVERSITY OF ALBERTA

RELEASE FORM

NAME OF AUTHOR: **WILLIAM CAMERON RUTHERFORD**

TITLE OF THESIS: **SIMULATION OF COMPOUND SEMICONDUCTOR HETEROSTRUCTURE BIPOLAR DEVICES**

DEGREE: **DOCTOR OF PHILOSOPHY**

YEAR THIS DEGREE GRANTED: **1995**

PERMISSION IS HEREBY GRANTED TO THE UNIVERSITY OF ALBERTA LIBRARY TO REPRODUCE SINGLE COPIES OF THIS THESIS AND TO LEND OR SELL SUCH COPIES FOR NON-PROFIT RESEARCH PURPOSES ONLY.

THE AUTHOR RESERVES OTHER PUBLICATION RIGHTS, AND NEITHER THE THESIS NOR EXTENSIVE EXTRACTS FROM IT MAY BE PRINTED OR OTHERWISE REPRODUCED WITHOUT THE AUTHOR'S WRITTEN PERMISSION.

W. Rutherford

WILLIAM CAMERON RUTHERFORD

Dated: January 30, 95

UNIVERSITY OF ALBERTA

FACULTY OF GRADUATE STUDIES AND RESEARCH

THE UNDERSIGNED CERTIFY THAT THEY HAVE READ, AND RECOMMEND TO THE FACULTY OF GRADUATE STUDIES AND RESEARCH FOR ACCEPTANCE, A THESIS ENTITLED **SIMULATION OF COMPOUND SEMICONDUCTOR HETEROSTRUCTURE BIPOLAR DEVICES** SUBMITTED BY **WILLIAM CAMERON RUTHERFORD** IN PARTIAL FULFILLMENT OF THE REQUIREMENTS FOR THE **DEGREE OF DOCTOR OF PHILOSOPHY**.

Dr. Igor M. Filanovsky

Dr. Fred D. Otto

Dr. Doug G. Ivey

Dr. Michael S. Shur

Dr. Ronald P. W. Lawson

Dr. Peter R. Smy

Dr. R. Ian MacDonald

Dr. Keith A. Stromsmoe

Dated: 9 Jan 1995

Dedicated to

Dr. Alexander Cameron Rutherford

ABSTRACT

This describes a new model of the heterostructure emitter bipolar transistor (HEBT). The simulation techniques are used for predicting device optimization for analog circuit design. The required approximations are achieved by use of parameterized one dimensional hydrodynamic descriptions of the intrinsic region combined with thermionic emission junction transport. The relative performance of the n-npn and p-pnp HEBT is evaluated by equivalent model comparison in terms of current gain and cut off frequency. A fabricated n-npn HEBT is simulated and its cutoff frequency and gain bandwidth product compared to a graded emitter HBT with equivalent parameters. Some discussion as to future research directions is also included.

ACKNOWLEDGEMENTS

The author would like to express his gratitude to Dr. Igor Filanovsky, for helping to set the direction of this research work and also for providing continuous guidance and motivation.

The author would also like to acknowledge the assistance of the committee members for helping to form the final version of this document and Lexmark Canada Inc. for the use of a laser printer to print it.

TABLE OF CONTENTS

Chapter			Page
1.	INTRODUCTION		1
	1.1	Cutoff Frequency of GaAs HBT, Si BJT, GaAs MESFET and GaAs HEMT	3
	1.2	Potential Applications, History and Topology Overview	9
	1.3	$Al_xGa_{1-x}As$ vs. Silicon Properties Overview	16
	1.4	Analysis of a Bandgap Graded $Al_xGa_{1-x}As$ Base	27
	1.5	$Al_xGa_{1-x}As$ Junction Types and Diffusion Potentials	41
	1.6	Section Summary	43
2.	REVIEW AND MODEL DEVELOPMENT		46
	2.1	Recombination Currents	47
	2.2	Dopant Band Gap Narrowing	57
	2.3	Lateral Resistance Components	60
	2.4	Junction Capacitance Components	68
	2.5	Junction Voltages	71

	2.6	Emitter Charging Time	74
	2.7	Base Transit Time	77
	2.8	Collector Transit Time	80
	2.9	Cutoff Frequency	81
	2.10	Maximum Frequency of Oscillation	83
	2.11	Section Summary	85
3.	RESULTS AND DISCUSSION		88
	3.1	The HEBT Design Philosophy	92
	3.2	The HEBT Model	93
	3.3	Heterostructure Emitter Small Signal Model	113
	3.4	Comparison with HEBT Experimental Data	122
	3.5	HEBT vs. HBT Cut Off Frequency and Gain Bandwidth Comparison	125
4.	CONCLUSIONS		127
	4.1	Future Research Directions	128
	REFERENCES		129

LIST OF FIGURES

Figure		Page
1.1	Estimated maximum collector current density for the GaAs and Si bipolar devices with an assumed base collector scr width of 200 nm and voltage drop of 1 volt as a function of electron concentration.	7
1.2	Estimated cutoff frequency of GaAs based MESFET and HEMT compared to GaAs HBTs and a Si BJT as a function of gate and base width at 300 K. An assumed J_c of 10^9 amp-cm^{-2} is used with a base / channel dopant level of 10^{17} cm^{-3} and an assumed 20 nm emitter base space charge region with a 200 nm base collector space charge region with a 1 volt drop.	8
1.3	Schematic cross section of an emitter up $Al_xGa_{1-x}As$ HBT configuration	10
1.4	Schematic cross section of a collector up $Al_xGa_{1-x}As$ HBT configuration	11
1.5	Schematic energy band diagram for a npn emitter up $Al_xGa_{1-x}As$ HBT	12
1.6	$Al_xGa_{1-x}As$ HBT differential test circuit for a test wafer	14
1.7	Overview of the production process	15
1.8	$Al_xGa_{1-x}As$ grade within emitter space charge region and base region	16
1.9	Plot of the main $Al_xGa_{1-x}As$ energy minima as a function of alloy fraction x at 300 K with Si for reference	18

1.10	Plot of the main energy minima as a function of temperature for $Al_xGa_{1-x}As$ at x = 0.3 with Si for reference	19
1.11	Plot of normalized minima effective mass as a function of x for $Al_xGa_{1-x}As$ with Si for reference	20
1.12	Normalized $Al_xGa_{1-x}As$ energy minima thermal equilibrium occupation factors as a function of x at 300 K	23
1.13	$Al_xGa_{1-x}As$ average density of states thermal equilibrium effective mass ratio as a function of x at 300 and 500 K with the 300 K Si value for reference	24
1.14	$Al_xGa_{1-x}As$ intrinsic carrier population as a function of lattice temperature at x = 0 and 0.3 with Si for reference	26
1.15	$Al_xGa_{1-x}As$ graded base built in electric field for a 100 nm wide base at T = 300 K as a function of alloy fraction at the emitter side assuming x = 0 at the collector side	29
1.16	$Al_xGa_{1-x}As$ vs. Si low electric field electron mobility estimates for x = 0 and 0.05 at T = 300 and 500 K as a function of acceptor ion concentration	32
1.17	$Al_xGa_{1-x}As$ and Si electron mobility estimate for $N_I = 10^{19}$ cm^{-3} and T = 500 K as a function of x	33
1.18	$Al_xGa_{1-x}As$ and Si low field electron mobility estimate for x = 0.05 and 0.15 with $N_I = 10^{19}$ cm^{-3} as a function of temperature	33
1.19	$Al_xGa_{1-x}As$ and Si electron lifetime estimate for x = 0 and T = 300 K as a function of base acceptor ion concentration assumed as equivalent to traps	34

1.20	The electron concentration for a 100 nm wide p-type base as a function of distance from the emitter base scr edge with x_{bo} = 0, 0.15 and 0.3 using $N_b = 10^{18}$ cm^{-3}	39
1.21	The ratio of electron content for a 100 nm wide p-type $Al_xGa_{1-x}As$ base with increasing alloy grade x with respect to the value at x = 0	39
1.22	Current density components for a 100 nm wide p-type $Al_xGa_{1-x}As$ base as a function of increasing alloy content with Si for reference. Parameters are the same as for figures 1.20 and 1.21	40
1.23	Diffusion potential of the $Al_xGa_{1-x}As$ and Si heterotype junctions as a function of increasing alloy fraction x with an acceptor level of 10^{19} and donor level of 10^{18} cm^{-3} at 300 K	42
1.24	Diffusion potential of the $Al_xGa_{1-x}As$ isotype heterojunction with a narrow gap alloy fraction of zero and a wide gap ion level of 10^{18} and 10^{19} cm^{-3}, as a function of increasing wide gap alloy fraction x at 300 K	43
2.1	Schematic view of HBT major recombination currents	47
2.2	Approximate $Al_xGa_{1-x}As$ surface and junction depletion width as a function of dopant ion concentration with worst case and 20% occupancy surface charge	50
2.3	Illustrative cut away of an $Al_xGa_{1-x}As$ HBT showing surface and junction depletion regions and surface depletion layer channeling currents	51
2.4	Theoretical base quasi-neutral layer recombination current densities compared to a parametric fit as a function of emitter base voltage assuming a base width of 100 nm and base quasi neutral region width of 90 nm	56

2.5	Empirical band gap narrowing approximation at 300 K for GaAs and Si	58
2.6	Empirical ionization energy approximation at 300 K for $Al_xGa_{1-x}As$ as a function of alloy fraction x	59
2.7	Semiconductor layer sheet resistance approximation for p and n type at a doping level of 10^{19} cm^{-3} as a function of layer width at 300 K	60
2.8	Schematic diagram of distributed base resistance and collector capacitance	61
2.9	Base layer sheet resistance components for p and n type at as a function of lateral distance with zero base alloy content at 300 K	67
2.10	Theoretical emitter base voltage for npn and pnp devices as a function of current density at 300 K with x = 0.3 for HBTs and 0 for GaAs BJTs in the emitter and zero base alloy with the same doping parameters as figure 2.9	72
2.11	Theoretical emitter charging time for npn and pnp devices as a function of current density at 300 K with x = 0.3 and 0 in the emitter and zero base alloy with the same doping parameters as figure 2.10	76
2.12	Theoretical delay components for npn and pnp devices with zero base field as a function of base width using $N_c = 10^{17}$ cm^{-3} and equivalent parameters to figures 2.9 to 2.11	78
2.13	Theoretical delay components for npn and pnp devices with zero base field as a function of base collector voltage using $N_c = 10^{17}$ cm^{-3} and equivalent parameters of figures 2.9 to 2.12	80

2.14	Theoretical f_t for npn and pnp devices with zero base field as a function of base width at $V_{bc} = 0$ volt and with equivalent parameters to figures 2.9 to 2.13	82
2.15	Theoretical f_{max} for npn and pnp devices with zero base field as a function of base width at $V_{bc} = 0$ and with equivalent parameters to figures 2.9 to 2.14	84
3.1	Illustrative band diagram showing movement of the conduction band peak back into the emitter scr and down in energy with the emitter alloy grade	88
3.2	Illustrative plot of graded and abrupt HBT I_c vs. V_{be} for several test devices on two different wafers at several points across the wafer	89
3.3	Scanning ion mass spectrometry plot of a Beryllium out diffusion profile for a dopant graded base	91
3.4	Schematic npn HEBT band diagram of the isotype heterojunction confinement emitter with an alloy graded base	93
3.5	J_{che0} for n-n and p-p isotype heterojunctions with twice the heterolayer dopant level as emitter dopant level vs. heterolayer alloy fraction x with an emitter alloy fraction of zero and dopant level of 10^{18} cm^{-3} at 300 K	103
3.6	V_{he} for n-n and p-p isotype heterojunctions with a J_{che0} corresponding to figure 3.5 values locked at an x value of 0.2 vs. majority carrier current density at 300 K and with other parameters as in figure 3.5	104

3.7	Valence and conduction band energy barrier height for n-npn and p-pnp HEBT isotype heterojunction steps with a J_{che} of 10^5 amp per cm^2 vs. heterolayer alloy content x with zero emitter alloy content and 2:1 heterolayer to emitter doping at 300 K	105
3.8	Assumed minority carrier concentration at emitter scr edge as a function of majority current density for n-npn and p-pnp devices at 300 K	106
3.9	Estimated emitter quasi-neutral region width with w_e assumed as 200 nm as a function of majority current density for n-npn and p-pnp devices with N_e of 10^{18} cm^{-3} at 300 K	108
3.10	Estimated minority carrier distributions in the emitter quasi-neutral region as a function of displacement from the emitter scr edge (z = 0 nm) with w_e assumed as 200 nm and majority current assumed as 10^5 amp/cm^2 for n-npn and p-pnp devices with N_e of 10^{18} cm^{-3} at 300 K	109
3.11	Estimated thermal emission current density at ($z = w_{eqn}$) as a function of x_h with w_e assumed as 200 nm and majority current assumed as 10^5 amp/cm^2 for n-npn and p-pnp devices with N_e of 10^{18} cm^{-3} and N_h of 2×10^{18} cm^{-3} at 300 K	110
3.12	Estimated current gain as a function of x_h with w_e assumed as 200 nm and majority current assumed as 10^5 amp/cm^2 for n-npn and p-pnp devices with N_e of 10^{18} cm^{-3} and N_h of 2×10^{18} cm^{-3} at 300 K	111
3.13	Small signal lumped element model of the heterostructure emitter	112

3.14 Estimated small signal effective resistance as a function of majority carrier current density for n-npn and p-pnp devices with heterolayer alloy $x_h = 0.2$ and $x_e = 0$ with N_e of 10^{18} cm^{-3} and N_h of 2×10^{18} cm^{-3} at 300 K 114

3.15 Estimated small signal effective resistance for n-npn and p-pnp devices as a function of heterolayer alloy fraction (x_h) with $J_{c\_he} = 10^5$ amp/cm^2 and $x_e = 0$ with N_e of 10^{18} cm^{-3} and N_h of 2×10^{18} cm^{-3} at 300 K 114

3.16 Estimated depletion ($V_{\beta h}$) and accumulation ($V_{\beta e}$) voltage drops for n-npn and p-pnp devices as a function of forward bias (V_{he}) with heterolayer alloy $x_h = 0.2$ and $x_e = 0$ with N_e of 10^{18} cm^{-3} and N_h of 2×10^{18} cm^{-3} at 300 K 115

3.17 Estimated isotype heterojunction capacitance for n-npn and p-pnp devices as a function of heterolayer alloy fraction at a majority carrier current density (J_{c_he}) of 10^5 amp/cm^2 with heterolayer alloy $x_h = 0.2$ and $x_e = 0$ with N_e of 10^{18} cm^{-3} and N_h of 2×10^{18} cm^{-3} at 300 K 117

3.18 Estimated isotype heterojunction capacitance for n-npn and p-pnp devices as a function of majority carrier current density (J_{c_he}) with heterolayer alloy $x_h = 0.2$ and $x_e = 0$ with N_e of 10^{18} cm^{-3} and N_h of 2×10^{18} cm^{-3} at 300 K 117

3.19 Estimated emitter cut off frequency for n-npn and p-pnp devices as a function of majority carrier current density (J_{c_he}) with $V_{bc} = 0$ volts heterolayer alloy $x_h = 0.2$ and $x_e = 0$ with N_e of 10^{18} cm^{-3} and N_h of 2×10^{18} cm^{-3} at 300 K 118

3.20 Estimated emitter cut off frequency for n-npn and p-pnp devices as a function of heterolayer alloy fraction (x_h) with $J_{c\_he} = 10^5$ amp/cm^2 and $V_{bc} = 0$ volts, $x_e = 0$ with N_e of 10^{18} cm^{-3} and N_h of 2×10^{18} cm^{-3} at 300 K 119

3.21 Estimated emitter cut off frequency for n-npn and p-pnp devices as a function of heterolayer doping (N_h) with $J_{c\_he} = 10^5$ amp/cm^2 and $V_{bc} = 0$ volts, $x_e = 0$ with N_e of 10^{18} cm^{-3} at 300 K 120

3.22 Estimated emitter gain bandwidth product for n-npn and p-pnp devices as a function of heterolayer alloy fraction (x_h) with $J_{c\_he} = 10^5$ amp/cm^2 and $V_{bc} = 0$ volts, $x_e = 0$ with N_e of 10^{18} cm^{-3} and N_h of 2×10^{18} cm^{-3} at 300 K. 121

3.23 Estimated current gain for n-npn simulated and large area passivated experimental devices as a function of collector current density using $V_{bc} = 0$ volts, $x_e = 0$ with N_e of 5×10^{17} cm^{-3} at 300 K. 122

3.24 Estimated current density components for the simulated experimental n-npn HEBT of figure 3.23 as a function of collector current density. 123

3.25 Estimated junction capacitances for the experimental HEBT and equivalent HBT devices of figures 3.22 and 3.23. 125

3.26 Estimated cut off frequency for equivalent HBT and simulated experimental HEBT devices as a function of collector current density with $V_{bc} = 0$ volts at 300 K. 126

3.27 Estimated gain bandwidth products for experimental n-npn HEBT device and an equivalent HBT as a function of collector current density with $V_{bc} = 0$ volts at 300 K. 126

LIST OF ABBREVIATIONS AND SYMBOLS

2kT	ideality of 2
AlAs	aluminium arsenide
$Al_xGa_{1-x}As$	aluminium gallium arsenide with alloy fraction x
Be	beryllium
BJT	bipolar junction transistor
DDE	drift diffusion equation
EB	emitter base
FET	field effect transistor
GaAs	gallium arsenide
HBT	heterojunction bipolar transistor
HEBT	heterostructure emitter bipolar transistor
HEMT	high electron mobility transistor (FET)
HLM	Henry, Logan and Merritt
kT	unity ideality
LDS	large dark spot
MBE	molecular beam epitaxy
MESFET	metal semiconductor FET

MTTF	mean time to failure
scr	space charge region
Si	silicon
SIMS	scanning ion mass spectrometer
SRH	Schockley, Read and Hall

Symbol	Units	Description
α		mobility reduction factor
α_c		conduction band offset factor
α_{cg}		factor for reducing graded conduction band barrier
α_{eb}		ratio factor for self aligned base
α_v		valence band offset factor
A_n	$\frac{cm^6}{s}$	Auger electron recombination coefficient
A_p	$\frac{cm^6}{s}$	Auger hole recombination coefficient
A_R	$\frac{amp}{cm^2 \cdot K^2}$	Richardson constant
B_R	$\frac{cm^3}{s}$	radiative recombination coefficient
β		d.c. current gain

C_{cb}	$\frac{fF}{\mu m^2}$	base collector depletion capacitance
C_{eb}	$\frac{fF}{\mu m^2}$	emitter base depletion capacitance
C_{he}	$\frac{fF}{\mu m^2}$	isotype heterojunction capacitance
C_{scr}	$\frac{fF}{\mu m^2}$	space charge region capacitance
D_p	$\frac{cm^2}{s}$	diffusion constant for holes
D_n	$\frac{cm^2}{s}$	diffusion constant for electrons
δ_{xhe}		heterolayer to emitter alloy molar increment
ε	$\frac{F}{m}$	dielectric constant
E_{gbo}	eV	bandgap at the emitter edge of the base
E_{gbw}	eV	bandgap at the collector edge of the base
E_{ge}	eV	bandgap in the emitter
E_{gh}	eV	bandgap in the emitter heterolayer
E_i	eV	intrinsic energy level
E_{th}	eV	thermal energy

E_{Fp}	eV	hole quasi-Fermi level
E_c	eV	conduction band energy
E_Γ	eV	Γ conduction band energy
E_X	eV	X conduction band energy
E_L	eV	L conduction band energy
E_v	eV	valence band energy
ΔE_{va}	eV	effective valence energy barrier
ΔE_{vbgn}	eV	valence band narrowing offset in the base
η		exponential characteristic ideality factor
f_{max}	GHz	maximum frequency of oscillation
f_t	GHz	cut off frequency
F_z	$\frac{volt}{cm}$	electric field component along z axis
F_m	$\frac{volt}{cm}$	maximum electric field for velocity saturation
J	$\frac{amp}{cm^2}$	current density
J_{2kT}	$\frac{amp}{cm^2}$	near ideality 2 current density

J_{pbe_hbt}	$\frac{amp}{cm^2}$	hole thermionic emission current density from HBT base to emitter
J_{peh}	$\frac{amp}{cm^2}$	hole thermionic emission current density from emitter to heterolayer
J_{pehs}	$\frac{amp}{cm^2}$	surface recombination current density at heterolayer
J_c	$\frac{amp}{cm^2}$	collector current density
J_{he0}	$\frac{amp}{cm^2}$	isotype heterojunction saturation current
J_{rb}	$\frac{amp}{cm^2}$	base bulk recombination current density
J_{re}	$\frac{amp}{cm^2}$	emitter bulk recombination current density
κ	$eV \cdot cm^{1.5}$	valence band narrowing proportionality constant
$\kappa_{\Gamma L}$	$\frac{volt}{cm \cdot eV}$	critical field adjustment factor
L_{DS}	nm	drain to source length
L_E	nm	effective emitter length
L_G	nm	effective gate length
L_{slice}	um	length of a standard emitter finger section
m_0	kg	electron free space rest mass

m_{Γ}	kg	electron effective mass in the Γ minima
m_{hh_AlAs}	kg	AlAs heavy hole effective mass
m_{hh_GaAs}	kg	GaAs heavy hole effective mass
m_{L}	kg	electron effective mass in the L minima
m_{lh_AlAs}	kg	AlAs light hole effective mass
m_{lh_GaAs}	kg	GaAs light hole effective mass
m_{X}	kg	electron effective mass in the X minima
m_{de}	kg	electron density of states effective mass
m_{le}	kg	longitudinal electron effective mass on ellipsoid
m_{te}	kg	transverse electron effective mass on ellipsoid
μ_{i}	$\frac{cm^2}{volt \cdot s}$	ion scattering mobility
μ_{n}	$\frac{cm^2}{volt \cdot s}$	mobility of electons
μ_{no_GaAs}	$\frac{cm^2}{volt \cdot s}$	GaAs intrinsic electron mobility
μ_{no_Si}	$\frac{cm^2}{volt \cdot s}$	silicon intrinsic electron mobility

μ_{no_ld}	$\frac{cm^2}{volt \cdot s}$	low doping temperature adjusted electron mobility
μ_p	$\frac{cm^2}{volt \cdot s}$	mobility of holes
μ_{po_GaAs}	$\frac{cm^2}{volt \cdot s}$	GaAs intrinsic hole mobility
μ_{po_Si}	$\frac{cm^2}{volt \cdot s}$	silicon intrinsic hole mobility
N_b	cm^{-3}	base acceptor density
N_{b_t}	cm^{-2}	total minority carrier charge in the base
n_{bxs}	cm^{-3}	excess electron concentration at the emitter edge of the base
N_c	cm^{-3}	collector ion density
N_{c_Si}	cm^{-3}	energy state density in silicon X minima
N_e	cm^{-3}	emitter ion density
n_e	cm^{-3}	non-equilibrium electron concentration in the emitter
n_{eo}	cm^{-3}	equilibrium electron concentration in the emitter
n_{exs}	cm^{-3}	excess electron concentration at the base edge of the emitter

N_{Γ}	cm^{-3}	energy state density in $Al_xGa_{1-x}As$ Γ minima
N_h	cm^{-3}	heterolayer ion density
n_i	cm^{-3}	intrinsic carrier level
N_L	cm^{-3}	energy state density in $Al_xGa_{1-x}As$ L minima
N_{st}	cm^{-2}	surface trap density per unit area
N_X	cm^{-3}	energy state density in $Al_xGa_{1-x}As$ X minima
v_{dr}	$\frac{cm}{s}$	drift velocity
v_{th}	$\frac{cm}{s}$	average thermal velocity
p_e	cm^{-3}	non-equilibrium hole concentration in the emitter
p_{eo}	cm^{-3}	equilibrium hole concentration in the emitter
p_{exs}	cm^{-3}	excess hole concentration at the base edge of the emitter
Ψ_e		normalized potential for emitter half of isotype heterojunction
Ψ_{he}		normalized potential drop for isotype heterojunction
q	C	elementary charge

r_e	$\Omega\,cm^2$	effective resistance of the emitter base energy barrier
r_h	$\Omega\,cm^2$	effective resistance of the heterolayer emitter energy barrier
S_h	$\frac{cm}{s}$	total effective surface recombination velocity at a heterolayer
S_{he}	$\frac{cm}{s}$	surface recombination velocity at a heterolayer due to emission
S_{hs}	$\frac{cm}{s}$	surface recombination velocity at a heterolayer due to trapping
σ_β		standard deviation of d.c. current gain in a sample of bipolar devices
σ_n	cm^2	electron capture cross section
σ_{offset}		standard deviation of offset voltage in a sample of devices
σ_p	cm^2	hole capture cross section
T	K	temperature above absolute zero
T_r	K	reference temperature of 300 K
τ_b	ns	base transit time
τ_e	ns	emitter charging time
τ_{ec}	ns	emitter to collector transit time

τ_n	ns	minority electron average lifetime
τ_p	ns	minority hole average lifetime
τ_{sc}	ns	collector space charge region transit time
V_{α_Si}	volt	silicon heterotype homojunction diffusion potential
V_{α_x}	volt	$Al_xGa_{1-x}As$ heterotype homojunction diffusion potential
V_{β}	volt	$Al_xGa_{1-x}As$ heterotype heterojunction diffusion potential
V_{γ}	volt	$Al_xGa_{1-x}As$ isotype heterojunction diffusion potential
V_{bc}	volt	applied voltage across a base collector junction
V_{bi_he}	volt	built in voltage of a emitter isotype heterojunction
V_{eb}	volt	applied voltage across the emitter base
V_{he}	volt	applied voltage across the emitter isotype heterojunction
V_{offset}	volt	offset voltage between devices in a differential pair
V_{th}	volt	thermal voltage
w_b	nm	metallurgical base width

w_{bcd}	nm	base collector depletion width
w_{bqn}	nm	quasi-neutral base width
w_{cbd}	nm	collector base depletion width
w_{e}	nm	metallurgical emitter width
w_{ebd}	nm	emitter base depletion width
w_{eqn}	nm	quasi-neutral emitter width
x_{bo}		alloy molar fraction at the emitter edge of the base
x_{bw}		alloy molar fraction at the collector edge of the base
x_{c}		alloy molar fraction in the collector
x_{e}		alloy molar fraction in the emitter
x_{h}		alloy molar fraction in the emitter heterolayer
z	nm	z axis coordinate

Note: The equations in this document use parameterization variables which are directly substituted, or passed on to previously defined equations. Further information can be obtained from MathSoft Inc., 101 Main Street, Cambridge, MA 02142.

Chapter 1

INTRODUCTION

This section gives an overview of the relative position of the work in later sections on $Al_xGa_{1-x}As$ bipolar devices with respect to other technologies and some emerging applications. As the frequency performance of competing devices is often considered the prime indicator of relative application possibilities, a rough estimate of the cutoff frequency of the $Al_xGa_{1-x}As$ HBT, Si BJT, GaAs MESFET and HEMT is formulated, indicating possible positioning of the three technologies. Consideration is then made of potential target applications, possible alternate semiconductor systems for the bipolar approach followed by the history, topology considerations, analog circuit fabrication results and an overview of the simulation and fabrication optimization. As $Al_xGa_{1-x}As$ is used in the context of bandgap manipulation throughout the rest of this work, a brief overview of $Al_xGa_{1-x}As$ properties contrasted with silicon are included. This is followed by their use in the analysis of a bandgap graded base, used in later sections, and elucidating some of the possibilities of this technology as applied to bipolar devices. Finally, a brief overview of the four junction types possible in bandgap engineered bipolar devices is presented, with their relative diffusion potentials.

From the perspective of recent compound semiconductor research the use of bandgap engineered bipolar transistors for high performance analog circuits [1] is a promising area of application [2]. The main competition has been from Si bipolar transistors [3] and more recently from Metal Semiconductor Field Effect Transistors [4] [5], neither of

which are able to address some of the emerging high performance analog applications as effectively [1]. From the theoretical perspective, which is the main concern of the current work, compound semiconductor and silicon based heterojunction and homojunction bipolar devices share similarities and differences impacting the design of analog circuits. Briefly, the ideal analog switch similar to other electronic device abstractions would have infinite input impedance, bandwidth and gain, along with linear response, zero offset and other idealized parameters. Of primary significance is the fact that the forward transconductance of these devices has the same exponential characteristic. However, a closer look at device characteristics indicates that the compound semiconductor bipolar devices, represented here by GaAs, may have lower transit times and resistances than Si devices, which translates to a significant frequency advantage. It is also of significance that the compound semiconductor devices have a much higher Early voltage [2], which is a measure of device linearity, and are also able to operate at a higher temperature [6] than Si devices. The junction capacitance of Si and compound semiconductor devices is similar in magnitude, but, the latter grown on semi-insulating substrates has negligible collector to substrate capacitance and with wafer thinning [5] can be used for controlled impedance microwave microstrip designs. GaAs MESFET circuits, while more attractive for high frequency applications than Si based devices, have relatively poor dc and low frequency characteristics [7], likely making the bipolar compound semiconductor devices a better choice for high performance wideband analog applications [1]. The overall scope of this work is to investigate $Al_xGa_{1-x}As$ based bipolar device architecture with respect to prioritized parameters for use in high performance wideband analog circuits. Additionally, this work is motivated in part by the

relatively recent successful fabrication of the simpler unipolar compound semiconductor GaAs MESFETs for high performance microwave, digital and analog service.

1.1 Cutoff Frequency of GaAs HBT, Si BJT, GaAs MESFET and GaAs HEMT

As compound semiconductor MESFET devices are a primary competitor in the high frequency domain and currently are the most widely manufactured of the GaAs transistor devices, priority is initially given to a basic comparison of frequency performance. One of the advantages that epitaxial bipolar devices may have, compared to FET devices, is the definition of the size-critical region in the vertical domain as opposed to the horizontal domain, which is favorable from the fabrication perspective. The cutoff frequency for a MESFET [8] can be approximated by arbitrarily assuming a GaAs n-type channel, with doping such that the effective channel drift mobility(μ_{nc}) is proportional to the intrinsic mobility, due to scattering using

$$\mu_{nc} = \alpha \cdot \mu_{no} \tag{1.1}$$

The average electric field in the channel(F_{xc}) acting on the electron can be approximated by assuming

$$F_{xc} = \frac{V_{DS}}{l_{DS}} \tag{1.2}$$

where D stands for drain, S for source and L_{DS} is the separation . The maximum average velocity of the electrons can be estimated as

$$v_m = \mu_{nc} \cdot F_m \tag{1.3}$$

where average drift velocity is limited by scattering at field threshold electric field F_m and can be approximated after [9] by

$$v_{dr} = \mu_{nc} \cdot F_{xc}(V_{DS}, L_{DS}) \cdot \left(1 + \frac{\mu_{nc} \cdot F_{xc}(V_{DS}, L_{DS})}{v_m(\mu_{nc})}\right)^{-1} \tag{1.4}$$

τ_{ct} is the effective channel transit time which can be estimated using the ratio of the distance traveled by an electron under the gate divided by the average drift velocity of the electron

$$\tau_{ct} = \frac{L_G}{v_{dr}(\mu_{nc}, V_{DS}, L_{DS})} \tag{1.5}$$

which gives the well known cutoff frequency as

$$f_{t\_FET} = \frac{1}{2 \cdot \pi \cdot \tau_{ct}(\mu_{nc}, V_{DS}, L_{DS}, L_G)} \tag{1.6}$$

Assuming a range for the FET gate metal length down to 0.05 μm with a self aligned source and drain contact with relational constant

$$\lambda_{DS}=5 \tag{1.7}$$

such that the source drain spacing is indexed to the gate length then

$$L_{DS}=\lambda_{DS}\cdot L_G \tag{1.8}$$

the approximate cut off frequency of the MESFET is roughly estimated as a function of gate length.

The bipolar device base transit time similarly to the MESFET channel transit time is determined by the rate at which the charge carrier particles present could be cleared out of the base layer which is proportional to the number in the base divided by the flow rate out giving

$$\tau_b=q\frac{n_b\cdot w_b}{J_c} \tag{1.9}$$

The emitter base junction represents a resistive energy barrier in per unit area terms charging both collector and emitter space charge regions implying

$$r_e=\frac{V_{th}(T_r)}{J_c} \tag{1.10}$$

combined with a charge separation layer (space charge region)

$$C_{scr} = \frac{\varepsilon}{w_{scr}} \tag{1.11}$$

which gives an effective emitter time constant

$$\tau_e = \tau_e\left(J_c\right) \cdot \left(C_{scr}\left(\varepsilon, w_{ebd}\right) + C_{scr}\left(\varepsilon, w_{bcd}\right)\right) \tag{1.12}$$

Assuming the collector space charge region is traversed at an average drift velocity twice that of the steady state drift velocity

$$\tau_{sc} = \frac{w_{bcd}}{2 \cdot v_{dr}\left(\mu_{nc}, V_{bcd}, w_{bcd}\right)} \tag{1.13}$$

and totaling the contributions

$$\tau_{ec} = \tau_e\left(J_c, \varepsilon, w_{ebd}, w_{bcd}\right) + \tau_b\left(J_c, w_b, n_b\right) + \tau_{sc}\left(\mu_{nc}, w_{bcd}, V_{bcd}\right) \tag{1.14}$$

similarly the cutoff frequency can be approximated as

$$f_{t\_BT} = \frac{1}{2 \cdot \pi \cdot \tau_{ec}\left(J_c, \varepsilon, \mu_{nc}, w_{ebd}, w_{bcd}, w_b, n_b, V_{bcd}\right)} \tag{1.15}$$

If frequency response is the main concern regardless of power consumption the maximum collector current density can be estimated as the maximum density of electrons times the average drift velocity in the collector space charge region

$$J_{c\_max} = q \cdot n_{max} \cdot v_{dr} \qquad (1.16)$$

From the perspective of direct comparison with FET devices the channel doping is assumed to be 10^{17} per cm^3 implying an equivalent maximum electron density in the collector space charge region of the HBT corresponding to about 10^5 amps per cm^2 in figure 1.1.

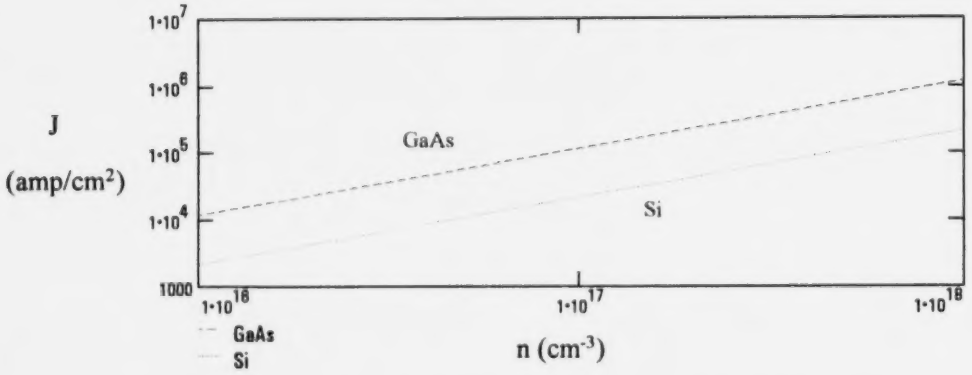

Figure 1.1: Estimated maximum collector current density for the GaAs and Si bipolar devices with an assumed base collector scr width of 200 nm and voltage drop of 1 volt as a function of electron concentration.

As the HBT does not exhibit as severe a high injection f_t rolloff as Si devices the device biasing is thermally limited [1] implying wafer thinning to compensate for the factor of three higher GaAs thermal resistance. Also circuit thermal transient / proximity analysis,

high temperature (>450 K) optimization modeling and worst case design analysis should include the negative temperature coefficient of β for GaAs HBT vs. positive coefficient for Si BJT [1].

In figure 1.2 the average HEMT electron mobility is assumed to be the same as in intrinsic material at 300 K, giving an advantage over the MESFET at the same control length. The HBTs are labeled according to the exponent of their collector current, i.e.. HBT n corresponds to a collector current of 10^n amps/cm^2 .

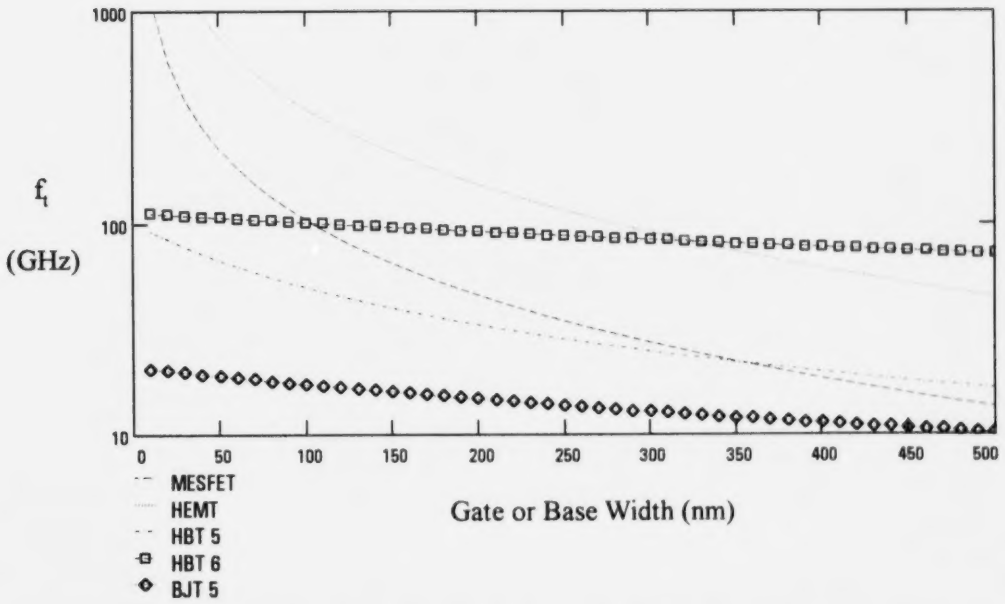

Figure 1.2: Estimated cutoff frequency of GaAs based MESFET and HEMT compared to GaAs HBTs and a Si BJT as a function of gate and base width at 300 K. An assumed J_c of 10^n amp-cm^{-2} is used with a base / channel dopant level of 10^{17} cm^{-3} and an assumed 20 nm emitter base space charge region with a 200 nm base collector space charge region with a 1 volt drop.

From figure 1.2 it is apparent that at high current density the vertical bipolar devices

have frequency parity with MESFET devices, especially in consideration that this may be achieved with relatively less stringent lithography. It should be noted that experimental HBT devices have been operated at current densities in the regime of 10^6 amp-cm^{-2} [2], however it should also be noted that MTTF decreases with temperature increase [1]. The FET channel is limited in cross sectional area orthogonal to current flow by the biasing of the Schottky diode gate for channel pinch off and as such greater wafer surface area, a valuable asset, would likely be necessary for the FET device drain current to match the HBT collector current giving the vertical devices a smaller area for a given circuit and a significant cost benefit advantage.

1.2 **Potential Applications, History and Topology Overview**

The suitability of $Al_xGa_{1-x}As$ for future tasks may depend as much on its optical properties as transport abilities [10]. It is already clear that a high quality production capacity epitaxial growth technology in combination with an easily modified fabrication process [11] will be a minimum investment for research. Notably the other compound semiconductor systems offer some potential improvements over $Al_xGa_{1-x}As$ systems [12] as well as optoelectronic possibilities in 1.3 to 1.55 μm long haul optic fibre [13] applications. However those other systems will likely have a less well supported fabrication infrastructure in the near term.

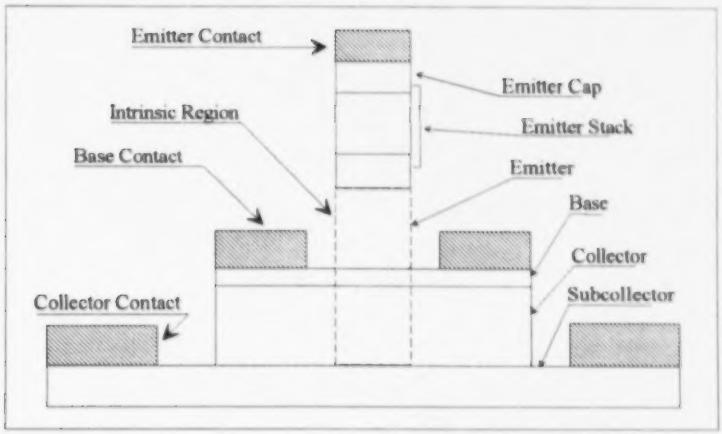

Figure 1.3: Schematic cross section of an emitter up $Al_xGa_{1-x}As$ HBT configuration

The history of the heterojunction bipolar transistor (HBT), figure 1.3, dates back to Shockley [14] and Kroemer [15] in the 1950s, with the concept of an emitter base junction of different (hetero) semiconductor material, which would improve device performance characteristics compared to an equivalent device with the same (homo) junction material. Current work, based on consideration of the original HBT concept from the view of analog circuit requirements combined with consideration of material properties, fabrication requirements and electrical performance, led to an investigation of basic device modifications. Structurally the base and other layers of the HBT are usually formed by crystal growth (epitaxial semiconductor deposition) followed by numerous photolithographic and other process steps such as crystal etching and liftoff forming of evaporated metal alloy contacts. Assuming the epitaxial starting material is flat the intrinsic base layer is adjoined by emitter and collector layers, either of which can be closer to the substrate starting material, with the relative trade off of capacitance vs.

leakage current [16] . In the process of forming contacts, very small areas of semiconductor material are often removed, perhaps by wet chemically selective etching or end point terminated plasma reactive ion etching [17], allowing the metal alloy to form an ohmic contact with the top of a very thin semiconductor layer, such as the base. One of the limitations of the process, therefore, is the etch accuracy across the wafer to form the base contacts, which limits the base layer thickness and/or yield of properly working devices. Referring to the collector up configuration of figure 1.4, collector material rather than emitter material would have to be precisely removed to adequately form an ohmic contact to the top of the base [18]. This process may be one of the major considerations in terms of fabricating devices, however, here we will assume no such liability and continue with theoretical optimizations based on basic idealized intrinsic geometries, assuming the intrinsic region, which includes the emitter, base and collector layers will be laterally defined by the residual surface shape combined with a subsurface isolation strategy. As such, the emitter stack, subcollector and extrinsic base can be thought of as connectors to the intrinsic device, indicated by the dashed outline in figures 1.3 and 1.4.

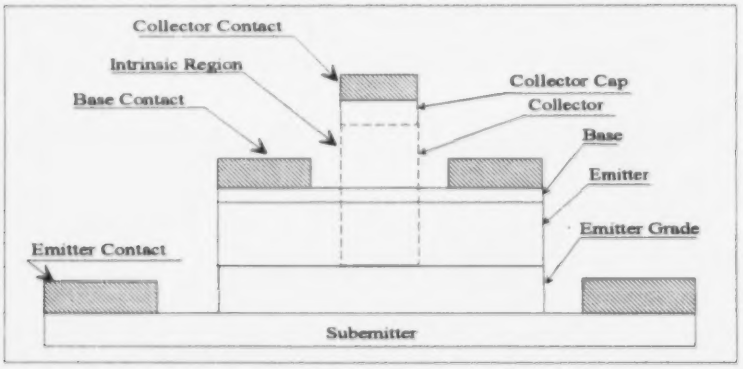

Figure 1.4: Schematic cross section of a collector up $Al_xGa_{1-x}As$ HBT configuration

The optional emitter stack or grade is used to gradually change the material characteristics to the optional emitter or collector cap to provide a predictable and reliable low resistance ohmic path to the contact alloy [2]. Similarly the subcollector or subemitter provides a low resistance path laterally to the semiconductor metal junction. The intrinsic part of the device depicted in figure 1.3 or 1.4 could for example have a wide bandgap n-type $Al_xGa_{1-x}As$ emitter, p-type GaAs base and an n-type GaAs collector as in the idealized device of figure 1.5.

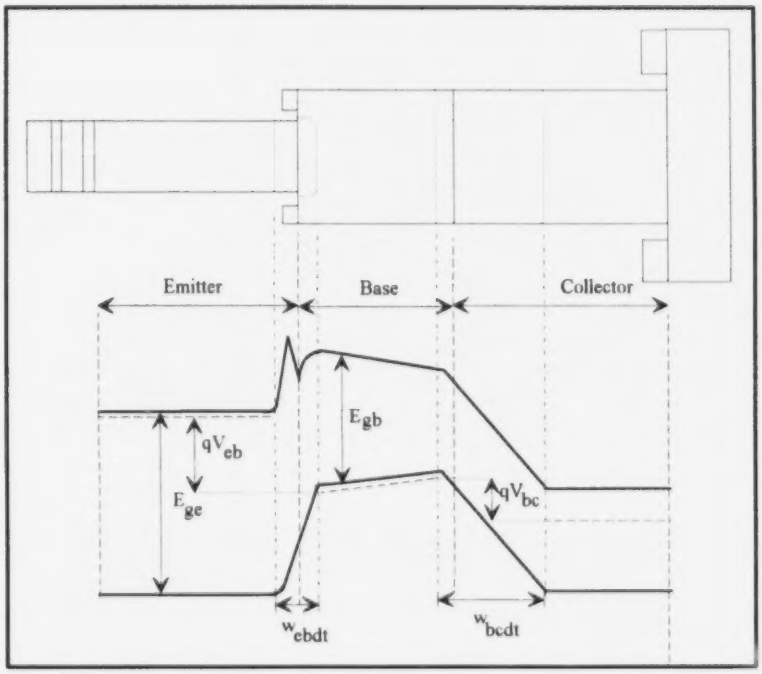

Figure 1.5: Schematic energy band diagram for a npn emitter up $Al_xGa_{1-x}As$ HBT

The HBT of figure 1.5 is shown with the emitter base junction forward biased by an energy level qV_{eb}, such that the average electron energy of the distribution of electron

energies in the emitter is increased by this externally applied bias, disturbing thermal equilibrium. As the emitter base junction bias raises the energy of electrons in the emitter the probability of electron emission over the energy barrier [19] at the junction is exponentially improved. The current density, (minority carriers), entering the base layer is also subject to the availability of appropriate energy states [20] on the target side of the barrier. This process occurs reciprocally with reduced emission in the opposite direction due to path differences. As the theoretical foundations of the HBT are closely related to the silicon bipolar homojunction transistor (BJT) which is widely used in analog circuits a brief synopsis of the relative advantages of the wide gap emitter after [21] are in order and include

- higher emitter efficiency, as minority carriers from the base are blocked by the higher energy barrier in the valence band.
- decreased base resistance as the base can be more heavily doped without sacrificing emitter efficiency.
- less emitter periphery current crowding due to a lower voltage drop along the emitter base junction.
- improved frequency response due to higher current gain combined with lower base resistance
- wider temperature range of operation due to a larger bandgap combined with shallow impurity levels

Generally many of the advantages of the HBT come from the minority carrier blocking

ability of the wide gap heterojunction emitter. Unfortunately there are also disadvantages, some of which can be traced to the fabrication of the "abrupt" emitter base heterojunction [2]. These include, as will be examined in more detail in later sections , the difficulty of aligning the dopant junction with the alloy junction, combined with a tendency for out diffusion and epitaxial growth carry forward of dopant species from the heavily doped base. As analog applications are the most demanding in terms of uniformity and overall performance in general [1], some mechanism to either mitigate or circumvent these problems is required and will be discussed in more detail in a later section. In 1982 Kroemer [22] proposed the heterojunction bipolar transistor as a promising device for several application areas, including microwave and millimeter wave circuits, as well as digital, analog and combined optoelectronic applications. Fabrication of HBTs has attracted increased attention with the gradual improvement of compound semiconductor technology [23], combined with the potential strategic importance of the devices in the long term. One example of HBT experimental differential pair circuits indicated in figure 1.6 after [24] were fabricated with

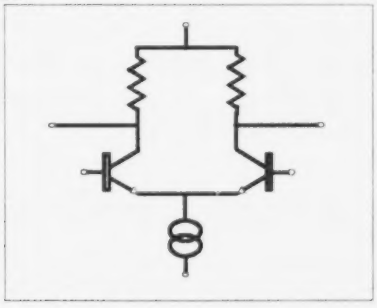

Figure 1.6: $Al_xGa_{1-x}As$ HBT differential test circuit for a test wafer
The average $\beta = 4.91$ with $\sigma_\beta = 0.21$ or 4.3%
and average $V_{offset} = 0.33$ mV with $\sigma_{offset} = 1.7$ mV.

disappointing results such as low current gain (β) combined with a high offset voltage, implying considerable improvement is necessary to produce competitive cost effective analog devices. As indicated in figure 1.7, the path of device evolution is fundamentally linked to a symbiotic relation between electrical simulation and the fabrication process. Various epitaxial growth techniques for GaAs/$Al_xGa_{1-x}As$ and other semiconductor systems are gradually improving, implying some could become major fabrication research and production tools for several heterostructure devices spanning a wide range of niche applications. Enhanced technology compound semiconductor properties combined with improved ingot growth, wafer quality and epitaxial growth processes may eventually enable profitable large scale mass market commercial growth and processing of Gallium Arsenide, Indium Phosphide and other substrates.

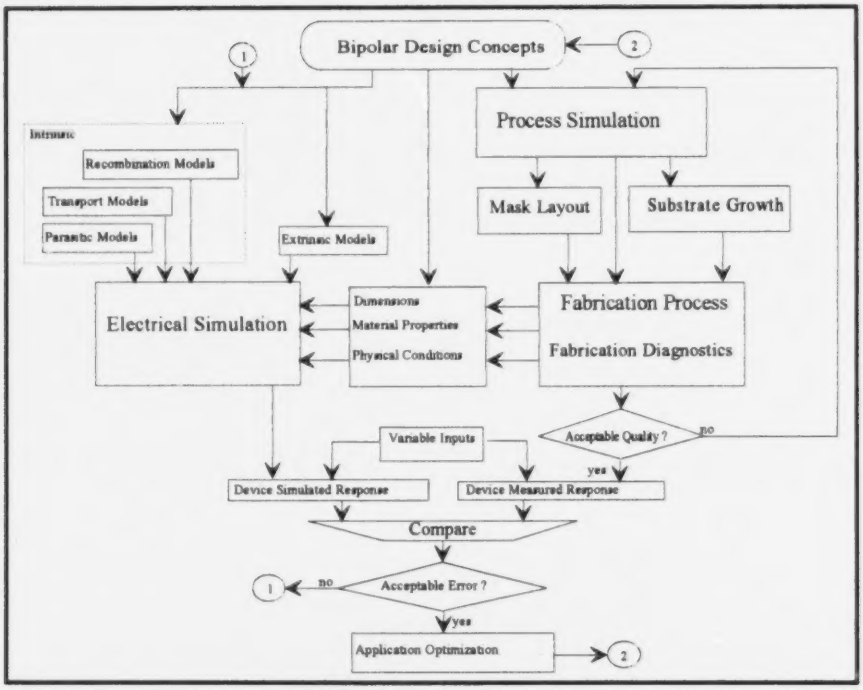

Figure 1.7: Overview of the production process

Improved ingot quality from growth systems conditions cannot be over emphasized as low circuit yield tends to reflect poor quality epi-layers and initial ingot problems [25]. Fabrication researchers with access to wafer processes have the opportunity to gradually improve quality and yield by, for example, experimenting with epitaxially deposited layers:

- using linear [19] (figure 1.8) or parabolic [26] aluminum mole fraction grading of the emitter base junction within the depletion region to minimize the conduction band spike.

- using linear grading of the aluminum content of the base [27] (figure 1.5) to create a built-in quasi-electric drift enhancement field.

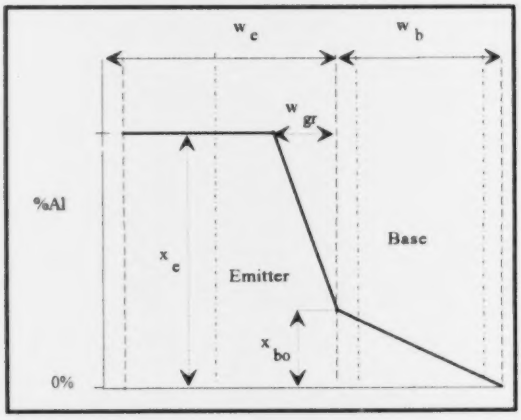

Figure 1.8: $Al_xGa_{1-x}As$ grade within emitter space charge region and base region

1.3 $Al_xGa_{1-x}As$ vs. Silicon Properties Overview

Before proceeding to more extensive device simulation a brief overview of bulk carrier

thermodynamic effects and approximations are undertaken, highlighting some phenomena indicating the general microscopic behavior of carriers under various conditions, which in turn determine the macroscopic electrical performance of a device. To optimize an electrical behavior under many possible operating conditions, the simulation should, as far as possible, include adequate carrier models which can, preferably, be parametrically driven by variables representing sufficiently localized conditions in the device. In general after [28] [29] and [30], the relative energy states of carriers in bulk semiconductors are sensitive to

- carrier scattering mechanisms or lack of them (i.e. nonequilibrium short range quasi-ballistic transport, traps)

- sub conduction and valence energy band infrastructure (i.e..shallow sub band edge energy states due to heavy doping)

- lattice temperature distribution (thermal energy production and transport through the device)

The three main $Al_xGa_{1-x}As$ conduction band energy minima are modeled [29] similarly to the indirect silicon X minimum and are given here with the parameterization used in following sections.

$$E_{X\_Si} = \left[1.170 - \frac{4.73 \cdot 10^{-4} \cdot K^{-1} \cdot T^2}{(T + 636 \cdot K)} \right] \cdot eV \qquad (1.17)$$

$$E_{\Gamma} = \left[(1.519 + 1.4 \cdot x) - \frac{5.405 \cdot 10^{-4} \cdot K^{-1} \cdot T^2}{(T + 204 \cdot K)} \right] \cdot eV \qquad (1.18)$$

$$E_L = \left[(1.815 + 1.09\,x) - \frac{6.05\,10^{-4}\,K^{-1}\,T^2}{(T + 204\,K)} \right] \cdot eV \qquad (1.19)$$

$$E_X = \left[(1.981 + 0.26\,x) - \frac{4.06\,10^{-4}\,K^{-1}\,T^2}{(T + 204\,K)} \right] \cdot eV \qquad (1.20)$$

The coefficients have been experimentally estimated [29] and the results plotted in figures 1.9 and 1.10, where it is apparent that a transfer of electrons is likely to occur to the X conduction band as alloy fraction(x) and temperature(T) increase.

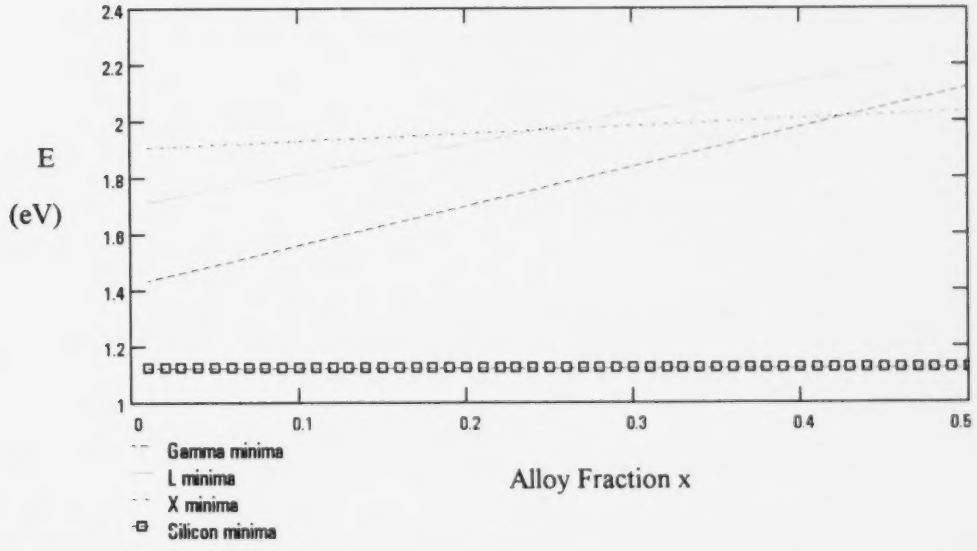

Figure 1.9: Plot of the main $Al_xGa_{1-x}As$ energy minima as a function of alloy fraction x at 300 K with Si for reference.

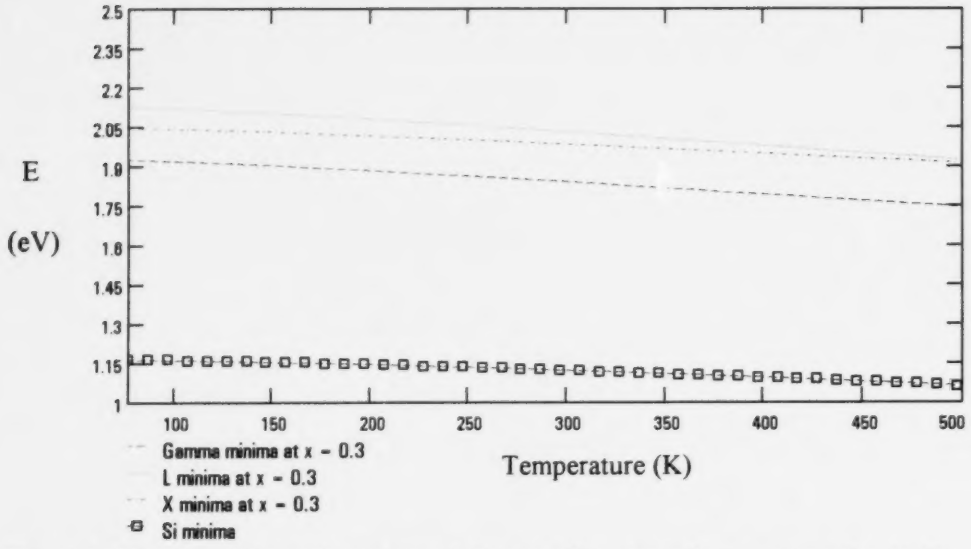

Figure 1.10: Plot of the main energy minima as a function of temperature for $Al_xGa_{1-x}As$ at x = 0.3 with Si for reference.

Clearly these properties of $Al_xGa_{1-x}As$ imply the designer should take adequate account of alloy concentration and temperature as a function of position and operating conditions within the device and between devices in the same analog circuit. Similarly $Al_xGa_{1-x}As$ minimum effective mass variation with alloy fraction is modeled after [29] as a linear interpolation.

$$m_\Gamma = m_0 \cdot (0.063 - 0.01 \cdot x) \tag{1.21}$$

$$m_L = m_0 \cdot (0.55 + 1.45 \cdot x) \tag{1.22}$$

$$m_X = m_o \cdot (0.85 + 0.14 \cdot x) \qquad (1.23)$$

compared to the density of states effective electron mass for silicon

$$m_{de\_Si} = \left(m_{le\_Si} \cdot m_{te\_Si}^{2}\right)^{\frac{1}{3}} \qquad (1.24)$$

which is plotted in figure 1.11, where minimal change of the Γ value is indicated with x and the ratio of the lower valley effective masses is approximately 5.2:1 in favour of Si.

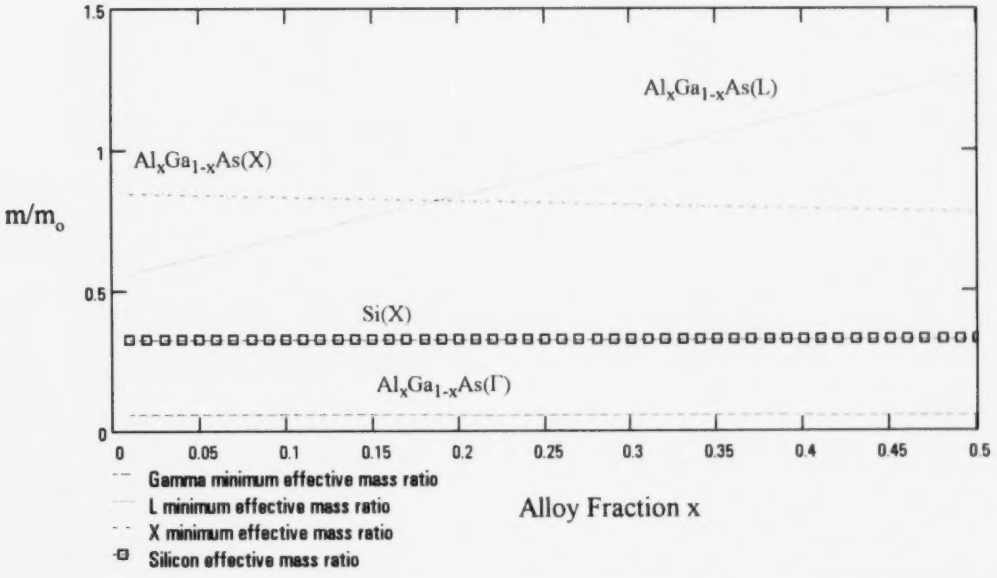

Figure 1.11: Plot of normalized minima effective mass as a function of x for $Al_xGa_{1-x}As$ with Si for reference.

Clearly one of the main advantages of compound semiconductor devices is the relatively low electron effective mass represented by a majority occupation of the Γ conduction band. The implication for device design is to minimize the probability of electrons scattering to the "upper valleys" in order to sustain the effective mass advantage. Each $Al_xGa_{1-x}As$ conduction band minimum has available electron energy states whose density variation is modeled [29] similarly to silicon as

$$N_{c\_Si}=2\cdot\left(2\cdot\pi\cdot m_{de\_Si}\cdot E_{th}(T)\cdot h^{-2}\right)^{\frac{3}{2}} \tag{1.25}$$

$$N_{\Gamma}=2\cdot\left(2\cdot\pi\cdot m_{\Gamma}(x)\cdot E_{th}(T)\cdot h^{-2}\right)^{\frac{3}{2}} \tag{1.26}$$

$$N_{L}=2\cdot\left(2\cdot\pi\cdot m_{L}(x)\cdot E_{th}(T)\cdot h^{-2}\right)^{\frac{3}{2}} \tag{1.27}$$

$$N_{X}=2\cdot\left(2\cdot\pi\cdot m_{X}(x)\cdot E_{th}(T)\cdot h^{-2}\right)^{\frac{3}{2}} \tag{1.28}$$

The relative occupation of the $Al_xGa_{1-x}As$ minima energy states by electrons in thermal equilibrium with the lattice can be modeled [29] using

$$n_{r\Gamma}=N_{\Gamma}(x,T)\cdot\exp\left(\frac{-E_{\Gamma}(x,T)}{E_{th}(T)}\right) \tag{1.29}$$

$$n_{rL} = N_L(x,T) \cdot \exp\left(\frac{E_L(x,T)}{E_{th}(T)}\right) \tag{1.30}$$

$$n_{rX} = N_X(x,T) \cdot \exp\left(\frac{E_X(x,T)}{E_{th}(T)}\right) \tag{1.31}$$

where the relative $Al_xGa_{1-x}As$ band overall population is the sum

$$n_{rT} = n_{r\Gamma}(x,T) + n_{rL}(x,T) + n_{rX}(x,T) \tag{1.32}$$

Comparing the $Al_xGa_{1-x}As$ band electron equilibrium occupation ratios, figure 1.12, implies normalized band occupation factors

$$\alpha_\Gamma = \frac{n_{r\Gamma}(x,T)}{n_{rT}(x,T)} \tag{1.33}$$

$$\alpha_L = \frac{n_{rL}(x,T)}{n_{rT}(x,T)} \tag{1.34}$$

$$\alpha_X = \frac{n_{rX}(x,T)}{n_{rT}(x,T)} \tag{1.35}$$

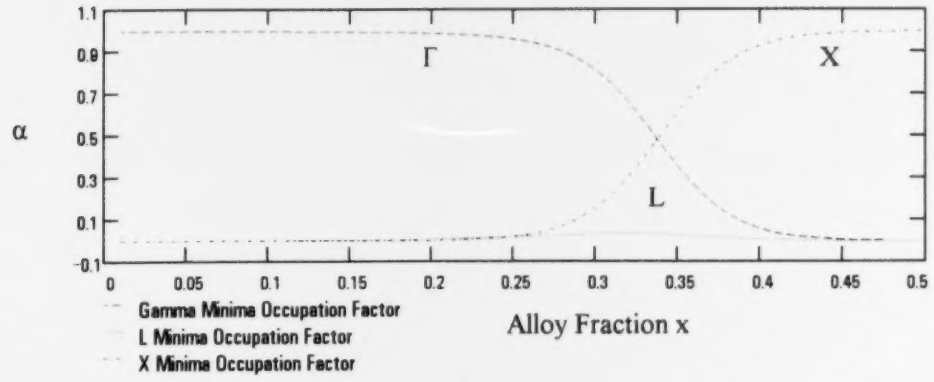

Figure 1.12: Normalized $Al_xGa_{1-x}As$ energy minima thermal equilibrium occupation factors as a function of x at 300 K.

Assuming that n-type donor atoms are all singly ionized at the temperatures of interest, the $Al_xGa_{1-x}As$ minima equilibrium electron density for a given ionized donor density would be expressed using the occupation factors, as

$$n_{o\Gamma} = N_D \alpha_\Gamma(x,T) \tag{1.36}$$

$$n_{oL} = N_D \alpha_L(x,T) \tag{1.37}$$

$$n_{oX} = N_D \alpha_X(x,T) \tag{1.38}$$

Again using the $Al_xGa_{1-x}As$ occupation factors the approximate average effective electron effective density of states mass can be expressed as

$$m_{de} = \alpha_{\Gamma}(x,T) \cdot m_{\Gamma}(x) + \alpha_{L}(x,T) \cdot m_{L}(x) + \alpha_{X}(x,T) \cdot m_{X}(x) \qquad (1.39)$$

where figure 1.13 indicates the effective mass and temperature penalty of increasing alloy fraction x.

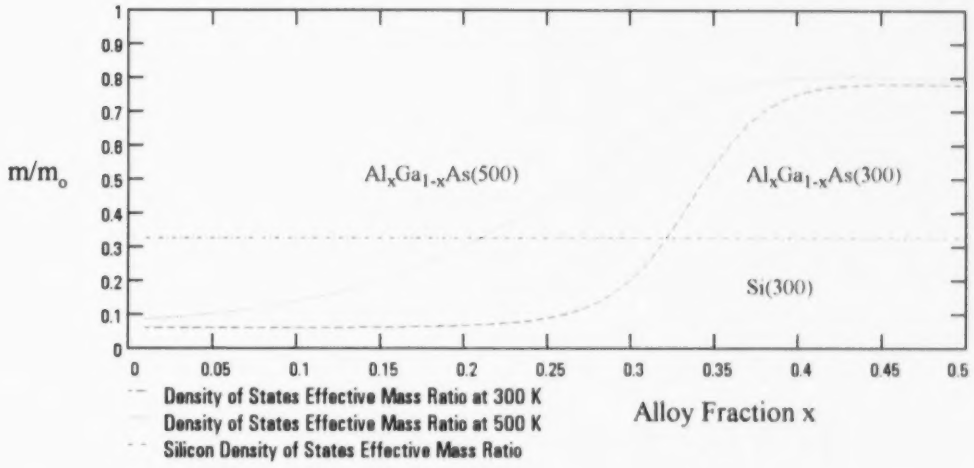

Figure 1.13: $Al_xGa_{1-x}As$ average density of states thermal equilibrium effective mass ratio as a function of x at 300 and 500 K with the 300 K Si value for reference

Light and heavy hole effective mass values are assumed for the range of x as a linear interpolation of the GaAs to AlAs extremes using after [29]

$$m_{lh} = m_{lh\_GaAs} + \left(m_{lh\_AlAs} - m_{lh\_GaAs}\right) \cdot x \qquad (1.40)$$

$$m_{hh} = m_{hh\_GaAs} + \left(m_{hh\_AlAs} - m_{hh\_GaAs}\right) \cdot x \tag{1.41}$$

The $Al_xGa_{1-x}As$ and Si effective density of states effective mass for holes are assumed after [31] to be modeled by

$$m_{dh} = \left(m_{lh}(x)^{\frac{3}{2}} + m_{hh}(x)^{\frac{3}{2}}\right)^{\frac{2}{3}} \tag{1.42}$$

and

$$m_{dh\_Si} = \left(m_{lh\_Si}^{\frac{3}{2}} + m_{hh\_Si}^{\frac{3}{2}}\right)^{\frac{2}{3}} \tag{1.43}$$

from which the effective density of states for the $Al_xGa_{1-x}As$ and Si valence bands are given by

$$N_v = 2 \cdot \left(\frac{2 \cdot \pi \cdot m_{dh}(x) \cdot E_{th}(T)}{h^2}\right)^{\frac{3}{2}} \tag{1.44}$$

$$N_{v\_Si} = 2 \cdot \left(\frac{2 \cdot \pi \cdot m_{dh\_Si} E_{th}(T)}{h^2}\right)^{\frac{3}{2}} \tag{1.45}$$

The intrinsic carrier concentrations can be approximated as

$$n_i = \sqrt{N_\Gamma(x,T)\cdot N_v(x,T)}\cdot e^{\frac{E_\Gamma(x,T)}{2\cdot E_{th}(T)}} + \sqrt{N_X(x,T)\cdot N_v(x,T)}\cdot e^{\frac{E_X(x,T)}{2\cdot E_{th}(T)}} + \sqrt{N_L(x,T)\cdot N_v(x,T)}\cdot e^{\frac{E_L(x,T)}{2\cdot E_{th}(T)}} \qquad (1.46)$$

and

$$n_{i\_Si} = \sqrt{N_{c\_Si}(T)\cdot N_{v\_Si}(T)}\cdot \exp\left(\frac{-E_{X\_Si}(T)}{2\cdot k\,T}\right) \qquad (1.47)$$

which when plotted against temperature give figure 1.14.

The $Al_xGa_{1-x}As$ low frequency (static) dielectric constant is linearly interpolated after [29] as

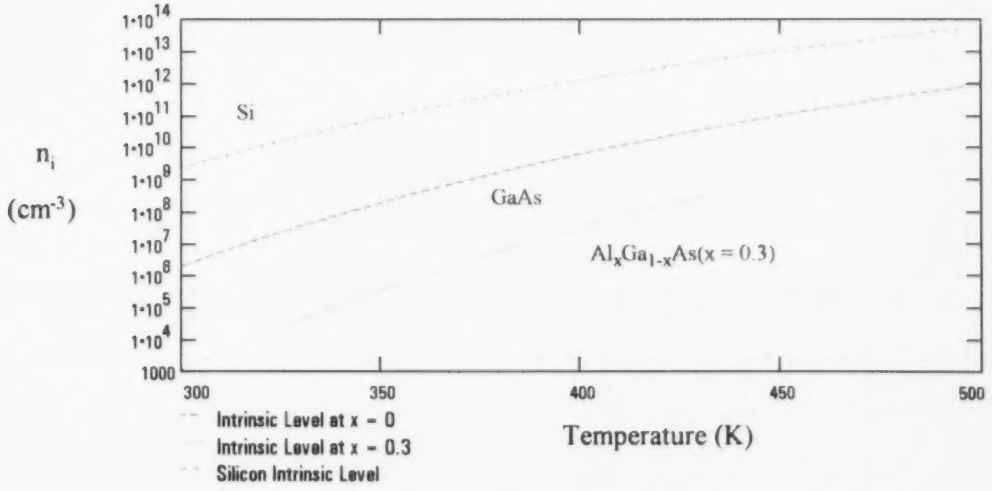

Figure 1.14: $Al_xGa_{1-x}As$ intrinsic carrier population as a function of lattice temperature at x = 0 and 0.3 with Si for reference.

$$\varepsilon_{s\_x} = \varepsilon_{GaAs} - (\varepsilon_{GaAs} - \varepsilon_{AlAs}) \cdot x \tag{1.48}$$

and the lattice thermal resistivity is quadratically approximated after [29] as

$$W_{s\_x} = W_{GaAs} + 28.83 \cdot cm \cdot K \cdot watt^{-1} \cdot x + 30 \cdot cm \cdot K \cdot watt^{-1} \cdot x^2 \tag{1.49}$$

where it should be noted that at x = 0.3 the thermal resistivity is about four times higher than pure GaAs due in part to alloy disorder effects.

1.4 Analysis of a Bandgap Graded $Al_xGa_{1-x}As$ Base

As indicated in the overall process diagram, figure 1.7, electrical simulation requires realistic models of intrinsic and extrinsic behavior [30]. One of the main goals of both models is to supply optimization information for the fabrication process. To supply this information it is desirable for the dimensions, material parameters and physical conditions of the devices to be variables in the electrical simulation such that the effect of process changes can be seen on electrical performance. One dimensional drift diffusion equation (DDE) models are typically able to accomplish this [30] by assuming a hydrodynamic representation of the particles in a representative vertical line, which

passes through the intrinsic region in the main direction of majority carrier current flow. The electric field acting on an electron within the base quasi-neutral region is approximated [27] by assuming that only the fractional conduction band offset is involved for the gamma band over the assumed linear alloy graded base region, ignoring for the present base dopant concentration grading.

$$F_{zb} = \left[\frac{\alpha_c}{q} \frac{\left(E_\Gamma(x_{bo}, T) - E_\Gamma(x_{bw}, T) \right)}{w_b} \right] \tag{1.50}$$

Here x_{bo} and x_{bw} are the alloy mole fractions assumed to exist at the top and bottom of the base layer and α_c is the ratio of conduction band offset to total offset. Clearly as x_{bo} increases in figure 1.15 the built-in field increases and the electric field threshold for scattering to the L minimum is reduced somewhat using

$$\kappa_{\Gamma L} = \frac{F_m}{E_L(x=0, T_r) - E_\Gamma(x=0, T_r)} \tag{1.51}$$

where

$$F_{\Gamma L} = \kappa_{\Gamma L} \left(E_L(x, T) - E_\Gamma(x, T) \right) \tag{1.52}$$

and it is assumed transient electron velocity overshoot is negligible up to about 4 kV/cm.

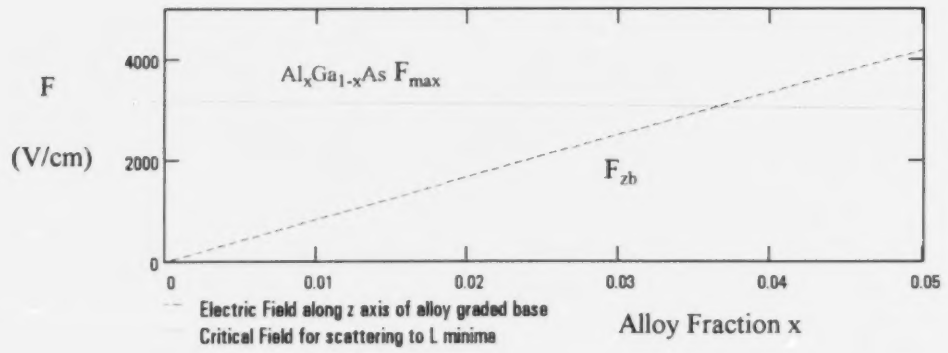

Figure 1.15: $Al_xGa_{1-x}As$ graded base built in electric field for a 100 nm wide base at T = 300 K as a function of alloy fraction at the emitter side assuming x = 0 at the collector side

Using the DDE, equation 1.53, for the base layer it is assumed that a quasi-static equilibrium exists such that while the carriers may be moving rapidly through the base layer their concentration as a function of z, $n_b(z)$, is not varying in time.

$$D_{nb}\cdot\frac{d^2}{dz^2}n_b(z)+\mu_{nb}\cdot F_{zb}\cdot\frac{d}{dz}n_b(z)-\frac{n_b(z)-n_{bo}}{\tau_{nb}}=0=\frac{d}{dt}n_b(z) \qquad (1.53)$$

It is assumed that excess minority carriers injected from the emitter appear at z = 0 at level $n_b(0)$. The carriers that appear at z = 0 are transported by diffusion corresponding to the first term and drifting, corresponding to the second term, in the F_{zb} field to $z = w_{bqn}$, the width of the base quasi neutral region. The third term corresponds to the excess

carriers at a given location divided by the lifetime associated with that location. As the lifetime is not significantly affected by lower alloy fractions an average value is assumed for the base layer as a whole. It is assumed that carriers are efficiently extracted at $z = w_{bqn}$ such that the concentration of minority carriers at the edge of the base collector space charge region is in the order of $n_b(w_{bqn}) = n_{bo}$ the base equilibrium level. In summary the initial core theoretical assumptions are that the injected electrons do not appreciably disturb their environment. They essentially execute a random walk across the base with drift velocity being accumulated between collisions in such a fashion that the electrons do not appreciably scatter to the L minimum. As the advantages of the wide gap emitter are exploited by very high base acceptor levels it is assumed that the dominant source of scattering at the temperatures of interest is ionized acceptor scattering and that all of the acceptors resident in the base are in fact ionized. An estimate of the average electron mobility in the base is made using the Brooks-Herring [32] ion scattering approach combined with a low doped sample estimate limit to correlate variability with base dopant, temperature and alloy content with equivalent assumptions for silicon giving

$$\mu_I = \frac{64\cdot\sqrt{\pi}\,\varepsilon_s^{2}\cdot(2\cdot k\cdot T)^{\frac{3}{2}}}{N_I\, q^3\cdot m_e^{\frac{1}{2}}}\cdot\ln\left[1+\left[\frac{12\cdot\pi\cdot\varepsilon_s\cdot k\,T}{q^2\cdot N_I^{\frac{1}{3}}}\right]^2\right]^1 \qquad (1.54)$$

where using the empirical temperature adjustment for the limit

$$\mu_{no\_ld} = \mu_{no} \cdot \left(\frac{T_r}{T}\right)^{2.3} \tag{1.55}$$

then the estimate as a function of x is

$$\mu_{n\_x} = \left(\frac{1}{\mu_{no\_ld}(\mu_{no\_GaAs}, T)} + \frac{1}{\mu_i(N_I, m_{de}(x,T), \varepsilon_{s\_x}(x), T)}\right)^{-1} \tag{1.56}$$

and for Si

$$\mu_{n\_Si} = \left(\frac{1}{\mu_{no\_ld}(\mu_{no\_Si}, T)} + \frac{1}{\mu_i(N_I, m_{de\_Si}, \varepsilon_{Si}, T)}\right)^{-1} \tag{1.57}$$

The resultant comparative electron mobilities used for later simulations are plotted as a function of dopant concentration, alloy fraction and temperature in figures 1.16 through 1.18.

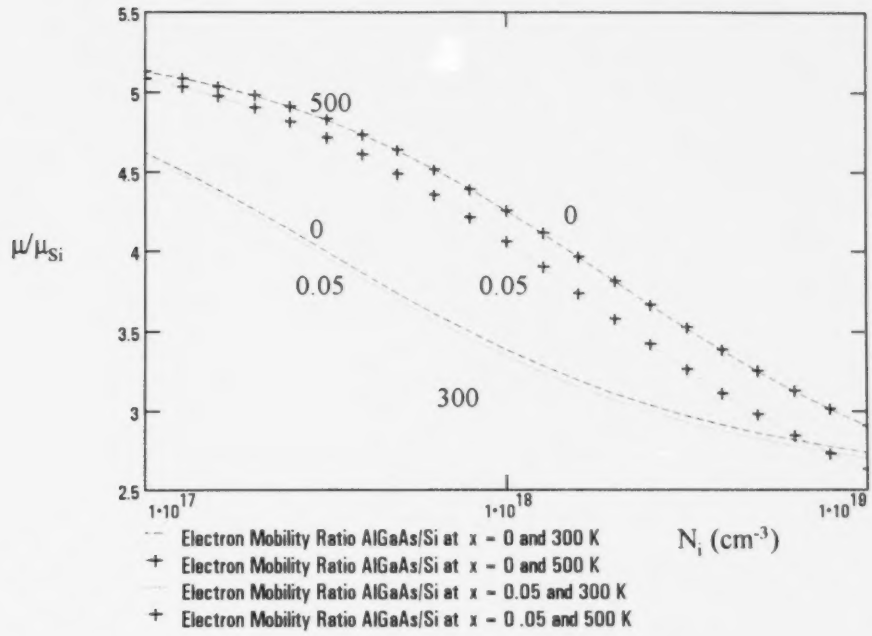

Figure 1.16: $Al_xGa_{1-x}As$ vs. Si low electric field electron mobility estimates for x = 0 and 0.05 at T = 300 and 500 K as a function of acceptor ion concentration

Along with the mobility an estimate of minority carrier life times is needed for a parametrized solution of the DDE. The average thermal velocity combined with the number of traps and the trap cross section gives an approximate lifetime as

$$\tau_n = \frac{1}{\sigma_n \cdot \nu_{th}(m_e, T) \cdot N_t} \tag{1.58}$$

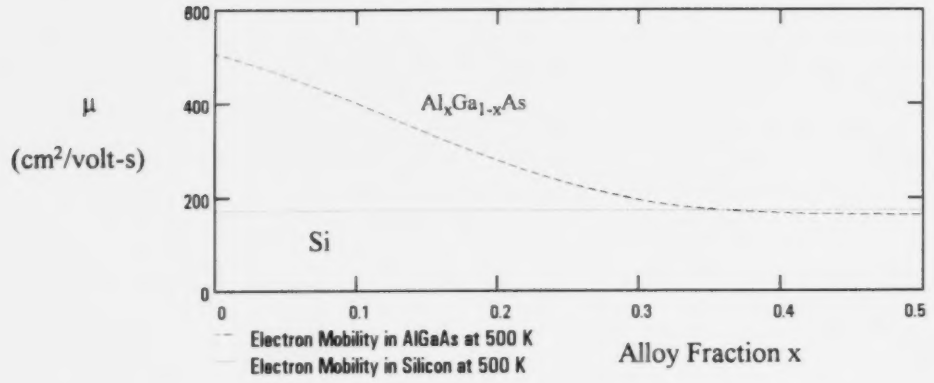

Figure 1.17: $Al_xGa_{1-x}As$ and Si electron mobility estimate for $N_I = 10^{19}$ cm^{-3} and T = 500 K as a function of x.

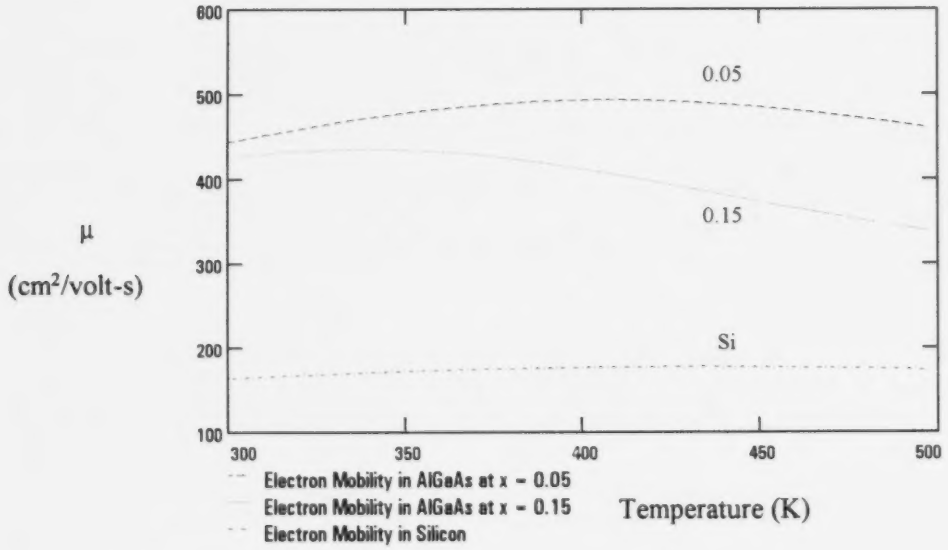

Figure 1.18: $Al_xGa_{1-x}As$ and Si low field electron mobility estimate for x = 0.05 and 0.15 with $N_I = 10^{19}$ cm^{-3} as a function of temperature.

Assuming the same capture cross section for $Al_xGa_{1-x}As$ as for pure GaAs such that the average lifetime of an electron in the base is approximated by

$$\tau_{n\_x} = \tau_n\left(N_t, \sigma_{n\_GaAs}, m_{de}(x,T), T\right) \tag{1.59}$$

and for an Si base as

$$\tau_{n\_Si} = \tau_n\left(N_t, \sigma_{n\_Si}, m_{de\_Si}, T\right) \tag{1.60}$$

which assuming acceptor ions are equivalent to traps gives the representative electron lifetimes of figure 1.19.

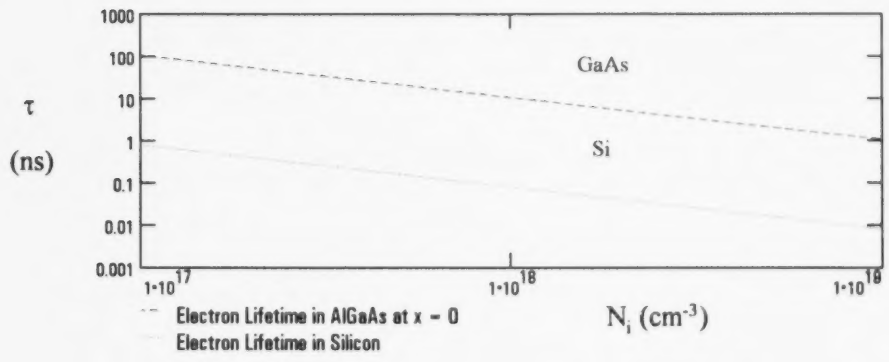

Figure 1.19: $Al_xGa_{1-x}As$ and Si electron lifetime estimate for x = 0 and T = 300 K as a function of base acceptor ion concentration assumed as equivalent to traps

Two further parameters are required for the solution, the electron diffusion constant in the base which can now be formulated using the thermal voltage

$$D_{n\_x} = \mu_{n\_x}(N_t, x, T) \cdot V_{th}(T) \tag{1.61}$$

and for Si

$$D_{n\_Si} = \mu_{n\_Si}(N_t, T) \cdot V_{th}(T) \tag{1.62}$$

and the diffusion length of electrons in the base which can now be formulated as

$$L_{n\_x} = \sqrt{D_{n\_x}(N_t, x, T) \cdot \tau_{n\_x}(N_t, x, T)} \tag{1.63}$$

and

$$L_{n\_Si} = \sqrt{D_{n\_Si}(N_t, T) \cdot \tau_{n\_Si}(N_t, T)} \tag{1.64}$$

Restructuring the alloy graded base DDE as

$$\frac{d^2}{dz^2} n_b(z) + \alpha \cdot \frac{d}{dz} n_b(z) - \frac{n_b(z) - n_{bo}}{L_{nb}^2} = 0 \tag{1.65}$$

where

$$\alpha_{AlGaAs} = \frac{F_{zb}(w_b, x_{bo}, x_{bw}, T)}{V_{th}(T)} \tag{1.66}$$

and

$$\alpha_{Si} = 0 \cdot cm^{-1} \tag{1.67}$$

where using the simplifying assignment

$$\gamma := \frac{\alpha_{AlGaAs}(w_b, x_{bo}, x_{bw}, T)}{2} \tag{1.68}$$

and assuming an average base alloy

$$x_{b\_av} := \frac{x_{bo} + x_{bw}}{2} \tag{1.69}$$

results in

$$\phi_{AlGaAs} := \frac{1}{2}\cdot\left(\alpha_{AlGaAs}(w_b, x_{bo}, x_{bw}, T)^2 + \frac{4}{L_{n\_x}(N_b, x_{b\_av}(x_{bo}, x_{bw}), T)^2}\right)^{\frac{1}{2}} \tag{1.70}$$

and

$$\phi_{Si} := \frac{1}{L_{n\_Si}(N_b, T)} \tag{1.71}$$

giving the roots

$$r_{b1\_x} := \gamma(w_b, x_{bo}, x_{bw}, T) + \phi_{AlGaAs}(N_b, w_b, x_{bo}, x_{bw}, T) \tag{1.72}$$

and

$$r_{b1\_Si} := \phi_{Si}(N_b, T) \tag{1.73}$$

and

$$r_{b2\_x} := \gamma(w_b, x_{bo}, x_{bw}, T) - \phi_{AlGaAs}(N_b, w_b, x_{bo}, x_{bw}, T) \tag{1.74}$$

and

$$r_{b2\_Si} := r_{b1\_Si}(N_{Ab}, T) \tag{1.75}$$

Similarly using the assignments

$$\zeta_{AlGaAs} := 2 \cdot e^{\gamma(w_b, x_{bo}, x_{bw}, T) \cdot w_{bqn}} \cdot \sinh\left(\phi_{AlGaAs}\left(N_b, w_b, x_{bo}, x_{bw}, T\right) \cdot w_{bqn}\right) \tag{1.76}$$

and

$$\zeta_{Si} := 2 \cdot \sinh\left(\phi_{Si}\left(N_b, T\right) \cdot w_{bqn}\right) \tag{1.77}$$

the constants become

$$c_{b1\_x} := \frac{n_{xs}}{\zeta_{AlGaAs}\left(w_{bqn}, N_b, w_b, x_{bo}, x_{bw}, T\right)} \tag{1.78}$$

and

$$c_{b1\_Si} := \frac{n_{xs}}{\zeta_{Si}\left(w_{bqn}, N_b, w_b, T\right)} \tag{1.79}$$

and

$$c_{b2\_x} := c_{b1\_x}\left(n_{xs}, w_{bqn}, N_b, w_b, x_{bo}, x_{bw}, T\right) \tag{1.80}$$

and

$$c_{b2\_Si} := c_{b1\_Si}\left(n_{xs}, w_{bqn}, N_b, w_b, T\right) \tag{1.81}$$

where n_{xs} is the injected electron concentration from the emitter barrier. Assuming the equilibrium electron level in the base is approximated by

$$n_{bo\_x} := \frac{n_i\left(x_{b\_av}\left(x_{bo}, x_{bw}\right), T\right)^2}{N_b} \tag{1.82}$$

and with

$$n_{bo\_Si} = \frac{n_{i\_Si}(T)^2}{N_b} \tag{1.83}$$

the distributions become

$$\begin{aligned} n_{b\_x} = {} & c_{b1\_x}\left(n_{xs}, w_{bqn}, N_b, w_b, x_{bo}, x_{bw}, T\right) \cdot e^{r_{b1\_x}\left(N_b, w_b, x_{bo}, x_{bw}, T\right) \cdot z} \ldots \\ & + c_{b2\_x}\left(n_{xs}, w_{bqn}, N_b, w_b, x_{bo}, x_{bw}, T\right) \cdot e^{r_{b2\_x}\left(N_b, w_b, x_{bo}, x_{bw}, T\right) \cdot z} \ldots \\ & + \left(n_{xs} + n_{bo\_x}\left(N_b, x_{bo}, x_{bw}, T\right)\right) \end{aligned} \tag{1.84}$$

and

$$\begin{aligned} n_{b\_Si} = {} & c_{b1\_Si}\left(n_{xs}, w_{bqn}, N_b, w_b, T\right) \cdot e^{r_{b1\_Si}\left(N_b, T\right) \cdot z} \ldots \\ & + c_{b2\_Si}\left(n_{xs}, w_{bqn}, N_b, w_b, T\right) \cdot e^{r_{b2\_Si}\left(N_b, T\right) \cdot z} + n_{xs} + n_{bo\_Si}\left(N_b, T\right) \end{aligned} \tag{1.85}$$

the base carrier distribution with no alloy content becomes

$$n_{b\_t\_x} = n_{b\_x}\left(z, n_{xs\_t}, w_{bqn\_t}, N_{Ab\_t}, w_{b\_t}, x_{bo}, x_{bw} = 0, T_r\right) \tag{1.86}$$

and

$$n_{b\_t\_Si} = n_{b\_Si}\left(z, n_{xs\_t}, w_{bqn\_t}, N_{Ab\_t}, w_{b\_t}, T_r\right) \tag{1.87}$$

which gives the base minority carrier profiles indicated in figure 1.20 where the zero alloy GaAs base and the Si base have the same distributions. Using the parametric data of figure 1.20 for figure 1.21 the total electron content of the base decreases with increased built in field as indicated in figure 1.21. Differentiating with respect to z and using the drift diffusion terms of current density gives

$$J_{nb\_x\_drift} = q\,\mu_{n\_x}\left(N_{b},x_{bo},T\right)\cdot n_{b\_x}\left(z,n_{xs\_t},w_{bqn\_t},N_{b},w_{b\_t},x_{bo},x_{bw}=0,T\right)\cdot F_{zb}\left(w_{b\_t},x_{bo},x_{bw}=0,T\right)$$

(1.88)

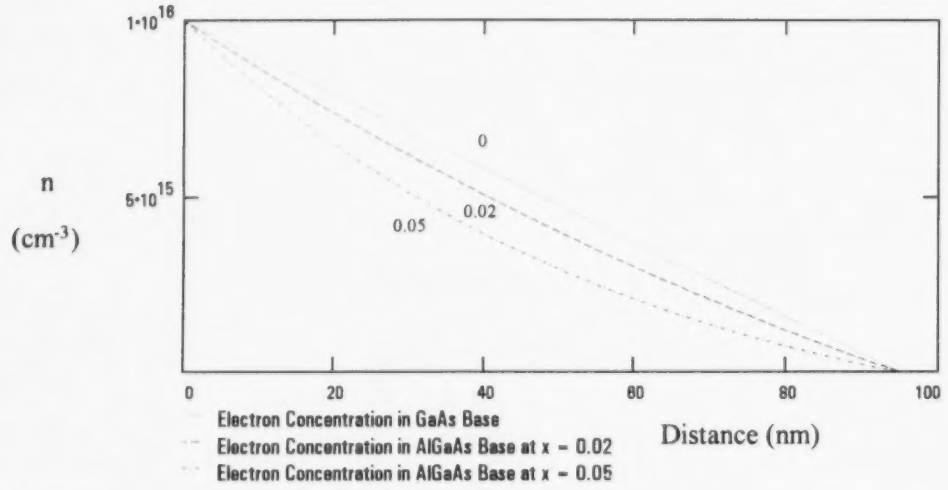

Figure 1.20: The electron concentration for a 100 nm wide p-type base as a function of distance from the emitter base scr edge with x_{bo} = 0, 0.15 and 0.3 using $N_b = 10^{18}$ cm^{-3}

The drop in base minority carrier content with x of figure 1.20 is plotted in figure 1.21.

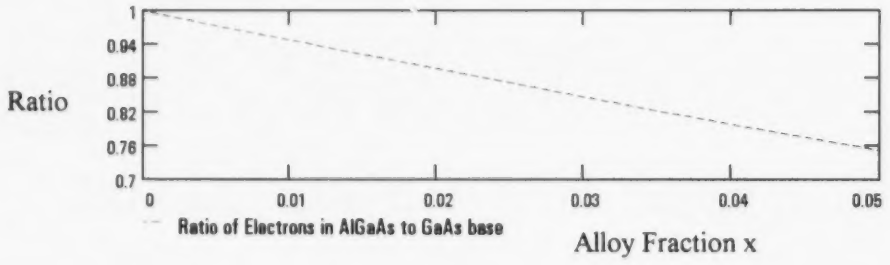

Figure 1.21: The ratio of electron content for a 100 nm wide p-type $Al_xGa_{1-x}As$ base with increasing alloy grade x with respect to the value at x = 0

The diffusion current densities in the base are

$$J_{nb\_x\_dif}(z) = q\, D_{n\_x}\, \frac{d}{dz} n_{b\_x}(z, n_{xs\_t}, w_{bqn\_t}, N_{b}, w_{b\_t}, x_{bo}, x_{bw} = 0, T) \qquad (1.89)$$

and

$$J_{nb\_Si\_dif}(z) = q\, D_{n\_Si}\, \frac{d}{dz} n_{b\_Si}(z, n_{xs\_t}, w_{bqn\_t}, N_{b}, w_{b\_t}, T) \qquad (1.90)$$

which when plotted in figure 1.22 indicate an increase of current density with alloy content.

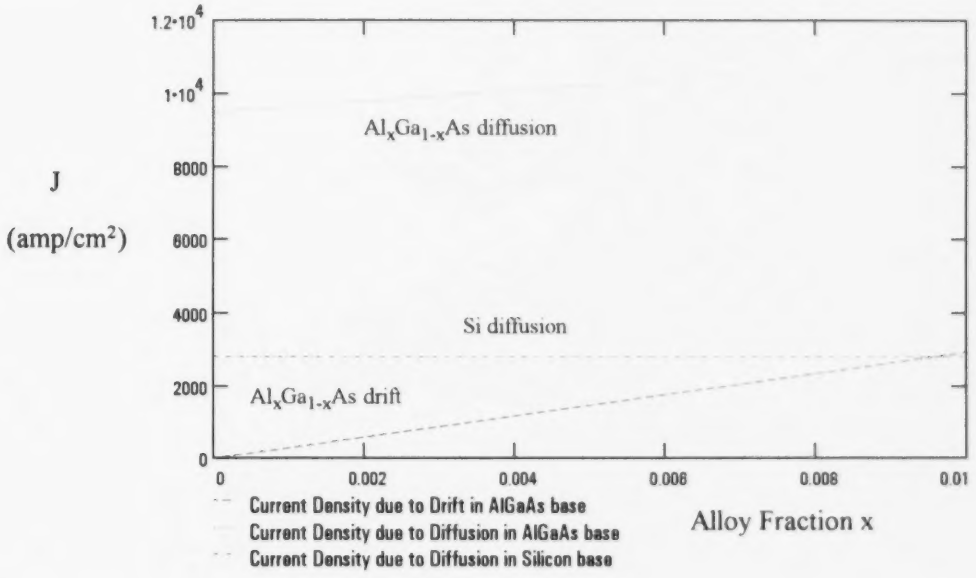

Figure 1.22: Current density components for a 100 nm wide p-type $Al_xGa_{1-x}As$ base as a function of increasing alloy content with Si for reference. Parameters are the same as for figures 1.20 and 1.21.

In summary, alloy grading of the base appears to have some clearly beneficial effects, increasing the current density capacity at a given emitter determined injection level and

reducing the minority carrier charge stored in the base at a given collector current which reduces the base transit time.

1.5 $Al_xGa_{1-x}As$ Junction Types and Diffusion Potentials

Before considering the overall transistor models of the following sections the interface or junction between semiconductor layers must be characterized. The ability to vary dopant and alloy content during growth implies the existence of four general classes of junction or transition zone between semiconductor regions. If there is a change of dopant concentration from n to p type semiconductor or vice versa it is called a heterotype junction class and if not an isotype junction class. If there is a change of semiconductor base material such as a change of alloy content it is referred to as a heterojunction class and if not a homojunction class. The four combinations are isotype homojunction, heterotype homojunction(α), isotype heterojunction(β) and heterotype heterojunction(γ). For heterotype homojunctions the built in voltage or diffusion potential at thermal equilibrium can be approximated as

$$V_{\alpha\_x} = V_{th}(T) \cdot \ln\left[\frac{N_1 \cdot N_2}{n_i(x,T)^2}\right] \tag{1.91}$$

and

$$V_{\alpha\_Si} = V_{th}(T) \cdot \ln\left[\frac{N_1 \cdot N_2}{n_{i\_Si}(T)^2}\right] \tag{1.92}$$

where the alloy fraction x is the same on both sides of the junction such that the space charge region (scr) is due solely to the distribution of acceptor/donor (N_1) and donor/acceptor (N_2) ions. Following the same line of development the $Al_xGa_{1-x}As$ heterotype heterojunction built in voltage or diffusion potential is estimated, by using alloy induced differential intrinsic levels in equation 1.91, as

$$V_{\gamma} = V_{th}(T) \cdot \ln\left(\frac{N_1 \cdot N_2}{n_i(x_1, T) \cdot n_i(x_2, T)}\right) \qquad (1.93)$$

Similarly the $Al_xGa_{1-x}As$ isotype heterojunction built in voltage or diffusion potential for the case of p-p or n-n is estimated by summing the separate contributions of the dopant and alloy induced differential intrinsic levels as

$$V_{\beta} = V_{th}(T) \cdot \left(\ln\left(\frac{N_1}{N_2}\right) + \ln\left(\frac{n_i(x_2, T)}{n_i(x_1, T)}\right)\right) \qquad (1.94)$$

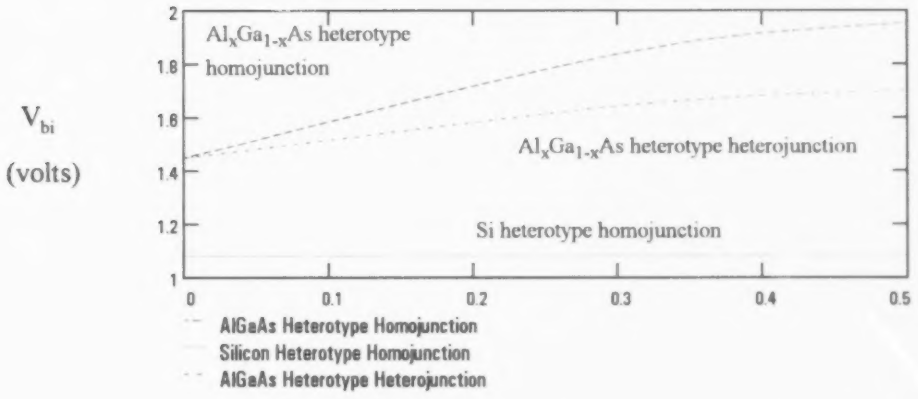

Figure 1.23: Diffusion potential of the $Al_xGa_{1-x}As$ and Si heterotype junctions as a function of increasing alloy fraction x with an acceptor level of 10^{19} and donor level of 10^{18} cm^{-3} at 300 K

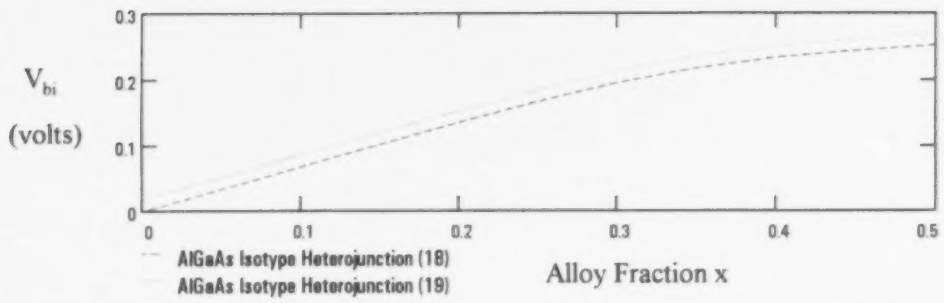

Figure 1.24: Diffusion potential of the $Al_xGa_{1-x}As$ isotype heterojunction with a narrow gap alloy fraction of zero and a wide gap ion level of 10^{18} and 10^{19} cm^{-3}, as a function of increasing wide gap alloy fraction x at 300 K

which when plotted in figure 1.23 and 1.24, indicates increasing diffusion potential with alloy fraction. It should be noted that the higher diffusion potential of the $Al_xGa_{1-x}As$ heterotype homojunction compared to the heterotype heterojunction is due to the presence of alloy on only one side of the latter.

1.6 Section Summary

A brief overview of some of the more relevant factors affecting the position of the work in following sections with respect to the field of compound semiconductor bipolar devices and competing technologies has been undertaken. A basic analysis of the cutoff frequency of competing technologies indicated that a unique position may be available for $Al_xGa_{1-x}As$ and related bipolar devices, especially in consideration that their closest rivals are FET devices with somewhat less suitable characteristics for broadband analog

application that require tighter lithographic control for devices with similar frequency capability. The potential applications including optoelectronic systems were briefly considered followed by a review of basic definitions and fabrication steps for the emitter up and collector up orientations with some discussion as to their relative merit. The intrinsic region was defined and the energy band diagram of a line through the intrinsic region introduced for an npn HBT device. This was followed by a summary in point form of the potential benefits of the wide gap emitter HBT compared to a silicon BJT. Some of the technical problems involved in HBT fabrication were discussed with an example of some fabrication results involving matching differential pairs, one of the basic building blocks of analog circuits, which highlights the problems of potentially low current gain combined with high offset voltage variability across the wafer. The overall plan of design and production was discussed starting from the production of high quality wafers through to an acceptable product for niche applications. The role of production enabled design innovations were covered in the form of epitaxial techniques, which are the basis of bandgap engineering with an example of a graded emitter HBT followed by an overview of some $Al_xGa_{1-x}As$ semiconductor property variations with aluminum alloy fraction with silicon as a comparative reference. An example of bandgap engineering was analyzed in the form of an alloy graded base, which is used in later sections, indicating how assumptions and approximations as to material properties and carrier behavior are used in simulation equations. Finally the four classes of semiconductor to semiconductor $Al_xGa_{1-x}As$ junction which could be utilized in bipolar devices were defined with their approximate diffusion potentials using equations from the property variations section.

Chapter 2

REVIEW AND MODEL DEVELOPMENT

This section reviews research on aspects of compound semiconductor bipolar device design and simulation with relevance to the following work in the next section starting with an overview of surface, junction space charge region and bulk recombination and leading to an identification of the role of current density component ideality in shaping the device overall current gain characteristic. Effective dopant bandgap narrowing approximations are covered for various atomic species for incorporation into the modeling of carrier emission over or through controlled or self adjusting variable height energy barriers, fundamental to bipolar device operation. A parametrized model of equivalently doped slices of npn and pnp silicon and $Al_xGa_{1-x}As$ bipolar devices is postulated with a comparative approximate emitter base voltage based on the thermionic emission necessary for a given current density. Emitter base junction space charge region widths and capacitances are then estimated based on the emitter base applied voltage for a given current density. Resistance components for the model are estimated by defining device segments and deriving the sheet mobility by assuming carrier stationary ion scattering is the dominant limitation. The model is then used to compare the four devices' relative lateral base resistance components, emitter charging time, base transit time and collector transit time. Finally the components are selectively assembled to compare the cutoff frequency and maximum frequency of oscillation which are formulated and compared for a fixed set of equivalent parameters at a relatively high current density.

2.1 **Recombination Currents**

The assumption of approximately constant β vs. I_c often made for Si based homojunction devices does not generally apply to compound semiconductor bipolar devices [33]. Surface energy states associated with high variable surface recombination velocity makes the low I_c dc base current of a GaAs based bipolar device differ significantly from that of a SiO_2 passivated silicon based bipolar device [34]. At a GaAs semiconductor-air interface, oxide formation and changing lattice conditions due to several mechanisms promote band distortion and the formation of intragap energy states as the surface is approached from the bulk [35]. A thin layer of surface charge may exist or be induced by varying conditions in the bulk changing the width of the surface depletion region. Similarly to the fat FET of the MESFET test patterns described in [36] large area HBT test devices of reducing circumference [35] illustrate the relative effect of periphery surface recombination current. Some progress has been made by using self aligned base [37] contacts and post fabrication surface treatments [38] to reduce the current loss. An increased band gap or emitter ledge at the base surface [39] also appears to decrease base gap recombination current. As indicated in figure 2.1 surface and bulk recombination currents are supplied by the emitter and base contacts such that dc base current is essentially providing carriers minus any hole contribution from the base collector scr for the level of recombination at a given collector current, while emitter current supplies equivalent recombination plus collector current minus any generation current contributed by ionization in the base collector scr.

The major HBT surface recombination currents include

· emitter sidewall surface recombination: $I_{re\_sidewall}$

· base contact to emitter gap surface recombination: I_{reb_gap}

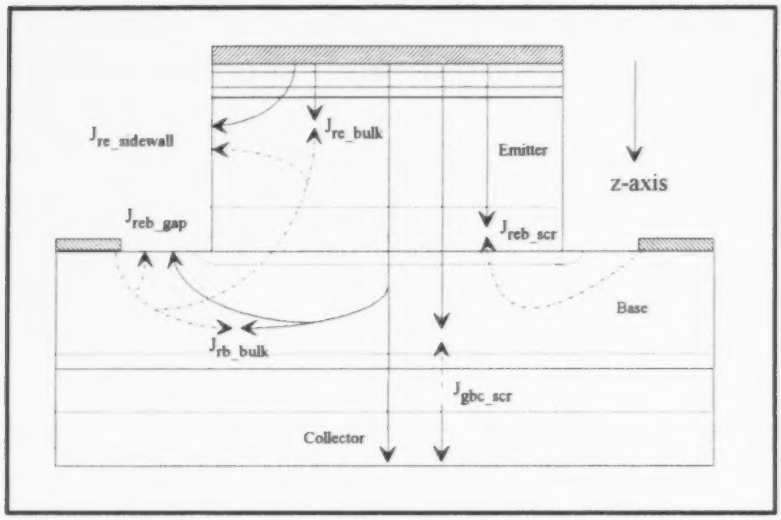

Figure 2.1: Schematic view of HBT major recombination currents

while the major bulk recombination and generation currents include

· emitter base space charge region recombination: I_{reb_scr}

· base bulk recombination: I_{rb_bulk}

· emitter bulk recombination: I_{re_bulk}

· collector space charge region avalanche generation: I_{gbc_scr}

If I_U and I_G are the current contributions due to recombination and generation and $\beta = I_c / I_b$ for a bipolar device where $I_c = I_e - I_U + I_G$ and $I_b = I_U - I_G$ the preferred analog situation of constant β of approximately 50 to 100 for useable I_c becomes the problem of optimizing the conglomerate I_U and I_G as a function of I_c. The general conglomerate recombination current equation for a forward biased EB junction is given by

$$I_{u\_gcr} = I_o \cdot \exp\left(\frac{V_{eb}}{\eta_{gcr} \cdot V_{th}(T)}\right) \qquad (2.1)$$

where both the ideality factor in the range of 1.4 to 2 and I_o of are overall representations of the entire device including localized band bending defects in the EB scr. This current can also be expressed as the sum of two parts [40]

$$I_{U\_2} = I_1 \cdot \exp\left(\frac{V_{eb}}{\eta_1 \cdot V_{th}(T)}\right) + I_2 \cdot \exp\left(\frac{V_{eb}}{\eta_2 \cdot V_{th}(T)}\right) \qquad (2.2)$$

where $\eta_1 \sim 1$ and $\eta_2 \sim 2$ leading to the reference "kT current" and "2kT current" respectively. The kT component is well understood and derives from several sources including diffusion of carriers across the junction scr [35]. The 2kT component similarly has several sources and in general results from either the proportionality of equality of

the carrier levels undergoing recombination [35]. During an investigation of large dark spots (LDS) which are broad nonluminescent regions near device surfaces and damage sites Henry, Logan and Merritt (HLM) [35] discovered the LDS were regions of intense nonradiative recombination. If a constant surface recombination velocity is assumed only a kT component results. HLM proposed a theory based on the surface charge being equal and opposite to the subsurface depletion layer charge which ensures that the recombination current will have a 2kT character over a wide range of adjacent bulk conditions and leads to the conclusion that the surface recombination velocity is proportional to the inverse square root of the minority carrier density in the adjacent bulk. Further HLM demonstrated the diffusion/channeling of of minority carriers injected from a junction intersecting the surface down a confined surface depletion width(w_{sd}) until they recombine. The maximum width of the surface depletion region is determined by the number of surface states(N_s) available with respect to the ion density in the depletion region.

$$w_{sd\_max} = \frac{N_s}{N_I} \tag{2.3}$$

where taking a representative trap density after [35]

$$N_{s\_x} = 8.4 \cdot 10^{12} \cdot cm^{-2} \tag{2.4}$$

the worst case depletion width and 20% occupancy is plotted vs. doping level in figure 2.2.

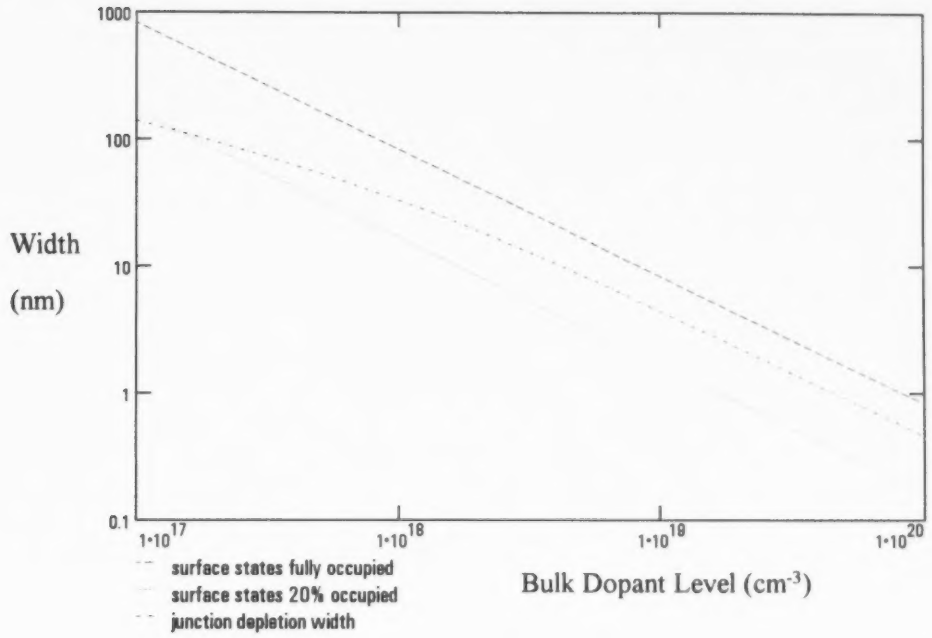

Figure 2.2: Approximate $Al_xGa_{1-x}As$ surface and junction depletion width as a function of dopant ion concentration with worst case and 20% occupancy surface charge

From figure 2.2 it is apparent that at the relatively high dopant concentrations used in both the emitter and base of HBT devices will tend to minimize the surface depletion widths. A typical device may have an emitter level of 5×10^{18} and base level of 5×10^{19} ions per cubic centimeter resulting in low bias surface depletion widths of about 50 nm in the emitter and 5 nm in the base, as illustrated in figure 2.3. As lateral emitter widths become increasingly narrow the internal central channel between surface depletion regions approaches pinch off likely limiting the practical minimum width of the emitter to significantly greater than 100 nm.

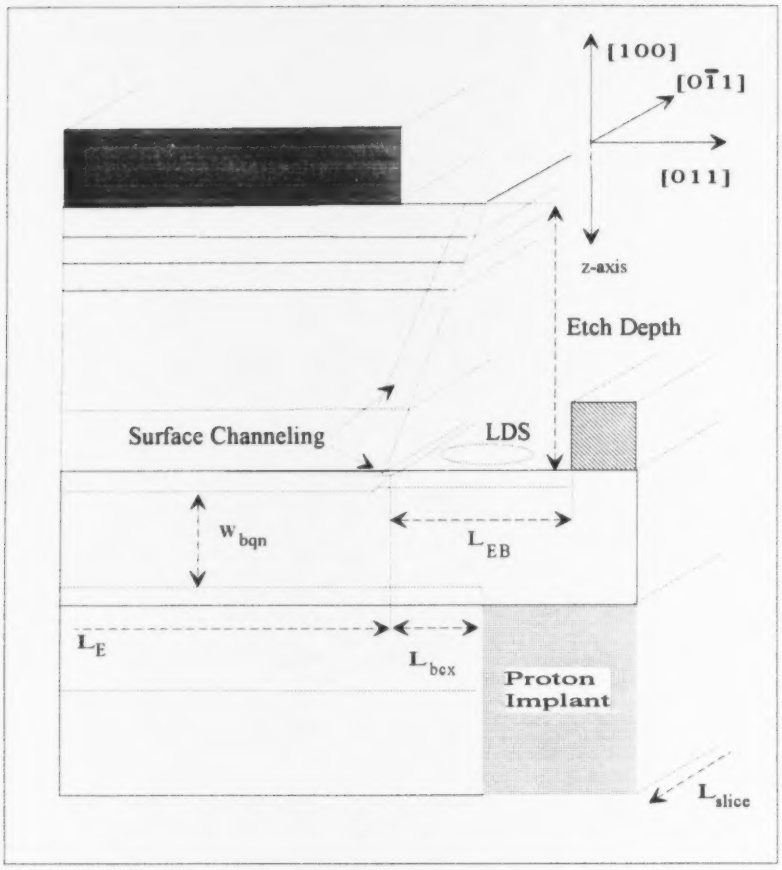

Figure 2.3: Illustrative cut away of an $Al_xGa_{1-x}As$ HBT showing surface and junction depletion regions and surface depletion layer two dimensional [41] channeling currents

Bulk recombination rate can be estimated for a device layer by a combination of deep level trap based non radiative Schockley Read Hall (SRH) , Auger and radiative recombination [27], with SRH estimated as

$$U_{SRH} = \frac{pn - n_i^2}{(n + n_t)\cdot\tau_p + (p + p_t)\cdot\tau_n} \qquad (2.5)$$

where representative electron and hole trap levels are assumed in the range of

$$n_t = 10^{13} \cdot cm^{-3} \tag{2.6}$$

$$p_t = 10^{13} \cdot cm^{-3} \tag{2.7}$$

and Auger recombination rate as

$$U_A = \left(A_p \cdot p + A_n \cdot n\right) \cdot \left(p \cdot n - n_i^2\right) \tag{2.8}$$

where representative Auger constants are taken as [27]

$$A_n = 10^{-31} \cdot \frac{cm^6}{s} \tag{2.9}$$

$$A_p = 10^{-31} \cdot \frac{cm^6}{s} \tag{2.10}$$

Radiative recombination rate is approximated by

$$U_R = B_R \cdot \left(p \cdot n - n_i^2\right) \tag{2.11}$$

where a representative radiative constant is taken as [27]

$$B_R = 10^{-11} \cdot \frac{cm^3}{s} \tag{2.12}$$

The total zone recombination rate is

$$U_Z = U_{SRH}\left(n, p, n_t, p_t, \tau_n, \tau_p, n_i\right) + \left(U_A\left(n, p, n_i, A_n, A_p\right) + U_R\left(n, p, n_i, B_R\right)\right) \tag{2.13}$$

giving the recombination current density for a layer of width w as

$$J_u = q \int_0^w U_z(z)\, dz \tag{2.14}$$

or in terms of average recombination rate for the layer as

$$J_u = q\, U_Z\left(n, p, n_t, p_t, \tau_n, \tau_p, n_i, A_n, A_p, B_R\right) \cdot w \tag{2.15}$$

Using the parameters of the previous section the average minority carrier concentration of the base quasi-neutral layer can be approximated as

$$n_{b\_av} = \frac{N_{b\_x}\left(n_{xs}, w_{bqn}, N_{Ab}, w_b, x_{bo}, x_{bw}, T\right)}{w_{bqn}} \tag{2.16}$$

where assuming the equilibrium intrinsic level $n_{io} = n_i(x=0, T_r)$ and emitter injection of minority carriers using equation 1.82, then the excess injected concentration can be estimated as

$$n_{xso} = n_{bo\_x}\left(N_b, x_{bo}=0, x_{bw}=0, T\right) \cdot e^{\frac{V_{eb} - \alpha_c \cdot 0.3 \cdot volt}{V_{th}(T)}} \tag{2.17}$$

Assuming a representative base dopant concentration level

$$N_{Ab}=10^{19}\cdot cm^{-3} \tag{2.18}$$

gives the estimated total bulk recombination in the base quasi neutral region as

$$J_{u\_bqn}=J_u\left(n_{b\_av}\left(n_{xs}, w_{bqn}, N_{Ab}, w_b, x_{bo}=0, x_{bw}=0, T_r\right), N_{Ab}, \tau_n, \tau_n, n_{io}, w_{bqn}\right) \tag{2.19}$$

where if the SRH electron lifetime is approximated by representative

$$\tau_n=1\cdot ns \tag{2.20}$$

and the SRH lifetime is assumed equal

$$\tau_p=\tau_n \tag{2.21}$$

and further using the recombination mechanism current densities

$$J_{u\_SRH}=q\cdot w\cdot U_{SRH}\left(n_{xso}\left(V_{eb}, N_{Ab}, T_r\right), N_{Ab}, n_t, p_t, \tau_n, \tau_p, n_{io}\right) \tag{2.22}$$

and assuming

$$J_{u\_A}=q\cdot w\cdot U_A\left(n_{xso}\left(V_{eb}, N_{Ab}, T_r\right), N_{Ab}, n_{io}, A_n, A_p\right) \tag{2.23}$$

with similarly

$$J_{u\_R} = q\, w\, U_R\left(n_{xso}, V_{eb}, N_{Ab}, T_r, N_{Ab}, n_{io}, B_R\right) \qquad (2.24)$$

The result is figure 2.4 where the relative magnitudes of the theoretical bulk kT recombination currents indicate SRH is dominant followed by radiative and then Auger recombination. With reference to the emitter base space charge region (scr) general factors affecting current gain (β) could include

- reduction of the conduction band barrier with respect to electron injection

- improved restriction of hole flow past the valence barrier into the emitter

- minimization of recombination in the emitter base scr

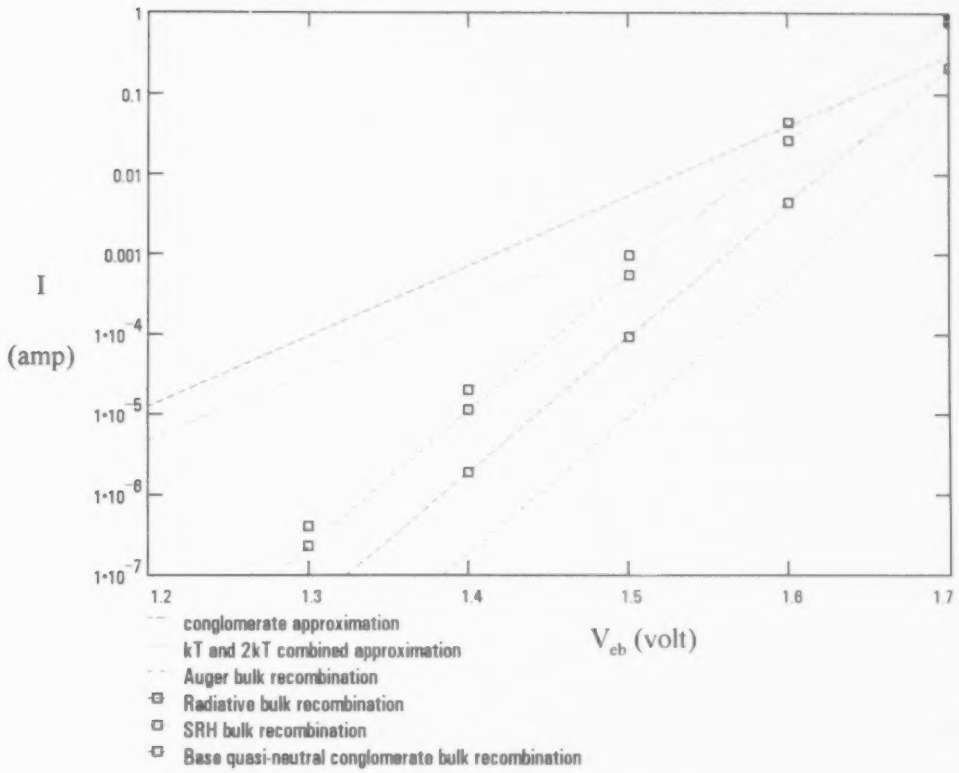

Figure 2.4: Theoretical base quasi-neutral layer recombination current densities compared to a parametric fit as a function of emitter base voltage assuming a base width of 100 nm and base quasi neutral region width of 90 nm

2.2 **Dopant Band Gap Narrowing**

Reduction of the conduction band barrier implies a local reduction in energy gap which will likely increase recombination and decrease the valence band barrier. Addressing the energy barrier (ΔE_{vbe}) to holes entering the emitter

$$\Delta E_{vbe} = q V_{eb} + \left(\psi_b + \alpha_c \Delta E_{gbe} + \Delta E_{vbgn} \right) \qquad (2.25)$$

where

$$\psi_b = \frac{E_{ge} + E_{gbo}}{2} - E_{Fne} + E_{Fpb} \qquad (2.26)$$

where E_{Fne} and E_{Fpb} are the quasi fermi levels (imrefs) in the emitter and base bulk at the edge of the space charge region and $\alpha_h \Delta E_{geb}$ is the proportion of the bandgap difference attributable to the valence band while ΔE_{vbgn} is due to base valence band narrowing from shallow impurity energy states close to the band edge [42] . Using an equation modified after [34], from experiments where N_b is assumed fully ionized and represents the hole concentration in the base region of interest, the extra energy levels are empirically estimated with units rationalization as

$$\Delta E_{vbgn} = 5.8 \cdot 10^{-13} \cdot \left(\frac{N_b}{cm^{-3}} \right)^{0.58} \cdot eV \qquad (2.27)$$

where it is assumed the accuracy of the equation is limited by the ionization energy level(s) of the donor or acceptor atoms at the points of intersection indicated in figure 2.5.

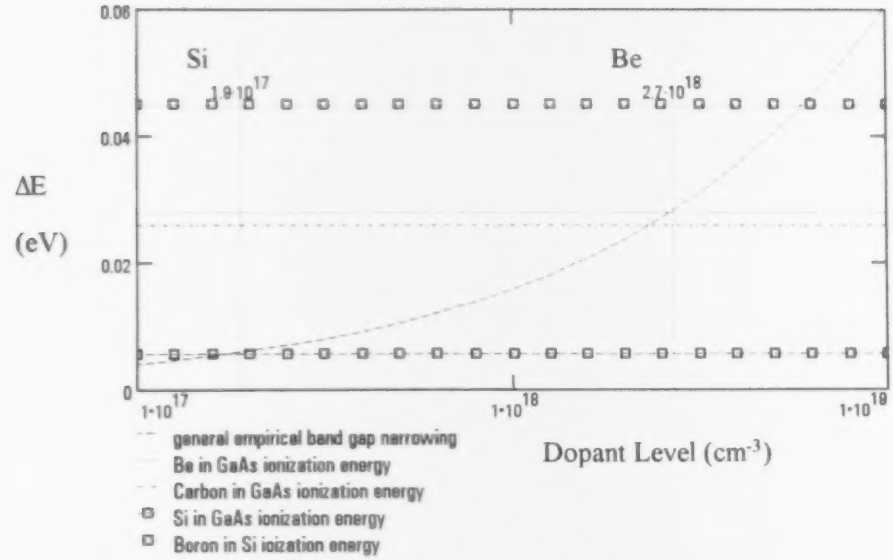

Figure 2.5: Empirical band gap narrowing approximation at 300 K for GaAs and Si

As $Al_xGa_{1-x}As$ alloy fraction x increases the donor ionization energy is assumed to vary as

$$E_d = E_{do} \cdot \left(\frac{\varepsilon_{s\_x}(x=0)}{\varepsilon_{s\_x}(x)} \right)^2 \cdot \frac{m_{de}(x,T)}{m_{de}(x=0,T_r)} \qquad (2.28)$$

and acceptor ionization energy as

$$E_a = E_{ao} \cdot \left(\frac{\varepsilon_{s\_x}(x=0)}{\varepsilon_{s\_x}(x)} \right)^2 \cdot \frac{m_{dh}(x)}{m_{dh}(x=0)} \qquad (2.29)$$

up to the range of x = 0.3. Where figure 2.6 indicates the potential for slightly enhanced

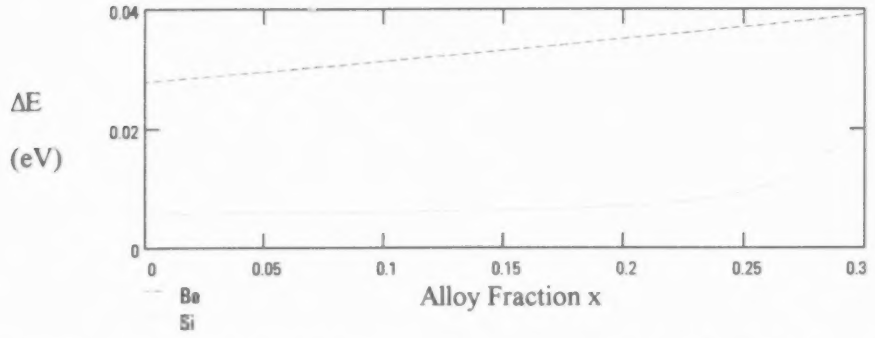

Figure 2.6: Empirical ionization energy approximation at 300 K for $Al_xGa_{1-x}As$ as a function of alloy fraction x.

bandgap narrowing for p and n type regions at increased alloy fraction.

2.3 Lateral Resistance Components

Base lateral resistance is composed of the sum of intrinsic, extrinsic and contact components. Characterizing a 1 micrometer cross section (L_{slice}) of a device the approximate base layer lateral resistances are based on the sheet resistance of the extrinsic base layer in ohms per square for p-type and n-type material. The sheet resistance is given by

$$R_{sh} = \frac{1}{q N \mu w} \qquad (2.30)$$

which upon substitution results in four equations.

P-type $Al_xGa_{1-x}As$ sheet resistance

$$R_{psh\_x} = R_{sh}\left(N_b, \mu_{p\_x}\left(N_b, x, T\right), w_b\right) \quad (2.31)$$

P-type silicon sheet resistance

$$R_{psh\_Si} = R_{sh}\left(N_b, \mu_{p\_Si}\left(N_b, T\right), w_b\right) \quad (2.32)$$

N-type $Al_xGa_{1-x}As$ sheet resistance

$$R_{nsh\_x} = R_{sh}\left(N_b, \mu_{n\_x}\left(N_b, x, T\right), w_b\right) \quad (2.33)$$

N-type silicon sheet resistance

$$R_{nsh\_Si} = R_{sh}\left(N_b, \mu_{n\_Si}\left(N_b, T\right), w_b\right) \quad (2.34)$$

The comparative plot of sheet resistance in figure 2.7 indicates a clear advantage for the n type GaAs over Si with approximately the same result for the p type of both.

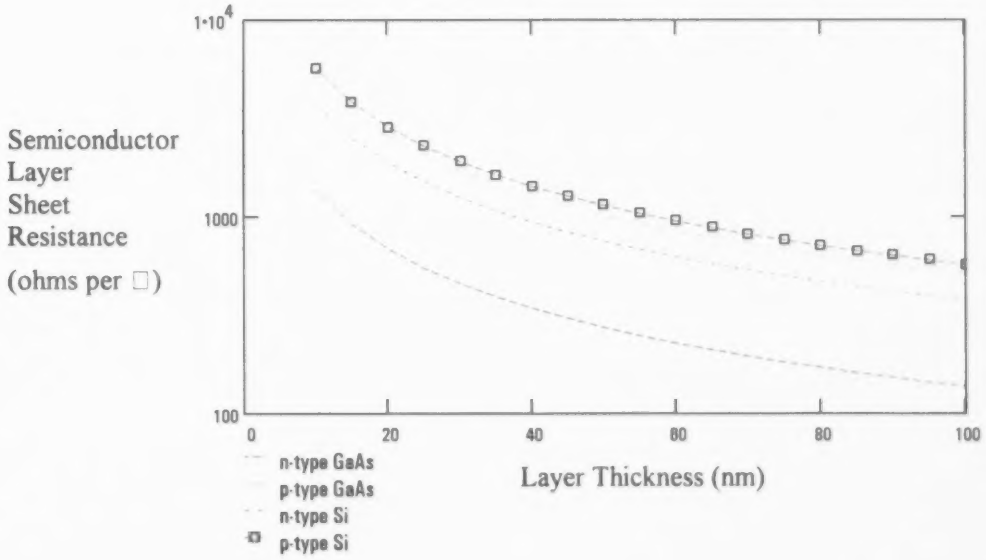

Figure 2.7: Semiconductor layer sheet resistance approximation for p and n type at a doping level of 10^{19} cm^{-3} as a function of layer width at 300 K

The intrinsic region lateral sheet resistance can be estimated by assuming a reduction in base layer sheet thickness due to the base to emitter and base to collector scr restricting lateral carrier flow as indicated in figure 2.8.

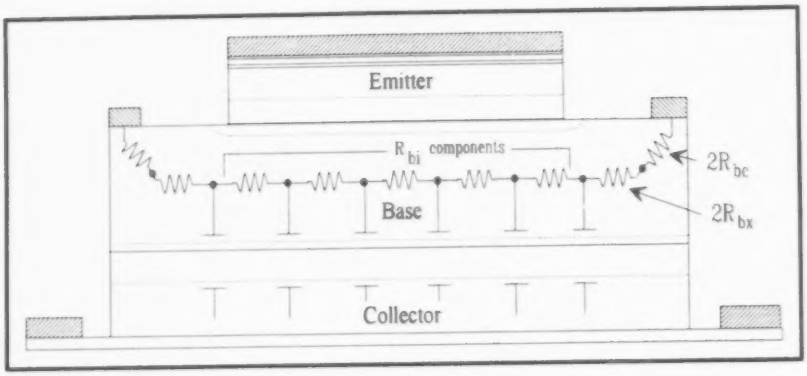

Figure 2.8: Schematic diagram of distributed base resistance and collector capacitance

The intrinsic base region, narrowed by bilateral scr regions can be estimated by using

$$w_{be\_he\_x} = \left[\frac{2 \cdot N_e \cdot \varepsilon_{s\_x}(x_e) \cdot \varepsilon_{s\_x}(x_{bo}) \cdot \left(V_\gamma(x_{bo}, x_e, N_b, N_e, T) - V_{eb} \right)}{q N_b \left(\varepsilon_{s\_x}(x_e) \cdot N_e + \varepsilon_{s\_x}(x_{bo}) \cdot N_b \right)} \right]^{\frac{1}{2}} \qquad (2.35)$$

with

$$w_{be\_ho\_Si} = w_d\left(V_{\alpha\_Si}(N_b, N_e, T), V_{eb}, \varepsilon_{Si}, N_b, N_e\right) \qquad (2.36)$$

and

$$w_{bc\_ho\_x} = w_d\left(V_{\alpha\_x}(x_{bw}, N_b, N_c, T), V_{bc}, \varepsilon_{s\_x}(x_{bw}), N_b, N_c\right) \qquad (2.37)$$

with

$$w_{bc\_ho\_Si} = w_d\left(V_{\alpha\_Si}\left(N_b, N_c, T\right), V_{bc}, \varepsilon_{Si}, N_b, N_c\right) \tag{2.38}$$

such that the base quasi neutral region width is estimated by

$$w_{bqn\_x} = w_b - \begin{pmatrix} w_{be\_he\_x}\left(V_{eb}, N_e, N_b, x_e, x_{bo}, T\right) \ldots \\ +w_{bc\_ho\_x}\left(V_{bc}, N_b, N_c, x_{bw}, T\right) \end{pmatrix} \tag{2.39}$$

and

$$w_{bqn\_Si} = w_b - \begin{pmatrix} w_{be\_ho\_Si}\left(V_{eb}, N_e, N_b, T\right) \ldots \\ +w_{bc\_ho\_Si}\left(V_{bc}, N_b, N_c, T\right) \end{pmatrix} \tag{2.40}$$

giving an approximate effective intrinsic base sheet resistance of

$$R_{sh\_bpi\_x} = R_{sh}\left(N_b, \mu_{p\_x}\left(N_b, x_{b\_av}, T\right), w_{bqn\_x}\left(V_{eb}, V_{bc}, N_e, N_b, N_c, x_e, x_{bo}, x_{bw}=0, w_b, T\right)\right) \tag{2.41}$$

and

$$R_{sh\_bpi\_Si} = R_{sh}\left(N_b, \mu_{p\_Si}\left(N_b, T\right), w_{bqn\_Si}\left(V_{eb}, V_{bc}, N_e, N_b, N_c, w_b, T\right)\right) \tag{2.42}$$

where assuming the same dopant levels the n-type intrinsic base sheet resistance would be

$$R_{sh\_bni\_x} = R_{sh}\left(N_b, \mu_{n\_x}\left(N_b, x_{b\_av}, T\right), w_{bqn\_x}\left(V_{eb}, V_{bc}, N_e, N_b, N_c, x_e, x_{bo}, x_{bw}=0, w_b, T\right)\right) \quad (2.43)$$

and

$$R_{sh\_bni\_Si} = R_{sh}\left(N_b, \mu_{n\_Si}\left(N_b, T\right), w_{bqn\_Si}\left(V_{eb}, V_{bc}, N_e, N_b, N_c, w_b, T\right)\right) \quad (2.44)$$

The intrinsic lateral base sheet resistance increases slightly as the base channel narrows with increasing collector scr width, similar to the depletion pinch of a FET. Initially using an empirical fit factor α_{rbi} to compensate for vertical current crowding near the emitter edge and assuming the lateral intrinsic base resistance is due to the sheet resistance in the intrinsic region combined with the bilateral symmetry of the base contacts then an approximation for the intrinsic resistance becomes

$$R_{bpi\_x} = 0.5 \cdot \alpha_{rbi} \left(\frac{L_E}{1 \cdot \mu m}\right) \cdot R_{sh\_bpi\_x}\left(V_{bc}, N_e, N_b, N_c, x_e, x_{bo}, w_b, T\right) \quad (2.45)$$

and

$$R_{bpi\_Si} = 0.5 \cdot \alpha_{rbi} \left(\frac{L_E}{1 \cdot \mu m}\right) \cdot R_{sh\_bpi\_Si}\left(V_{bc}, N_e, N_b, N_c, w_b, T\right) \quad (2.46)$$

and for n-type

$$R_{bni\_x} = 0.5 \cdot \alpha_{rbi} \cdot \left(\frac{L_E}{1 \cdot \mu m} \right) \cdot R_{sh\_bni\_x}\left(V_{bc}, N_e, N_b, N_c, x_e, x_{bo}, w_b, T\right) \qquad (2.47)$$

and

$$R_{bni\_Si} = 0.5 \cdot \alpha_{rbi} \cdot \left(\frac{L_E}{1 \cdot \mu m} \right) \cdot R_{sh\_bni\_Si}\left(V_{bc}, N_e, N_b, N_c, w_b, T\right) \qquad (2.48)$$

The extrinsic connections for the two base types assuming a short gap (L_{EB}) to the base metal contacts with an assumed average alloy level for the base and negligible channel pinch effect from the surface or base collector scr due to idealized fabrication related considerations becomes

$$R_{bpx\_x} = 0.5 \cdot \left(\frac{L_{EB}}{1 \cdot \mu m} \right) \cdot R_{psh\_x}\left(N_b, x_{b\_av}, w_b, T\right) \qquad (2.49)$$

and

$$R_{bpx\_Si} = 0.5 \cdot \left(\frac{L_{EB}}{1 \cdot \mu m} \right) \cdot R_{psh\_Si}\left(N_b, w_b, T\right) \qquad (2.50)$$

with for n-type

$$R_{bnx\_x} = 0.5 \cdot \left(\frac{L_{EB}}{1 \cdot \mu m} \right) \cdot R_{nsh\_x}\left(N_b, x_{b\_av}, w_b, T\right) \qquad (2.51)$$

and

$$R_{bnx\_Si} = 0.5 \cdot \left(\frac{L_{EB}}{1 \cdot \mu m} \right) \cdot R_{nsh\_Si}\left(N_b, w_b, T\right) \qquad (2.52)$$

Finally the p and n-type metal ohmic contact resistances are estimated after [43] using representative contact resistances from GaAs for all semiconductor types as

$$R_{bpc\_x} = \frac{\sqrt{R_{psh\_x}(N_{b'}, x_{bo}, w_{b'}, T) \cdot \rho_{cp}}}{2 \cdot \mu m^{-1}} \cdot \coth\left[L_B \cdot \sqrt{\frac{\rho_{cp}}{R_{psh\_x}(N_{b'}, x_{bo}, w_{b'}, T)}}\right] \tag{2.53}$$

and

$$R_{bpc\_Si} = \frac{\sqrt{R_{psh\_Si}(N_{b'}, w_{b'}, T) \cdot \rho_{cp}}}{2 \cdot \mu m^{-1}} \cdot \coth\left[L_B \cdot \sqrt{\frac{\rho_{cp}}{R_{psh\_Si}(N_{b'}, w_{b'}, T)}}\right] \tag{2.54}$$

with for n-type

$$R_{bnc\_x} = \frac{\sqrt{R_{nsh\_x}(N_{b'}, x_{bo}, w_{b'}, T) \cdot \rho_{cn}}}{2 \cdot \mu m^{-1}} \cdot \coth\left[L_B \cdot \sqrt{\frac{\rho_{cn}}{R_{nsh\_x}(N_{b'}, x_{bo}, w_{b'}, T)}}\right] \tag{2.55}$$

and

$$R_{bnc\_Si} = \frac{\sqrt{R_{nsh\_Si}(N_{b'}, w_{b'}, T) \cdot \rho_{cn}}}{2 \cdot \mu m^{-1}} \cdot \coth\left[L_B \cdot \sqrt{\frac{\rho_{cn}}{R_{nsh\_Si}(N_{b'}, w_{b'}, T)}}\right] \tag{2.56}$$

where L_B is the length of the contact metalization on top of the extrinsic base layer, after the transmission line model of [43]. Summing the total approximate lateral base

resistance per micrometer of emitter for the four cases starting with

$$R_{Bp\_x} = R_{bpi\_x}\left(L_E, \alpha_{rbi}, V_{bc}, N_e, N_b, N_c, x_e, x_{bo}, w_b, T\right) \ldots + R_{bpx\_x}\left(L_{EB}, N_b, x_{bo}, x_{bw}, w_b, T\right) \ldots + R_{bpc\_x}\left(L_B, N_b, x_{bo}, w_b, T\right) \quad (2.57)$$

and

$$R_{Bp\_Si} = R_{bpi\_Si}\left(L_E, \alpha_{rbi}, V_{bc}, N_e, N_b, N_c, w_b, T\right) \ldots + R_{bpx\_Si}\left(L_{EB}, N_b, w_b, T\right) \ldots + R_{bpc\_Si}\left(L_B, N_b, w_b, T\right) \quad (2.58)$$

with for n-type

$$R_{Bn\_x} = R_{bni\_x}\left(L_E, \alpha_{rbi}, V_{bc}, N_e, N_b, N_c, x_e, x_{bo}, w_b, T\right) \ldots + R_{bnx\_x}\left(L_{EB}, N_b, x_{bo}, x_{bw}, w_b, T\right) \ldots + R_{bnc\_x}\left(L_B, N_b, x_{bo}, w_b, T\right) \quad (2.59)$$

and

$$R_{Bn\_Si} = R_{bni\_Si}\left(L_E, \alpha_{rbi}, V_{bc}, N_e, N_b, N_c, w_b, T\right) \ldots + R_{bnx\_Si}\left(L_{EB}, N_b, w_b, T\right) \ldots + R_{bnc\_Si}\left(L_B, N_b, w_b, T\right) \quad (2.60)$$

From the fully parameterized version of the preceding equations, figure 2.9, on the next page, indicates the GaAs n-type base material has a roughly 2:1 advantage for lateral base resistance components.

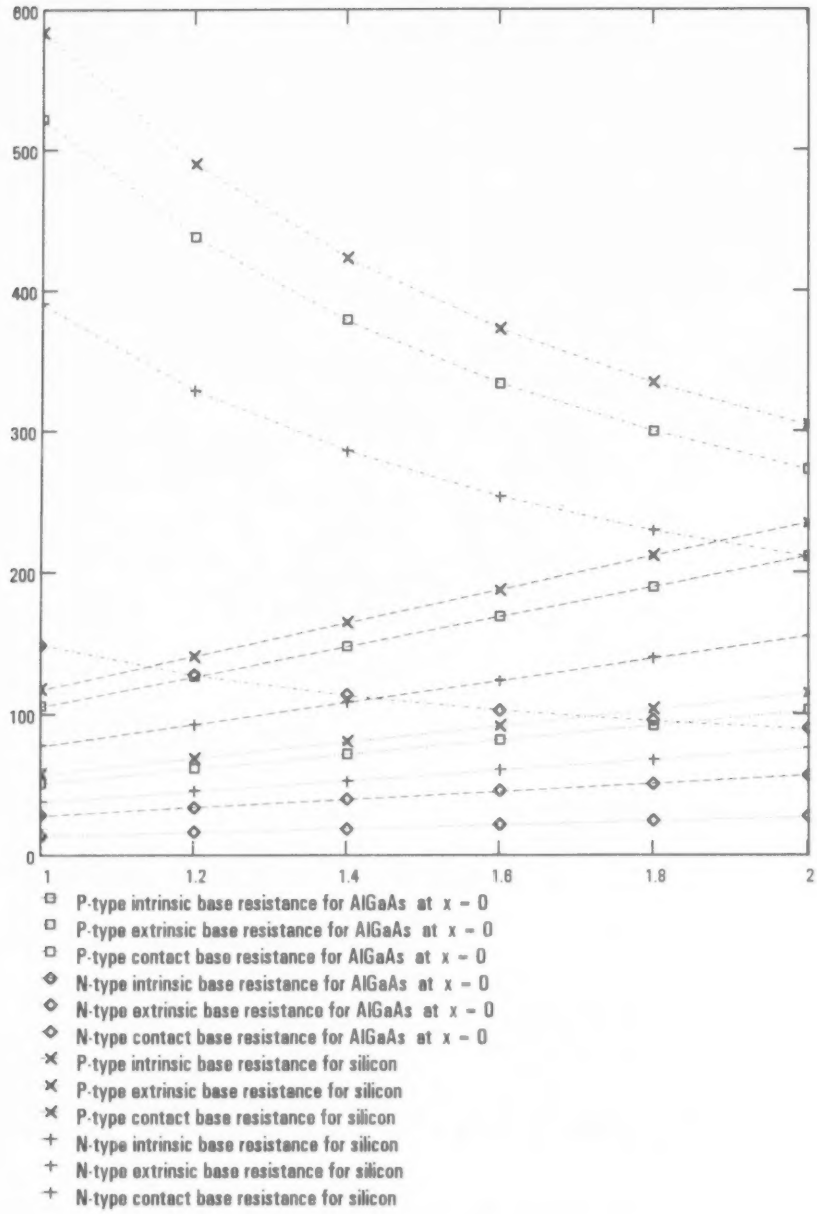
600
500
400
300
200
100
0
1
1.2
1.4
1.6
1.8
2
P-type intrinsic base resistance for AlGaAs at x = 0
P-type extrinsic base resistance for AlGaAs at x = 0
P-type contact base resistance for AlGaAs at x = 0
N-type intrinsic base resistance for AlGaAs at x = 0
N-type extrinsic base resistance for AlGaAs at x = 0
N-type contact base resistance for AlGaAs at x = 0
P-type intrinsic base resistance for silicon
P-type extrinsic base resistance for silicon
P-type contact base resistance for silicon
N-type intrinsic base resistance for silicon
N-type extrinsic base resistance for silicon
N-type contact base resistance for silicon

Figure 2.9: Base layer sheet resistance components for p and n type at as a function of lateral distance with zero base alloy content at 300 K

2.4 Junction Capacitance Components

Assuming that the self aligned process implied in figure 2.3 also employs an intrinsic region definition implant [16] or two stage MBE process [44] that limits the lateral extent of the base to collector or emitter layer interface, then the capacitance due to the ionic charge separation of the space charge region can be estimated by using a process empirical fit factor (α_{eb}) in the relation

$$L_{bcx}=\alpha_{eb}\cdot L_E \tag{2.61}$$

in

$$A_{bc}=L_{slice}\left(L_E+2\cdot L_{bcx}\left(\alpha_{eb},L_E\right)\right) \tag{2.62}$$

Continuing with the comparative analysis and assuming a collector heterotype homojunction with no alloy fraction for the unit slice of an emitter finger combined with equivalent doping for all devices, currently subsuming equivalent process specific high current gain due to the emitter strategy for all devices the homojunction collector-base scr width becomes

$$w_{cb\_ho\_x}=w_d\left(V_{\alpha\_x}\left(x_c,N_b,N_c,T\right),V_{bc},\varepsilon_{s\_x}\left(x_c\right),N_c,N_b\right) \tag{2.63}$$

such that the combined base-collector total scr width is

$$w_{bct\_ho\_x} = w_{bc\_ho\_x}(V_{bc}, N_b, N_c, x_{bw}, T) + w_{cb\_ho\_x}(V_{bc}, N_b, N_c, x_c, T) \quad (2.64)$$

and for Si

$$w_{cb\_ho\_Si} = w_d(V_{\alpha\_Si}(N_b, N_c, T), V_{bc}, \varepsilon_{Si}, N_c, N_b) \quad (2.65)$$

such that

$$w_{bct\_ho\_Si} = w_d(V_{\alpha\_Si}(N_b, N_c, T), V_{bc}, \varepsilon_{Si}, N_b, N_c) + w_d(V_{\alpha\_Si}(N_b, N_c, T), V_{bc}, \varepsilon_{Si}, N_c, N_b) \quad (2.66)$$

where using an effective base capacitance area A_{bc} as a function of emitter dimension L_E and process specific containment parameter α_{eb} the intrinsic plus localized extrinsic base to collector capacitance is approximated by

$$C_{bc\_x} = A_{bc}(\alpha_{eb}, L_E) \cdot \left[\frac{\varepsilon_{s\_x}(x_c)}{(w_{bc\_ho\_x}(V_{bc}, N_b, N_c, x_{bw}, T) + w_{cb\_ho\_x}(V_{bc}, N_b, N_c, x_c, T))} \right] \quad (2.67)$$

and for Si

$$C_{bc\_Si} = A_{bc}(\alpha_{eb}, L_E) \cdot \left[\frac{\varepsilon_{Si}}{(w_{bc\_ho\_Si}(V_{bc}, N_b, N_c, T) + w_{cb\_ho\_Si}(V_{bc}, N_b, N_c, T))} \right] \quad (2.68)$$

for the unit slice. Using the slice technique entire devices could be constructed by arranging the preferred slice model or fractions of it in the desired layout with modified slice model for finger ends in the most appropriate pattern for a particular part of the analog circuit taking into account orientation and thermal effects [45] then simulating the operation of the entire circuit or representative derivatives thereof. Improvements could then be made by directly adjusting the device model and layout excluding some extrinsic parasitics and/or accurate passive components as separate issues for current purposes.

2.5 **Junction Voltages**

Continuing with the model with consideration that the majority current controlling emitter base bias voltage is required as a function of current density, the relative thermionic emission of electrons and holes [46] can be used to approximate V_{eb} for the devices assuming the barrier is a combination of built in and heterojunction offset voltages while neglecting tunneling current. For an abrupt device

$$V_{npn\_xa} = V_{th}(T) \cdot \ln\left(\frac{J}{A_R\left(m_{de}\left(x_e, T\right)\right) \cdot T^2}\right) + \left[V_\gamma\left(x_{bo}, x_e, N_b, N_e, T\right) + \frac{\alpha_c \cdot \left(E_\Gamma\left(x_e, T\right) - E_\Gamma\left(x_{bo}, T\right)\right)}{q}\right] \quad (2.69)$$

or assuming a grade fit parameter α_{cg} which reduces the barrier height as indicated above as a function of the width and profile of the graded region

$$V_{npn\_xg} = V_{th}(T)\cdot\ln\left(\frac{J}{A_R\left(m_{de}(x_e,T)\right)\cdot T^2}\right) + \left[V_\gamma(x_{bo},x_e,N_b,N_e,T) + \frac{\alpha_{cg}\cdot\alpha_c\cdot\left(E_\Gamma(x_e,T) - E_\Gamma(x_{bo},T)\right)}{q}\right] \tag{2.70}$$

with the Si device emitter base assumed as a heterotype homojunction equivalently for comparison as

$$V_{npn\_Si} = V_{th}(T)\cdot\ln\left(\frac{J}{A_R\left(m_{de\_Si}\right)\cdot T^2}\right) + V_{\alpha\_Si}(N_b,N_e,T) \tag{2.71}$$

with similarly for the pnp devices

$$V_{pnp\_xe} = V_{th}(T)\cdot\ln\left(\frac{J}{A_R\left(m_{dh}(x_e)\right)\cdot T^2}\right) + \left[V_\gamma(x_{bo},x_e,N_b,N_e,T) + \frac{\alpha_v\cdot\left(E_\Gamma(x_e,T) - E_\Gamma(x_{bo},T)\right)}{q}\right] \tag{2.72}$$

and for the graded version using α_{vg}

$$V_{pnp\_xg} = V_{th}(T)\cdot\ln\left(\frac{J}{A_R\left(m_{dh}(x_e)\right)\cdot T^2}\right) + \left[V_\gamma(x_{bo},x_e,N_b,N_e,T) + \frac{\alpha_{vg}\cdot\alpha_v\cdot\left(E_\Gamma(x_e,T) - E_\Gamma(x_{bo},T)\right)}{q}\right] \tag{2.73}$$

with the Si device as

$$V_{pnp\_Si} = V_{th}(T) \cdot \ln\left(\frac{J}{A_R \cdot m_{dh\_Si} \cdot T^2}\right) + V_{\alpha\_Si}(N_b, N_e, T) \qquad (2.74)$$

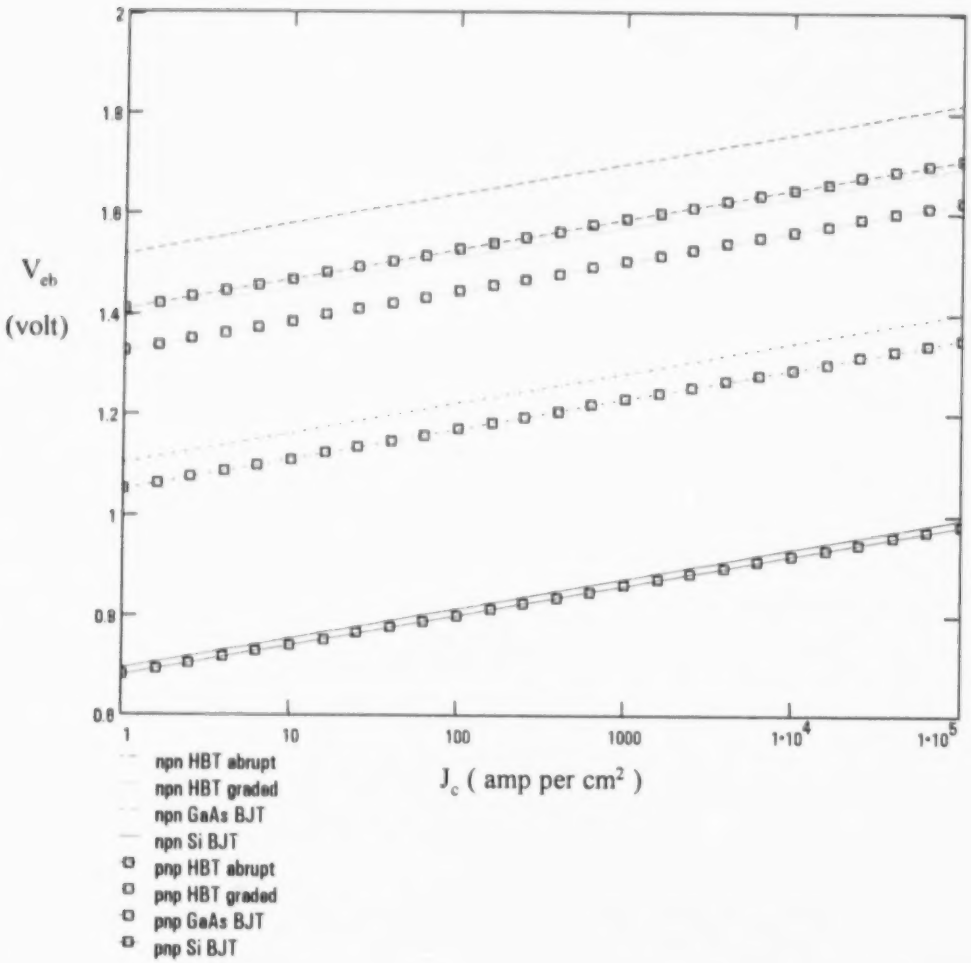

Figure 2.10: Theoretical emitter base voltage for npn and pnp devices as a function of current density at 300 K with x = 0.3 for HBTs and 0 for GaAs BJTs in the emitter and zero base alloy with the same doping parameters as figure 2.9.

giving figure 2.10 from which it is apparent, from a power dissipation perspective that a pnp GaAs heterotype homojunction, trace 7, is the most desirable of the non Si devices followed by a npn GaAs heterotype homojunction.

2.6 **Emitter Charging Time**

Proceeding further towards the comparative frequency analysis model with emitter scr width approximations the heterotype heterojunction width modified after [47] is

$$w_{eb\_he\_x} = \left[\frac{2 \cdot N_b \cdot \varepsilon_{s\_x}(x_e) \cdot \varepsilon_{s\_x}(x_{bo}) \cdot (V_\gamma(x_{bo}, x_e, N_b, N_e, T) - V_{eb})}{q N_e \cdot (\varepsilon_{s\_x}(x_e) \cdot N_e + \varepsilon_{s\_x}(x_{bo}) \cdot N_b)} \right]^{\frac{1}{2}} \tag{2.75}$$

where it should be noted that V_{eb} is limited by V_γ giving the total emitter base depletion width as

$$w_{ebt\_he\_x} = w_{eb\_he\_x}(V_{eb}, N_e, N_b, x_e, x_{bo} = 0, T) + w_{be\_he\_x}(V_{eb}, N_e, N_b, x_e, x_{bo} = 0, T) \tag{2.76}$$

and for Si as

$$w_{ebt\_ho\_Si} = w_d(V_{\alpha\_Si}(N_b, N_e, T), V_{eb}, \varepsilon_{Si}, N_e, N_b) + w_d(V_{\alpha\_Si}(N_b, N_e, T), V_{eb}, \varepsilon_{Si}, N_b, N_e) \tag{2.77}$$

Now we are in a position to assemble the main components of τ_{ec} for the devices starting with the n-type emitters using as before the charging time for the emitter and collector base capacitances, neglecting the diffusion capacitance for basic comparative purposes, giving for the graded emitter HBT

$$\tau_{e\_npn\_xg} = \frac{V_{th}(T_r)}{J} \cdot \left[\frac{\varepsilon_{s\_x}(x_e)}{w_{ebt\_he\_x}(V_{npn\_xg}(J, \alpha_{cg}, N_e, N_b, x_e, x_{bo}=0, T), N_e, N_b, x_e, T)} \cdots + \frac{\varepsilon_{s\_x}(x_c=0)}{w_{bct\_ho\_x}(V_{bc}, N_b, N_c, x_{bw}=0, x_c=0, T)} \right] \tag{2.78}$$

and for the Si BJT

$$\tau_{e\_npn\_Si} = \frac{V_{th}(T_r)}{J} \cdot \left[\frac{\varepsilon_{Si}}{w_{ebt\_ho\_Si}(V_{npn\_Si}(J, N_e, N_b, T), N_e, N_b, T)} \cdots + \frac{\varepsilon_{Si}}{w_{bct\_ho\_Si}(V_{bc}, N_b, N_c, T)} \right] \tag{2.79}$$

with the p-type emitters as

$$\tau_{e\_pnp\_xg} = \frac{V_{th}(T_r)}{J} \cdot \left[\frac{\varepsilon_{s\_x}(x_e)}{w_{ebt\_he\_x}(V_{pnp\_xg}(J, \alpha_{vg}, N_e, N_b, x_e, x_{bo}=0, T), N_e, N_b, x_e, T)} \cdots + \frac{\varepsilon_{s\_x}(x_c=0)}{w_{bct\_ho\_x}(V_{bc}, N_b, N_c, x_{bw}=0, x_c=0, T)} \right] \tag{2.80}$$

and for the pnp Si BJT

$$\tau_{e\_pnp\_Si} = \frac{V_{th}(T_r)}{J} \cdot \left| \frac{\varepsilon_{Si}}{w_{ebt\_ho\_Si}(V_{pnp\_Si}, J, N_e, N_b, T, N_e, N_b, T)} \cdots + \frac{\varepsilon_{Si}}{w_{bct\_ho\_Si}(V_{bc}, N_b, N_c, T)} \right| \tag{2.81}$$

giving figure 2.11, indicating a capacitance penalty, and highlighting the phenomenon of a collapsed scr at high current density with implications for a graded HBT where the scr is within the grade region [49]. Assuming the built in voltage has been countered by the applied bias in the case of a heterotype homojunction the conduction and valence bands would be approximately horizontal through the emitter base scr. In the case of the abrupt heterotype heterojunction the bulk on either side of the junction is assumed to be aligned as in the homojunction case, however the band discontinuities from the alloy change remain blocking the flow of carriers in both directions. As the capacitance is calculated using the built in voltage a new approach should be adopted for biasing beyond or even near this point for accurate results [50]. In the case of the graded HBT where the width of the grade is within the collapsing emitter scr a tendency to the homojunction situation will likely occur with specific results dependent on the grade parameters leading to enhanced degradation of current gain. It should also be noted that high current induced base push out and high current thermal effects [51] due in part to the high thermal resistivity of GaAs are associated with a rapid fall off of current gain and cut off frequency in experimental devices.

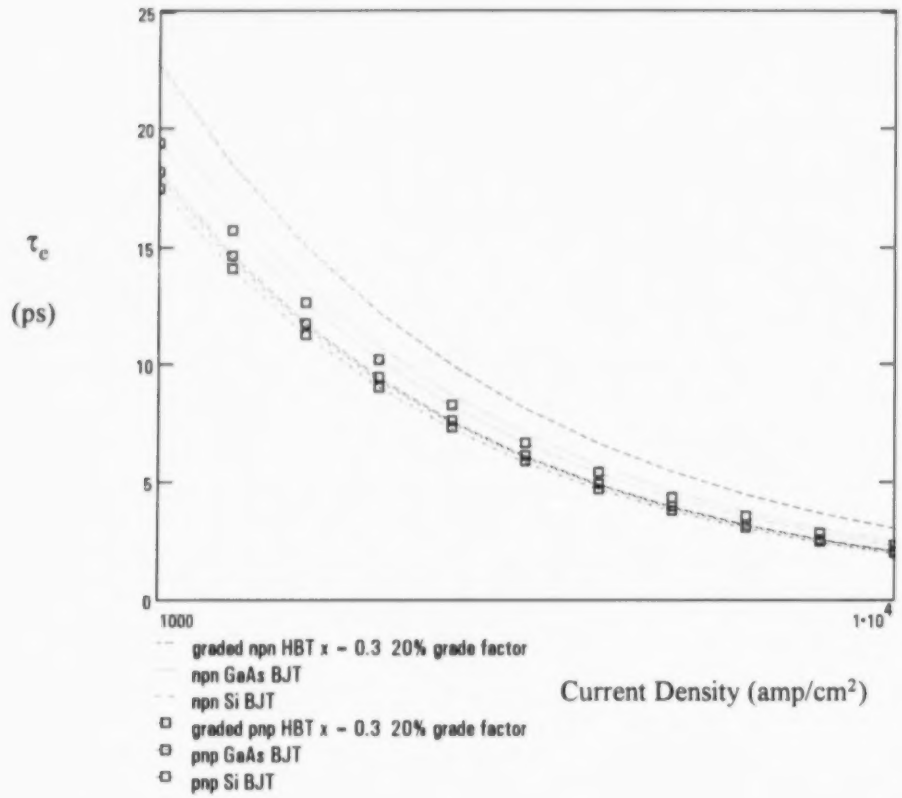

Figure 2.11: Theoretical emitter charging time for npn and pnp devices as a function of current density at 300 K with x = 0.3 and 0 in the emitter and zero base alloy with the same doping parameters as figure 2.10.

2.7 **Base Transit Time**

Proceeding to the base region, where it is assumed that for a given thermionically generated current density J the excess carrier concentration n_{xsj} at the imaginary line on the base side of the emitter base scr for a zero alloy p-type base device is approximated,

using equation 1.76, by

$$n_{xsj\_x} = \frac{J_n}{qD_{n\_x}(N_b, x_{be}=0, T)} \cdot \frac{\zeta_{AlGaAs}(w_{bqn\_x}(V_{eb}, V_{bc}, N_e, N_b, N_c, x_e=0, x_{bo}=0, x_{bw}=0, w_b, T), N_b, w_b, x_{bo}=0, x_{bw}=0, T)}{r_{b1\_x}(N_b, w_b, x_{bo}=0, x_{bw}=0, T) + r_{b2\_x}(N_b, w_b, x_{bo}=0, x_{bw}=0, T)}$$

(2.82)

where J_n is the minority carrier current at the emitter scr edge of the base and, using equation 1.77, for Si

$$n_{xsj\_Si} = \frac{J_n}{qD_{n\_Si}(N_b, T)} \cdot \frac{\zeta_{Si}(w_{bqn\_Si}(V_{eb}, V_{bc}, N_e, N_b, N_c, w_b, T), N_b, w_b, T)}{r_{b1\_Si}(N_b, T) + r_{b2\_Si}(N_b, T)} \quad (2.83)$$

such that for an p-type GaAs base

$$\tau_{b\_n\_x} = \frac{qN_{b\_x}(n_{xsj\_x}(J_n, N_e, N_b, N_c, w_b, T), w_{bqn\_x}(V_{eb}, V_{bc}, N_e, N_b, N_c, x_e=0, x_{bo}=0, x_{bw}=0, w_b, T), N_b, w_b, x_{bo}=0, x_{bw}=0, T)}{J_n}$$

(2.84)

and for an n-type Si base

$$\tau_{b\_n\_Si} = \frac{qN_{b\_Si}(n_{xsj\_Si}(J_n, N_e, N_b, N_c, w_b, T), w_{bqn\_Si}(V_{eb}, V_{bc}, N_e, N_b, N_c, w_b, T), N_b, w_b, T)}{J_n} \quad (2.85)$$

for comparative purposes it is assumed that for the GaAs n-type base

$$\tau_{b\_p\_x} = \frac{\mu_{n\_x}(N_b, x=0, T)}{\mu_{p\_x}(N_b, x=0, T)} \cdot \tau_{b\_n\_x}(J_n, N_e, N_b, N_c, w_b, T) \qquad (2.86)$$

and equivalently for Si

$$\tau_{b\_p\_Si} = \frac{\mu_{n\_Si}(N_b, T)}{\mu_{p\_Si}(N_b, T)} \cdot \tau_{b\_n\_Si}(J_n, N_e, N_b, N_c, w_b, T) \qquad (2.87)$$

indicating in figure 2.12 significant advantage for the npn p-type GaAs base.

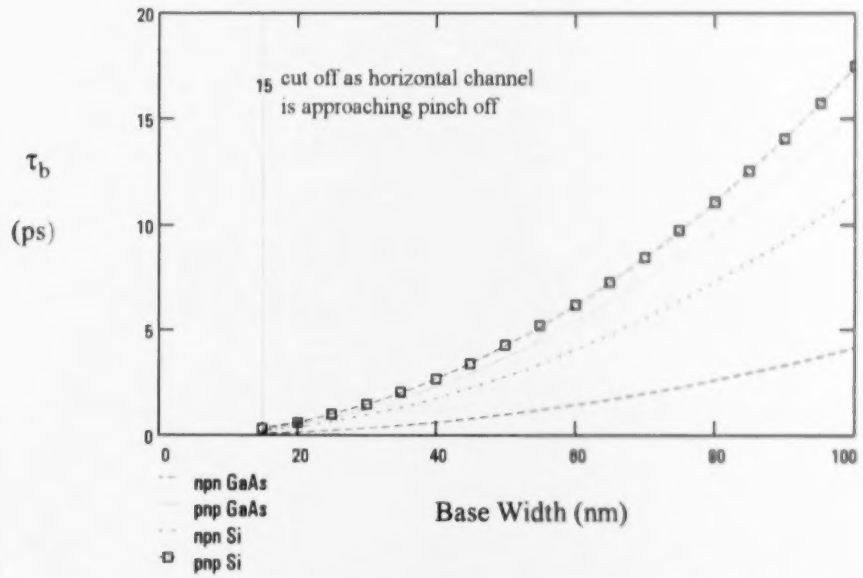

Figure 2.12: Theoretical delay components for npn and pnp devices with zero base field as a function of base width using $N_c = 10^{17}$ cm^{-3} and equivalent parameters to figures 2.9 to 2.11

2.8 Collector Transit Time

In the GaAs heterotype homojunction collector it is assumed [52] for comparative purposes based on mobility in the collector scr, that

$$\tau_{sc\_npn\_x} = \frac{w_{cb\_ho\_x}(V_{bc}, N_b, N_c, x_c=0, T)^2}{2 \cdot \mu_{n\_x}(N_c, x_c=0, T) \cdot (V_{bc} + V_{\alpha\_x}(x=0, N_b, N_c, T))} \tag{2.88}$$

and for Si

$$\tau_{sc\_npn\_Si} = \frac{w_{cb\_ho\_Si}(V_{bc}, N_b, N_c, T)^2}{2 \cdot \mu_{n\_Si}(N_c, T) \cdot (V_{bc} + V_{\alpha\_Si}(N_b, N_c, T))} \tag{2.89}$$

and in the pnp case that

$$\tau_{sc\_pnp\_x} = \frac{w_{cb\_ho\_x}(V_{bc}, N_b, N_c, x_c=0, T)^2}{2 \cdot \mu_{p\_x}(N_c, x_c=0, T) \cdot (V_{bc} + V_{\alpha\_x}(x=0, N_b, N_c, T))} \tag{2.90}$$

and for Si

$$\tau_{sc\_pnp\_Si} = \frac{w_{cb\_ho\_Si}(V_{bc}, N_b, N_c, T)^2}{2 \cdot \mu_{p\_Si}(N_c, T) \cdot (V_{bc} + V_{\alpha\_Si}(N_b, N_c, T))} \tag{2.91}$$

such that figure 2.13 indicates an apparent advantage for the npn devices, however high field scattering is not taken into account here, which will move the npn HBT τ_{sc} higher up on the time scale [53].

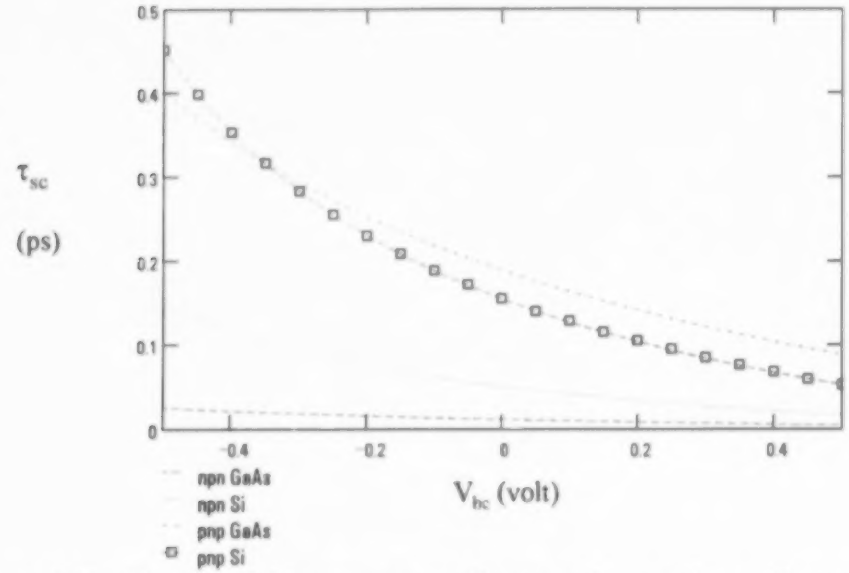

Figure 2.13: Theoretical delay components for npn and pnp devices with zero base field as a function of base collector voltage using $N_c = 10^{17}$ cm^{-3} and equivalent parameters of figures 2.9 to 2.12

The avalanche ionization break down voltage in the collector scr is complicated in the case of GaAs bipolar devices due to microplasma formation around lattice defects [54], however in general involves similar, well understood, compromises to Si BJT devices.

2.9 Cutoff Frequency

Proceeding to a comparison of the cutoff frequency [55] by assembling the delay components for the graded emitter npn HBT

$$f_{t\_npn\_xg} := \frac{1}{2\cdot\pi\cdot\left(\begin{array}{l}\tau_{e\_npn\_xg}\left(J_n, \alpha_{cg}, V_{bc}, N_e, N_b, N_c, x_e, T\right)\ldots \\ +\tau_{b\_n\_x}\left(J_n, N_e, N_b, N_c, w_b, T\right)\ldots \\ +\tau_{sc\_npn\_x}\left(V_{bc}, N_b, N_c, T\right)\end{array}\right)} \tag{2.92}$$

and Si BJT

$$f_{t\_npn\_Si} := \frac{1}{2\cdot\pi\cdot\left(\begin{array}{l}\tau_{e\_npn\_Si}\left(J_n, V_{bc}, N_e, N_b, N_c, T\right)\ldots \\ +\tau_{b\_n\_Si}\left(J_n, N_e, N_b, N_c, w_b, T\right)\ldots \\ +\tau_{sc\_npn\_Si}\left(V_{bc}, N_b, N_c, T\right)\end{array}\right)} \tag{2.93}$$

with the pnp devices similarly as

$$f_{t\_pnp\_xg} := \frac{1}{2\cdot\pi\cdot\left(\begin{array}{l}\tau_{e\_pnp\_xg}\left(J_p, \alpha_{vg}, V_{bc}, N_e, N_b, N_c, x_e, T\right)\ldots \\ +\tau_{b\_p\_x}\left(J_p, N_e, N_b, N_c, w_b, T\right)\ldots \\ +\tau_{sc\_pnp\_x}\left(V_{bc}, N_b, N_c, T\right)\end{array}\right)} \tag{2.94}$$

and

$$f_{t\_pnp\_Si} := \frac{1}{2\cdot\pi\cdot\left(\begin{array}{l}\tau_{e\_pnp\_Si}\left(J_p, V_{bc}, N_e, N_b, N_c, T\right)\ldots \\ +\tau_{b\_p\_Si}\left(J_p, N_e, N_b, N_c, w_b, T\right)\ldots \\ +\tau_{sc\_pnp\_Si}\left(V_{bc}, N_b, N_c, T\right)\end{array}\right)} \tag{2.95}$$

giving figure 2.14, using 10^5 amp per cm^2, and indicating a convergence of cutoff frequency as the base width is reduced to 15 nm. However at 50 nm width the graded npn HBT device is in favour by a factor of about 2:1 over an equivalently doped npn Si BJT, but comes in under the equivalent GaAs BJT by a small margin. A comparative estimate for theoretical vs. experimental proton and nonproton implanted HBT devices can be found in [56].

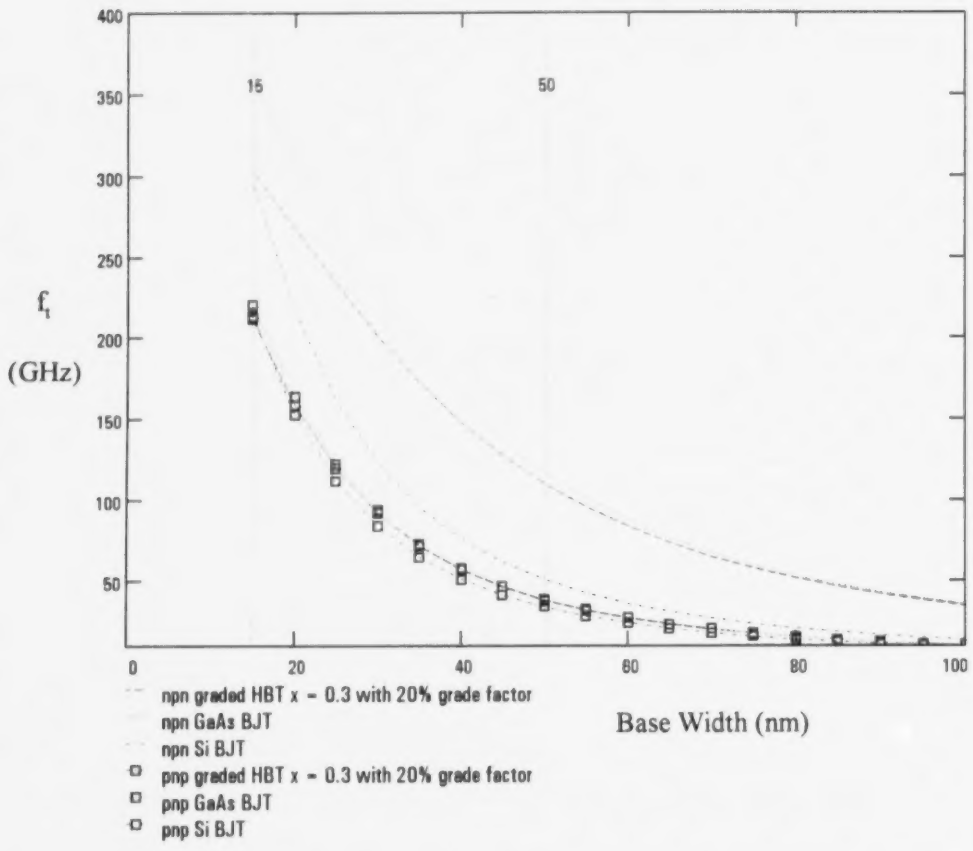

Figure 2.14: Theoretical f_t for npn and pnp devices with zero base field as a function of base width at $V_{bc} = 0$ volt and with equivalent parameters to figures 2.9 to 2.13

2.10 **Maximum Frequency of Oscillation**

If we now compare the plane of the wafer in terms of basic lateral carrier movement [57] then assembling components for an equivalent set of devices we have

$$f_{m\_npn\_xg} := \left(\frac{f_{t\_npn\_xg}(J_n, \alpha_{cg}, x_e, V_{bc}, N_e, N_b, N_c, w_b, T)}{8 \cdot \pi \cdot R_{Bp\_x}(L_E, \alpha_{rbi} := 0.2, L_{EB}, L_B, V_{bc}, N_e, N_b, N_c, x_e, x_{bo} := 0, x_{bw} := 0, w_b, T) \cdot C_{bc\_x}(L_E, \alpha_{eb}, V_{bc}, N_b, N_c, x_{bw} := 0, x_c := 0, T)} \right)^{\frac{1}{2}}$$

(2.96)

and

$$f_{m\_npn\_Si} := \left(\frac{f_{t\_npn\_Si}(J_n, V_{bc}, N_e, N_b, N_c, w_b, T)}{8 \cdot \pi \cdot R_{Bp\_Si}(L_E, \alpha_{rbi} := 0.2, L_{EB}, L_B, V_{bc}, N_e, N_b, N_c, w_b, T) \cdot C_{bc\_Si}(L_E, \alpha_{eb}, V_{bc}, N_b, N_c, T)} \right)^{\frac{1}{2}}$$

(2.97)

and

$$f_{m\_pnp\_xg} := \left(\frac{f_{t\_pnp\_xg}(J_p, \alpha_{vg}, x_e, V_{bc}, N_e, N_b, N_c, w_b, T)}{8 \cdot \pi \cdot R_{Bn\_x}(L_E, \alpha_{rbi} := 0.2, L_{EB}, L_B, V_{bc}, N_e, N_b, N_c, x_e, x_{bo} := 0, x_{bw} := 0, w_b, T) \cdot C_{bc\_x}(L_E, \alpha_{eb}, V_{bc}, N_b, N_c, x_{bw} := 0, x_c := 0, T)} \right)^{\frac{1}{2}}$$

(2.98)

and

$$f_{m\_pnp\_Si} := \left(\frac{f_{t\_pnp\_Si}(J_p, V_{bc}, N_e, N_b, N_c, w_b, T)}{8 \cdot \pi \cdot R_{Bn\_Si}(L_E, \alpha_{rbi} := 0.2, L_{EB}, L_B, V_{bc}, N_e, N_b, N_c, w_b, T) \cdot C_{bc\_Si}(L_E, \alpha_{eb}, V_{bc}, N_b, N_c, T)} \right)^{\frac{1}{2}}$$

(2.99)

giving us figure 2.15, where apparently the left side of the graded npn HBT maximum is lateral transport limited due to base thinning and the increase of lateral base resistance and the right side is vertical transport limited, due to the accumulation of delays in the cutoff frequency.

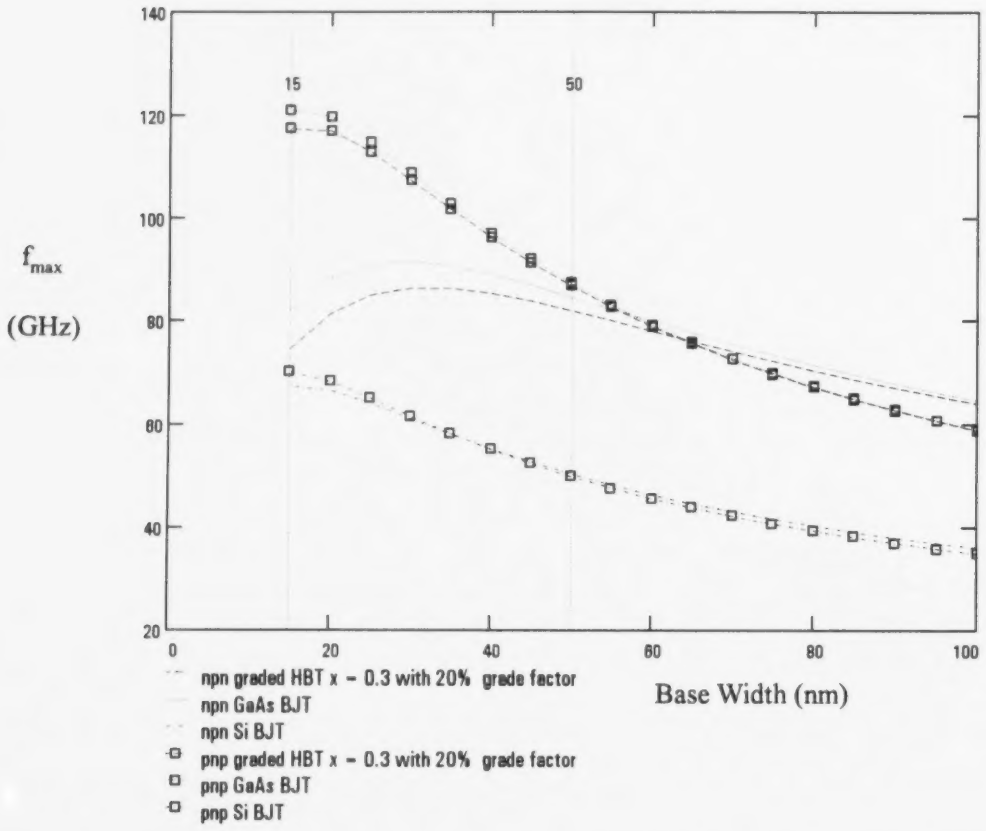

Figure 2.15: Theoretical f_{max} for npn and pnp devices with zero base field as a function of base width at $V_{bc} = 0$ and with equivalent parameters to figures 2.9 to 2.14

Clearly below 50 nm the cutoff frequency advantage of the npn device has been countered at low collector voltage by the mobility advantage of the graded pnp HBT base in the lateral dimension [58 to 62]. As base width is reduced the base transit time decreases improving the cutoff frequency and increasing base lateral resistance lessening the relative importance of cutoff frequency to the maximum frequency of oscillation such that a compromise situation arises, and optimization for particular operational

parameters is necessary. From the perspective of analog design it would be preferable to maintain the frequency advantages of the HBT architecture with if possible a lower turn on voltage combined with other optimizations such as improved current gain vs. collector current, reduced offset voltage and reduced sensitivity to process or material variations across or between substrate wafers. Some of these considerations will be addressed in the next section.

2.11 Section Summary

This review of some of the more critical factors affecting the work in the following sections has included some of the sources of recombination current in compound semiconductor devices, the bandgap narrowing approximation, and an explicit component model of the elements contributing to the relative frequency performance of an idealized set of npn and pnp bipolar devices. From the presence of significant 2kT current, due in part to surface recombination, it can be postulated that the overall device current gain characteristic will likely be lower at low collector current. This will gradually increase with current as the relative importance of the 2kT component diminishes with respect to kT recombination current components. Clearly it is desirable to reduce the magnitude of the 2kT current contribution by whatever means are available to rectify this situation. Bandgap narrowing is dopant species specific and as such other considerations such as diffusivity or epitaxial growth technique may determine which

dopant is to be used and hence what level of band gap narrowing is present in the emitter, base and collector. Generally the simulations here assume Si as an n-type dopant and Be as a p-type dopant. From the perspective of f_{max} optimization for compound semiconductor devices with relatively high mobility electrons it appears the pnp configuration is preferable as the relative effect of the higher mobility in the lateral base out weighs vertical mobility advantages at low collector voltage and relatively narrow collector base space charge region. Another factor to be considered at higher collector voltages is the scattering of electrons to higher energy minima possibly negating to some degree the relative advantage over holes.

Chapter 3

RESULTS AND DISCUSSION

This section presents the historical perspective and reasoning for the recent innovation of a modified form of bipolar device called a heterostructure emitter bipolar transistor (HEBT), followed by a detailed analysis of the HEBT architecture and its positioning with respect to the graded emitter HBT, which is the main contribution of this work. The analysis consists of the creation of a one dimensional model for the heterostructure emitter followed by the use of the model to compare HEBT performance characteristics to graded emitter HBT characteristics. The course of this analysis proceeds by analyzing the basic characteristics of an idealized isotype heterojunction in the emitter, followed by the relative frequency response characteristics and current gain of the overall device. The results from the analysis of frequency response are seen to imply guidelines for overall optimization of the heterostructure emitter, which are then formulated by further analysis into a set of equations which can be used for optimization and approximation of critical performance parameters.

From a historical perspective one of the more significant recent developments was the growth by MBE of a rectifying isotype heterojunction ramp in the late 1970's at the Bell Laboratories [63]. This new structure demonstrated the potential to, as indicated by Allyn, Gossard and Wiegmann [63] and early work from Anderson [47] and later from others [64 to 68], allow flexible programming of barrier structures "including low barriers for low voltage operation". Subsequently the investigation of compound semiconductor fabrication and material technology in general benefited from the

proliferation of FET and other devices in the early to mid 1980's [69 to 74]. Work on compound semiconductor abrupt heterotype heterojunction bipolar transistors in the 1980's encountered interesting problems, as indicated in previous sections, leading to the investigation of modifications and enhancing research efforts on compound semiconductor material properties [75] including more data on the relatively new $Al_xGa_{1-x}As$ material system. From previous considerations, clearly the point of intersection of equivalent densities of opposing ion types which determines the metallurgical junction position of an Si BJT is complicated in a $Al_xGa_{1-x}As$ HBT by the presence of the alloy heterojunction, which theoretically should be perfectly aligned with the heterotype homojunction to produce the heterotype heterojunction.

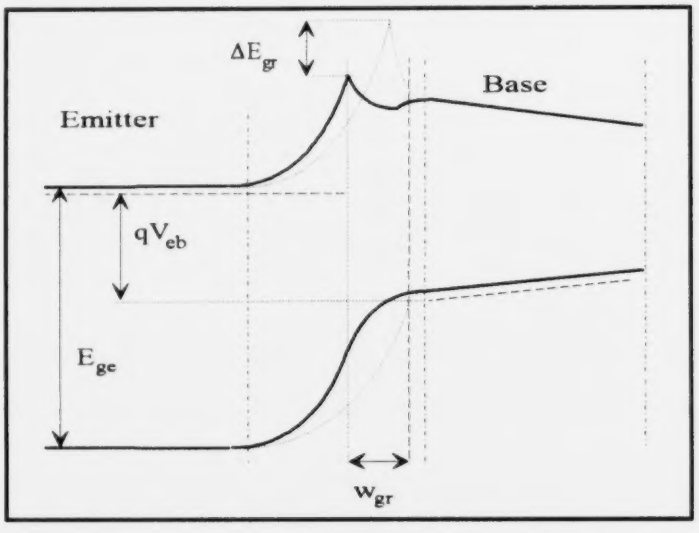

Figure 3.1: Illustrative band diagram showing movement of the conduction band peak back into the emitter scr and down in energy with the emitter alloy grade

Historically, it appears, the first major modification considered for the HBT emitter was the use of a graded $Al_xGa_{1-x}As$ layer, as indicated in figure 3.1, and in chapter one, to

reduce the height of the energy barrier and dissociate the alloy peak from the dopant metallurgical junction as indicated respectively in figure 3.1 by ΔE_{gr} and w_{gr}. It should be noted that the emitter grade also changes the valence band profile and creates an "energy pocket" near the interface which increases local carrier densities in the proportionate manner affiliated with 2kT current [76]. The results of this experimentation can be seen in figure 3.2 after [77], where the rather disconcerting spread of abrupt HBT current voltage characteristic across the wafer has been significantly reduced by the emitter grade. Clearly as well, from figure 3.2, the turn on voltage of the graded emitter design is reduced.

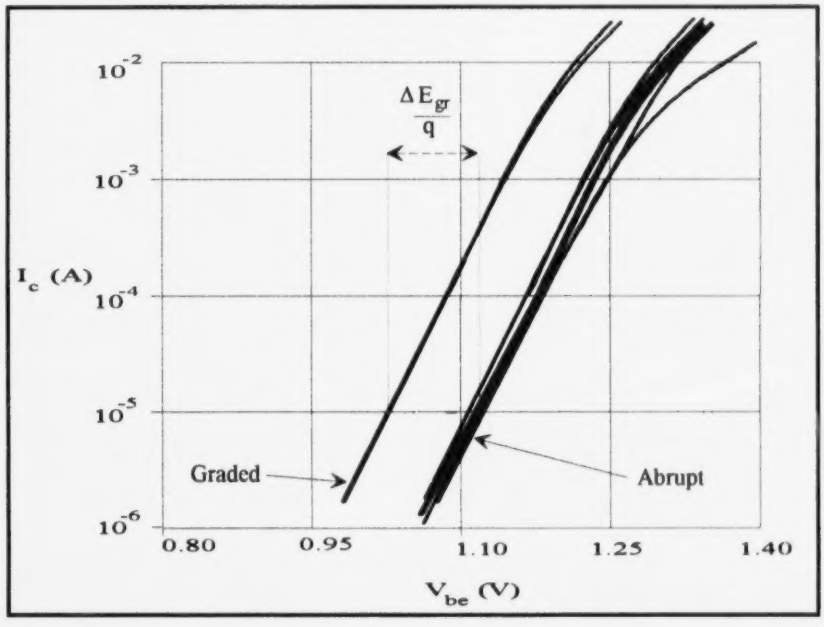

Figure 3.2: Illustrative plot of graded and abrupt HBT I_c vs. V_{be} for several test devices on two different wafers at several points across the wafer

The reduction in turn on voltage is a function of the emitter grade parameters, such that the

corner of the grade occurs back from the EB junction at a distance (w_{gr}) correlating to the location of the new conduction band peak as indicated in figure 3.1 by the thick solid conduction band line [78]. Further comparing figures 3.1 and 3.2, the onset of current characteristic variation for the graded devices is limited to, as indicated in figure 3.2, higher collector currents implying a similar variation phenomena to the abrupt devices of shifted sensitivity. This leads to the conclusion that if the sources of current characteristic variations are the same for both devices then the reduced magnitude and changed onset of the variation in the graded devices is likely due to the relative position of the emitter space charge region edge with respect to the height of the peak in the conduction band. Possible causes of the variation for the abrupt devices could include a localized energy barrier distortion surface due to defects/traps with net statistical variation of the average conduction band peak height over the surface of the emitter base interface or, assuming consistent alloy growth conditions, differential out diffusion of base dopant, possibly induced by lateral variations in base dopant concentration combined with local thermal history. Clearly the reduced sensitivity of the graded devices is due to some variational aspect(s) of the relative localized alignment of the emitter alloy/dopant and base dopant out diffusion profiles [79] [80] [81].

High frequency response is only attainable at high current density which makes a well matched current characteristic between devices in this regime highly desirable for analog design purposes. Clearly, high current density means a collapsed scr of a few tens of nanometers. Visible in the scanning ion mass spectrometry (SIMS) plot of the Beryllium (Be) base dopant of figure 3.3, after [82] are carry forward peaks of Be extending about

100 nm into the emitter past the base out diffusion profile resulting in a total of about 150 nm incursion of variational anomalies into the emitter.

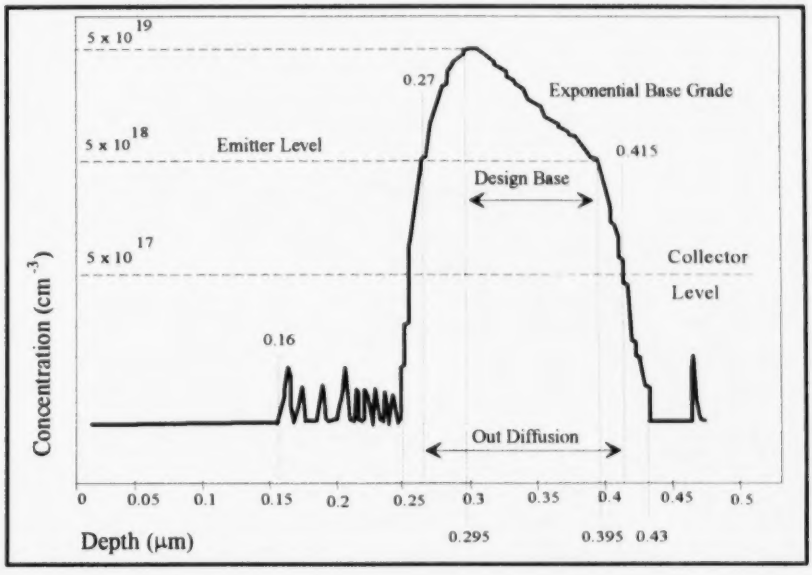

Figure 3.3: Scanning ion mass spectrometry plot of a Beryllium out diffusion profile for a dopant graded base

Clearly in order to minimize the impact of the alloy alignment with the base out diffusion intersection of the emitter out diffusion and other anomalies on the graded emitter HBT current voltage characteristics at high current density a relatively long alloy grade may be necessary with the compromise of putting the edge of the scr within the graded region at the current densities of interest. A current characteristic transition zone near the conduction band peak would be created and likely be affected more by lateral peak position rather than height introducing another possible source of variation. The onset of degradation of

current gain due to the reduction of the base majority carrier barrier profile would be a factor when operating in the alloy graded zone. Increased storage of charge in a larger energy pocket [78] may affect switching time, diffusion capacitance and increase the 2kT current component. Clearly maximum base dopant concentration is highly desirable from the performance perspective [83] which implies enhanced base dopant out diffusion profiles [84] of greater extent and potential variation into the emitter and across the wafer for a given dopant species likely causing current induced degradation [85] [86] [87].

3.1 The HEBT Design Philosophy

A potential solution to the variational compromises implicit in the graded HBT is to further dissociate the alloy to dopant alignment problems by providing a secondary interface further back in the emitter, outside of the scr at high current. Clearly in the context of bandgap engineering the isotype heterojunction is a potential candidate for this task and as such from these considerations we propose to investigate the heterostructure emitter bipolar transistor (HEBT), which uses the isotype heterojunction of Allyn, Gossard and Wiegmann [63] set back from the the emitter scr. This innovation essentially moves part of the minority carrier blocking capability of the heterotype heterojunction emitter base junction of the HBT back into the emitter quasi-neutral region leaving a heterotype homojunction as the primary interface to the base and is somewhat analogous to the well known minority carrier blocking polysilicon emitter employed for high performance Si BJTs. As far as one can discern, from the literature [88 to 92], this type of

emitter contact was first mentioned as a relatively unlikely design variation in connection with a 1986 theoretical analysis [93] of the npn GaAs homojunction transistor.

3.2 **The HEBT Model**

The HEBT structure has been fabricated recently [89] [90] [91] [92] and is briefly reviewed here before more extensive discussion in later sections. The energy band diagram in figure 3.4 indicates the most distinguishing feature of the minority carrier confinement strategy as the energy barrier in the form of an isotype heterojunction in the emitter.

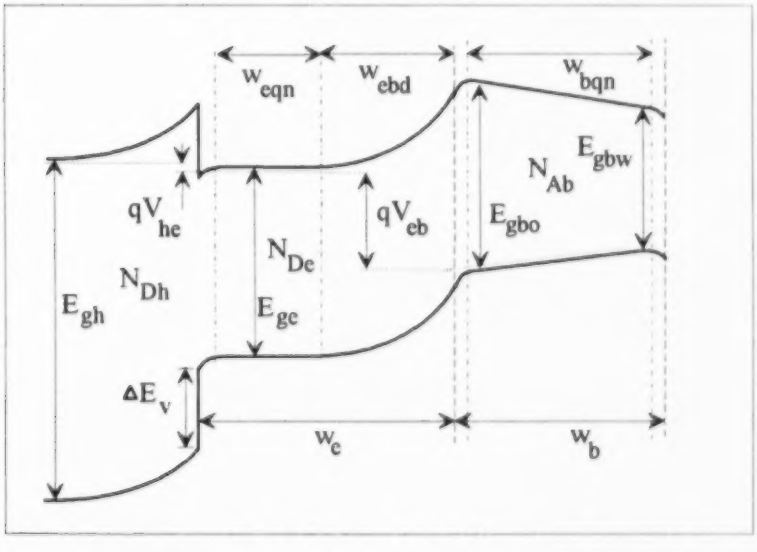

Figure 3.4: Schematic npn HEBT band diagram of the isotype heterojunction confinement emitter with an alloy graded base.

Briefly the hole, or in the case of a p-pnp device electron, path starts from the very high concentration of carriers in the base, some of which escape the energy barrier at the emitter base heterotype homojunction then diffuse (D_{pe}) and recombine (τ_{pe}) across the quasi neutral region (w_{eqn}) to the isotype heterojunction valence barrier, where again some escape by various means. An accumulation of electrons and relative depletion of holes occurs on the emitter side of the isotype heterojunction barrier corresponding to the downward bend of the conduction and valence bands. For initial modeling the isotype heterolayer is assumed to be flat rather than a ramp with differential doping on the heterolayer (N_h) and emitter (N_e) sides. As both isotype heterojunction voltage V_{he} and heterotype homojunction voltage V_{eb} increase, their respective space charge regions decrease in width creating a wider quasi-neutral region(w_{eqn}) along with a covariantly larger hole concentration, due to the reduction of the valence band energy barriers. As the isotype heterojunction valence band energy barrier confining the holes decreases the isotype heterojunction forward bias V_{he} increases, indicating that the current voltage characteristics of the isotype heterojunction combined with the heterotype homojunction are key characteristics of the HEBT, such that if a low isotype heterojunction voltage(V_{he}) is needed to supply majority carrier current the hole blocking confinement barrier remains effective at high current density. Hence the goals of this investigation are to construct a flexible theoretical model to determine the relative current gain, frequency response and other characteristics of the HEBT relative to an equivalent graded HBT, and to identify possible optimizations for improvement of HEBT performance. This is accomplished by formulating the structure of the devices into

'ıyered majority and minority carrier distributions using one dimensional drift diffusion equations combined with appropriate junction transport boundary conditions. From this we find the current density components and with further consideration of the junction voltages of the devices the junction capacitance, resistance and cutoff frequency are approximated as a function of current density. Factors, unique to the HEBT device architecture, affecting analog circuit performance are then considered for optimization on a priority basis. In order to simulate minority carrier escape at the emitter quasi neutral region to isotype heterojunction boundary, of figure 3.4, a dual component surface recombination velocity is assumed [94], such that the boundary condition at the edge of the emitter quasi neutral region is given by equating the rate of hole diffusion at the heterolayer edge of the emitter quasi-neutral region to the sum of the net thermal emission(S_{eh_n}) over the barrier plus the surface trap recombination(S_{eh_s}) in the vicinity of the barrier giving a total effective recombination velocity S_{eht} for the n-npn device

$$-D_{pe}\cdot\left(\frac{d}{dx}p_e(x)\right)_{w_{eqn}}=S_{eht}\cdot q\,p_e(w_{eqn}) \qquad (3.1)$$

and for the p-pnp HEBT, which to our knowledge has not been fabricated.

$$-D_{ne}\cdot\left(\frac{d}{dx}n_e(x)\right)_{w_{eqn}}=S_{eht}\cdot q\,n_e(w_{eqn}) \qquad (3.2)$$

The surface trap component of the net recombination velocity is assumed to be of the form

$$S_{eh\_sp}=\sigma_{ps\_GaAs}\cdot v_{th}\left(m_{dh}\left(x_e\right),T\right)\cdot N_{st} \tag{3.3}$$

and for the p-pnp device

$$S_{eh\_sn}=\sigma_{ns\_GaAs}\cdot v_{th}\left(m_{de}\left(x_e,T\right),T\right)\cdot N_{st} \tag{3.4}$$

The net assumed equivalent thermal emission surface recombination velocity(S_{eh_n}) is postulated as the sum of two components one corresponding to thermal emission of holes over the isotype heterojunction barrier(S_{eh}) and the other to back emission of holes from the heterolayer into the emitter(S_{he}). The current density components are the thermal emission hole current density from emitter to heterolayer(J_{p_eh}) and the back emission from the heterolayer into the emitter(J_{p_he}) for the n-npn HEBT

$$J_{p\_eh}=A_R\left(m_{dh}\left(x_h\right)\right)\cdot T^2\cdot\exp\left(-\frac{\Delta E_{vb\_eh}+E_{Fp\_ew}}{E_{th}(T)}\right) \tag{3.5}$$

and the p-pnp as

$$J_{n\_eh}=A_R\left(m_{de}\left(x_h,T\right)\right)\cdot T^2\cdot\exp\left(-\frac{\Delta E_{cb\_eh}+E_{Fn\_ew}}{E_{th}(T)}\right) \tag{3.6}$$

with back n-npn emission as

$$J_{p\_he} = A_R \left(m_{dh}(x_e) \right) \cdot T^2 \cdot \exp\left(\frac{E_{Fp\_ho}}{E_{th}(T)} \right) \qquad (3.7)$$

and p-pnp back emission as

$$J_{n\_he} = A_R \left(m_{de}(x_e, T) \right) \cdot T^2 \cdot \exp\left(\frac{E_{Fn\_ho}}{E_{th}(T)} \right) \qquad (3.8)$$

where the quasi-Fermi level for holes is approximated by

$$E_{Fp} = E_i - E_{th}(T) \cdot \ln\left(\frac{p}{n_i(x,T)} \right) \qquad (3.9)$$

and electrons similarly by

$$E_{Fn} = E_i - E_{th}(T) \cdot \ln\left(\frac{n}{n_i(x,T)} \right) \qquad (3.10)$$

and the intrinsic Fermi level for the $Al_xGa_{1-x}As$ bulk region by

$$E_i = \frac{1}{2} \cdot \left[\alpha_\Gamma(x,T) \cdot E_\Gamma(x,T) + \alpha_X(x,T) \cdot E_X(x,T) + \alpha_L(x,T) \cdot E_L(x,T) \ldots \right. \\ \left. + E_{th}(T) \cdot \ln\left(\frac{N_v(x,T)}{\alpha_\Gamma(x,T) \cdot N_\Gamma(x,T) + \alpha_X(x,T) \cdot N_X(x,T) + \alpha_L(x,T) \cdot N_L(x,T)} \right) \right] \qquad (3.11)$$

The surface trap hole recombination current density at the n-n heterolayer interface is approximated by

$$J_{p\_eh\_s} = q \cdot p_{ewqn} \cdot S_{eh\_sp}\left(N_{st\_eh}, x_e, T\right) \tag{3.12}$$

and at the p-p interface by

$$J_{n\_eh\_s} = q \cdot n_{ewqn} \cdot S_{eh\_sn}\left(N_{st\_eh}, x_e, T\right) \tag{3.13}$$

where p_{ewqn} and n_{ewqn} are the concentration of minority carriers at the edge of the heterolayer barrier as a function of overall operating conditions, such that the total current density at the n-n emitter to heterolayer barrier is given by combining the three components

$$J_{p\_eh\_t} = J_{p\_eh}\left(x_h, \Delta E_{vb\_eh}, E_{Fp\_ew}, T\right) - J_{p\_he}\left(x_e, E_{Fp\_ho}, T\right) + J_{p\_eh\_s}\left(p_{ew}, N_{st\_eh}, x_e, T\right) \tag{3.14}$$

and at the p-p barrier by

$$J_{n\_eh\_t} = J_{n\_eh}\left(x_h, \Delta E_{cb\_eh}, E_{Fn\_ew}, T\right) - J_{n\_he}\left(x_e, E_{Fn\_ho}, T\right) + J_{n\_eh\_s}\left(n_{ew}, N_{st\_eh}, x_e, T\right) \tag{3.15}$$

Clearly both the equivalent thermal emission and surface trap recombination minority carrier current densities in the emitter require a solution to the drift diffusion equation

in the quasi-neutral emitter which in turn cannot be solved without a solution to the majority carrier current densities as a function of the isotype heterojunction and heterotype homojunction forward bias requirements. Thus proceeding in sequence from the emitter quasi-neutral region, the hole lifetime in the n-n emitter is approximated by

$$\tau_{p\_x} = \frac{1}{\sigma_{p\_GaAs} \cdot v_{th}(m_{dh}(x), T) \cdot N_t} \tag{3.16}$$

which combined with the hole diffusion constant in emitter

$$D_{p\_x} = \mu_{p\_x}(N_i, x, T) \cdot V_{th}(T) \tag{3.17}$$

gives the hole diffusion length in the emitter as

$$L_{p\_x} = \sqrt{D_{p\_x}(N_{e'x_e}, T) \cdot \tau_{p\_x}(N_{e'x_e}, T)} \tag{3.18}$$

which combined with the roots for the solution to the n-n emitter DDE

$$r_{ne1} = \frac{1}{L_{p\_x}(N_{e'x_e}, T)} \tag{3.19}$$

and

$$r_{ne2} := r_{ne1}(N_e, x_e, T) \tag{3.20}$$

with for the p-p emitter using equations previously defined in section one

$$r_{pe1} := \frac{1}{L_{n\_x}(N_e, x_e, T)} \tag{3.21}$$

and

$$r_{pe2} := r_{pe1}(N_e, x_e, T) \tag{3.22}$$

and with n-n integration constants

$$c_{ne1} := \frac{-p_{xs\_e0}}{2 \cdot \left(\frac{D_{p\_x}(N_e, x_e, T)}{L_{p\_x}(N_e, x_e, T) \cdot S_{eht}} \cdot \cosh\left(\frac{w_{eqn}}{L_{p\_x}(N_e, x_e, T)} \right) + \sinh\left(\frac{w_{eqn}}{L_{p\_x}(N_e, x_e, T)} \right) \right)} \tag{3.23}$$

and

$$c_{ne2} := c_{ne1}(p_{xs\_e0}, w_{eqn}, N_e, S_{eht}, x_e, x_h, T) \tag{3.24}$$

with p-p integration constants

$$c_{pe1} := \frac{-n_{xs\_e0}}{2 \cdot \left(\frac{D_{n\_x}(N_e, x_e, T)}{L_{n\_x}(N_e, x_e, T) \cdot S_{eht}} \cdot \cosh\left(\frac{w_{eqn}}{L_{n\_x}(N_e, x_e, T)} \right) + \sinh\left(\frac{w_{eqn}}{L_{n\_x}(N_e, x_e, T)} \right) \right)} \tag{3.25}$$

and

$$c_{pe2} := c_{ne1}(n_{xs\_e0}, w_{eqn}, N_e, S_{eht}, x_e, x_h, T) \tag{3.26}$$

where p_{xs_e0} and n_{xs_e0} represent the excess minority carrier injected from the base into the emitter at the edge of the emitter scr. Proceeding with the analysis, using the approximate thermal equilibrium hole concentration in emitter as

$$p_0 := \frac{n_i(x,T)^2}{N_D} \tag{3.27}$$

gives the approximate parametrized solution for the hole distribution in the HEBT n-n emitter as a function of z as

$$\begin{aligned} p_e := {} & c_{ne1}(p_{xs\_e0}, w_{eqn}, N_e, S_{eht}, x_e, x_h, T) \cdot e^{r_{ne1}(N_e, x_e, T)\cdot z} \ldots \\ & + c_{ne2}(p_{xs\_e0}, w_{eqn}, N_e, S_{eht}, x_e, x_h, T) \cdot e^{r_{ne2}(N_e, x_e, T)\cdot z} \ldots \\ & + p_{xs\_e0} + p_0(N_e, x_e, T) \end{aligned} \tag{3.28}$$

with for the p-p case

$$\begin{aligned} n_e := {} & c_{pe1}(n_{xs\_e0}, w_{eqn}, N_e, S_{eht}, x_e, x_h, T) \cdot e^{r_{pe1}(N_e, x_e, T)\cdot z} \ldots \\ & + c_{pe2}(n_{xs\_e0}, w_{eqn}, N_e, S_{eht}, x_e, x_h, T) \cdot e^{r_{pe2}(N_e, x_e, T)\cdot z} \ldots \\ & + n_{xs\_e0} + n_0(N_e, x_e, T) \end{aligned} \tag{3.29}$$

The HEBT junction biases V_{he} and V_{eb} are assumed to be determined by the requirements of majority carrier current continuity combined with the junction transport characteristic for a given junction such that V_{he} for the isotype heterojunction is approximated after [47] by

$$V_{he} = V_{th}(T) \cdot \ln\left(\frac{J_{c\_he}}{J_{che0}} + 1\right) \tag{3.30}$$

where c is either n or p and using, for clarification, the notational substitution

$$V_{bi\_he} = V_{\beta}(x_h, x_e, N_h, N_e, T) \tag{3.31}$$

for the diffusion potential such that for the n-n case J_{nhe0} is approximated as

$$J_{nhe0} = \frac{q A_R (m_{de}(x_e, T))^2 \cdot T \cdot V_{bi\_he}(x_h, x_e, N_h, N_e, T)}{k} \cdot \exp\left(-\frac{V_{bi\_he}(x_h, x_e, N_h, N_e, T)}{V_{th}(T)}\right) \tag{3.32}$$

with for the p-p case

$$J_{phe0} = \frac{q A_R (m_{dh}(x_e))^2 \cdot T \cdot V_{bi\_he}(x_h, x_e, N_h, N_e, T)}{k} \cdot \exp\left(-\frac{V_{bi\_he}(x_h, x_e, N_h, N_e, T)}{V_{th}(T)}\right) \tag{3.33}$$

after [95] where the Richardson constant A_R assumes the lesser of the two effective masses after [20]. A plot of J_{nhe0} and J_{phe0} in figure 3.5 indicates in general a magnitude drop off with increasing alloy content and that the p-pnp J_{phe0} is greater by a factor of about seven over J_{nhe0} for a given alloy fraction essentially corresponding to their ratio of density of states effective mass. The effect of variation of J_{nhe0} and J_{phe0} on the minority carrier blocking barrier is the focus of the following analysis.

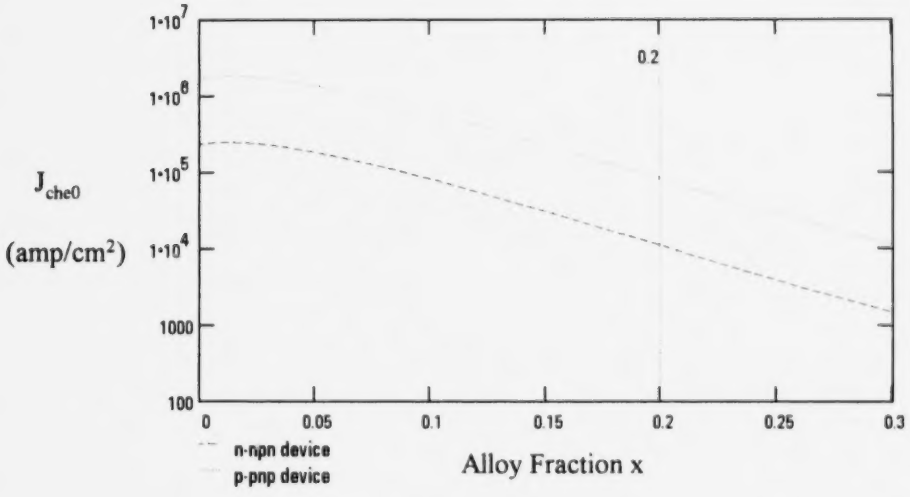

Figure 3.5: J_{che0} for n-n and p-p isotype heterojunctions with twice the heterolayer dopant level as emitter dopant level vs. heterolayer alloy fraction x with an emitter alloy fraction of zero, emitter dopant level of 1×10^{18} cm^{-3} and heterolayer dopant level of 2×10^{18} cm^{-3} at 300 K

Using representative values of J_{che0}, figure 3.6 indicates the forward bias V_{he} required to provide majority carrier current density J_{che}. It should be noted that as the forward bias V_{he} increases with J_{che} the minority carrier band energy barrier ΔE_{vb_he} or ΔE_{cb_he}

decreases, which indicates the p-p isotype heterojunction could under equivalent conditions provide better minority carrier blocking.

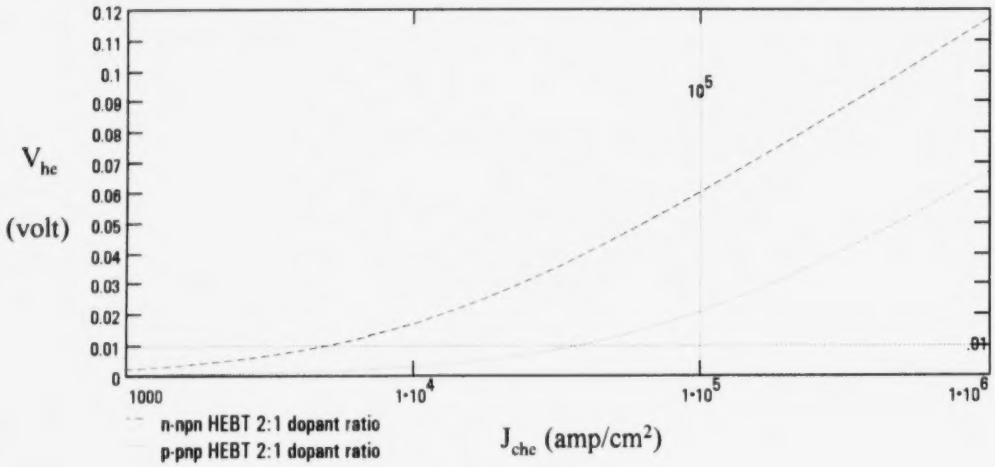

Figure 3.6: V_{he} for n-n and p-p isotype heterojunctions with a J_{che0} corresponding to figure 3.5 values locked at an x value of 0.2 vs. majority carrier current density at 300 K and with other parameters as in figure 3.5.

Using equations from chapter 1 the n-n heterolayer to emitter valence band gap offset change can be approximated as

$$\Delta E_v = \alpha_v \left[\begin{array}{l} \left(\alpha_\Gamma(x_h,T)\cdot E_\Gamma(x_h,T) + \alpha_X(x_h,T)\cdot E_X(x_h,T) + \alpha_L(x_h,T)\cdot E_L(x_h,T)\right) \cdots \\ + \cdot\left(\alpha_\Gamma(x_e,T)\cdot E_\Gamma(x_e,T) + \alpha_X(x_e,T)\cdot E_X(x_e,T) + \alpha_L(x_e,T)\cdot E_L(x_e,T)\right) \end{array} \right] \quad (3.34)$$

and summing components the total hole valence band barrier is approximated by

$$\Delta E_{vb\_eh} = \Delta E_v(x_h,x_e,T) + q\cdot V_{bi\_he}(x_h,x_e,N_h,N_e,T) + \cdot q\cdot V_{he}(J_{nhe0}(x_h,x_e,N_h,N_e,T),J_{nhe},T) \quad (3.35)$$

with for the p-p case

$$\Delta E_c = \alpha_c \left[\begin{array}{l} \left(\alpha_\Gamma(x_h, T) \cdot E_\Gamma(x_h, T) + \alpha_X(x_h, T) \cdot E_X(x_h, T) + \alpha_L(x_h, T) \cdot E_L(x_h, T) \right) \ldots \\ + \left(\alpha_\Gamma(x_e, T) \cdot E_\Gamma(x_e, T) + \alpha_X(x_e, T) \cdot E_X(x_e, T) + \alpha_L(x_e, T) \cdot E_L(x_e, T) \right) \end{array} \right] \quad (3.36)$$

and summing components the total electron conduction band barrier is approximated by

$$\Delta E_{cb\_eh} = \Delta E_c(x_h, x_e, T) + q \cdot V_{bi\_he}(x_h, x_e, N_h, N_e, T) - q \cdot V_{he}(J_{phe0}(x_h, x_e, N_h, N_e, T), J_{phe}, T) \quad (3.37)$$

which when plotted in figure 3.7 at a representative high forward majority carrier current density of 10^5 amp per cm^2 indicates as expected an increasing barrier height with heterolayer alloy fraction, and also that the p-pnp device has approximately a 0.1 eV higher minority carrier barrier with the parameters of figure 3.7.

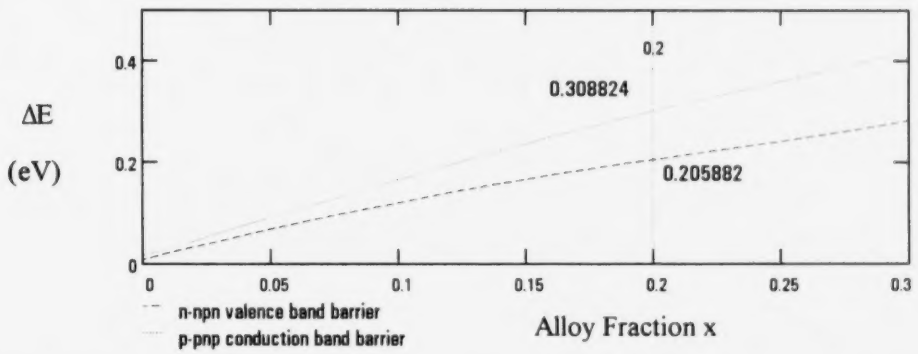

Figure 3.7: Valence and conduction band energy barrier height for n-npn and p-pnp HEBT isotype heterojunction steps with a J_{che} of 10^5 amp per cm^2 vs. heterolayer alloy content x with zero emitter alloy content and 2:1 heterolayer to emitter doping at 300 K.

Proceeding with overall device model, if we assume the ideal diode equation for the

emitter base heterotype homojunction in order to establish relative approximate excess minority carrier boundary conditions as a function of majority carrier current density. Then on either side where the excess hole concentration at the emitter edge of the scr for the n-npn device p_{xs_e0} is approximated allowing for bandgap narrowing at high Be base dopant levels by

$$p_{xs\_e0} = p_o(N_e, x_e, T) \cdot \left[\exp\left[\frac{V_{eb} - \frac{E_a(E_{a\_Be\_GaAs}, x_b)}{q}}{V_{th}(T)} \right] - 1 \right] \qquad (3.38)$$

with the equivalent expression for the p-pnp assumed silicon doped base device as

$$n_{xs\_e0} = n_o(N_e, x_e, T) \cdot \left[\exp\left[\frac{V_{eb} - \frac{E_a(E_{d\_Si\_GaAs}, x_b)}{q}}{V_{th}(T)} \right] - 1 \right] \qquad (3.39)$$

giving figure 3.8 where the n-npn device corresponds to the top dashed trace.

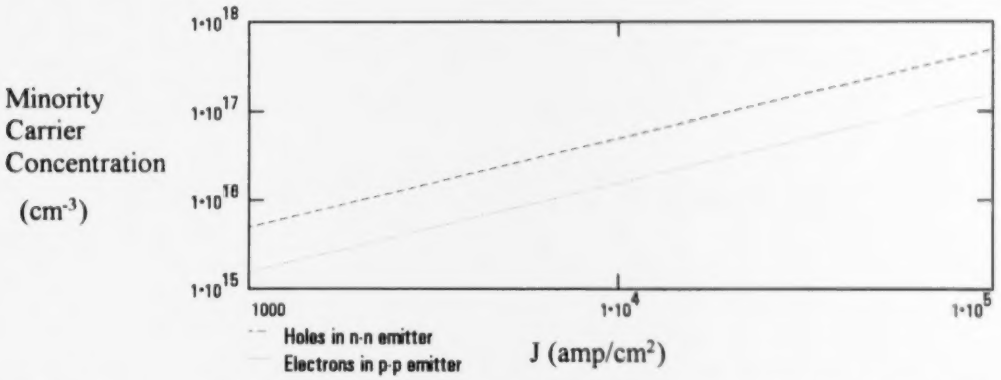

Figure 3.8: Assumed minority carrier concentration at emitter scr edge as a function of majority current density for n-npn and p-pnp devices at 300 K.

Further with the assumption that the majority current densities J_{chc} and J_{ceb} are essentially equal, assuming for this that the recombination current for the emitter bulk quasi-neutral region and surfaces are negligible, the minority carrier levels p_{ewqn} and n_{ewqn} at the edge of the heterolayer barrier can be determined using successive approximation for the components of S_{eht} however the distance $z = w_{eqn}$ from the edge of the emitter base scr to the edge of the heterolayer minority carrier scr is required as a function of majority carrier current density for both n-npn and p-pnp devices. Clearly the width of the emitter quasi-neutral region depends, in turn, on the position giving separation w_e of the two scr edges which again in turn are a function of their respective applied junction voltages and hence majority carrier current density. Starting with an approximation of the emitter heterolayer side

$$w_{eh} = w_d\left(V_{bi\_he}\left(x_h, x_e, N_h, N_e, T\right), V_{he}, \varepsilon_{s\_x}\left(x_e\right), N_e, N_h\right) \tag{3.40}$$

giving an emitter hole quasi-neutral region width of

$$w_{eqn} = w_e - \left(w_{eb\_he\_x}\left(V_{eb}, N_e, N_b, x_e, x_{bo}, T\right) + w_{eh}\left(V_{he}, N_h, N_e, x_h, x_e, T\right)\right) \tag{3.41}$$

where w_e is the metallurgical width of the emitter. Before constructing the overall models the limits on the emitter width should be considered. For a given set of parameters the existence of the assumed classical quasi-neutral region is dependent on the bias in as much as the space charge regions will merge at low bias if $w_e < w_{eh} + w_{eb}$. Thus for our

purposes here we will generally wish to choose $w_e > w_{eh} + w_{eb}$ at low bias or in consideration of the base out diffusion and carry forward, the anomalies will likely be contained in the quasi-neutral region if we assume 200 nm as in figure 3.9.

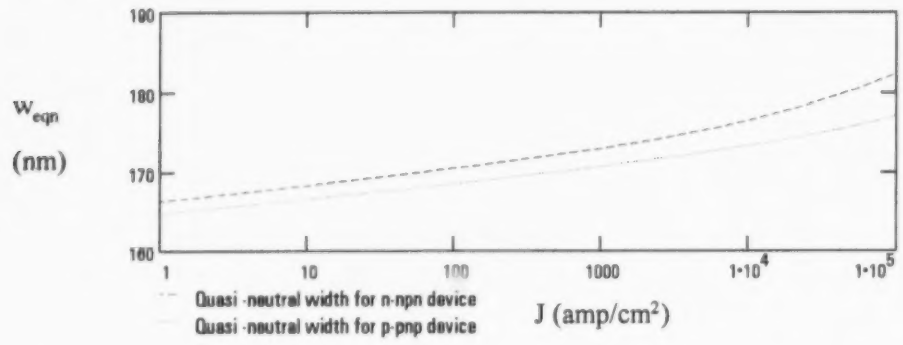

Figure 3.9: Estimated emitter quasi-neutral region width with w_e assumed as 200 nm as a function of majority current density for n-npn and p-pnp devices with N_e of 10^{18} cm^{-3} at 300 K.

Clearly from figure 3.9 the surface area of emitter sidewall in the quasi-neutral region is reduced at lower bias. Currently assuming surface recombination as the only escape mechanism at the heterolayer with a representative trap density of 1×10^{14} cm^{-2} gives a surface recombination velocity in the order of 10^6 cm/s. The distribution of minority carriers vs. z in the emitter is plotted in figure 3.10. From the results of figure 3.10 the relative magnitude of the outgoing thermal emission current over the barrier can be estimated assuming a 0.2:0 heterolayer to emitter alloy ratio combined with the preceding equations. The back emission is dependent on the excess electron population in the heterolayer at the edge of the heterolayer scr which is in turn dependent on the assumed carrier distribution.

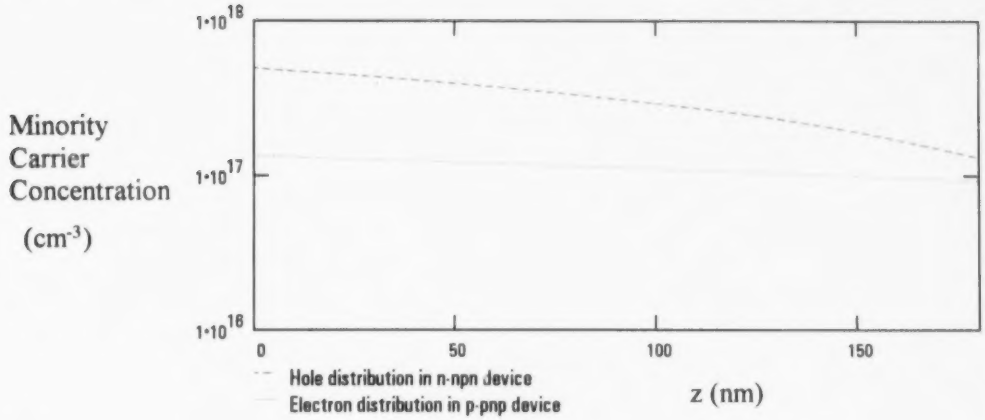

Figure 3.10: Estimated minority carrier distributions in the emitter quasi-neutral region as a function of displacement from the emitter scr edge (z = 0 nm) with w_e assumed as 200 nm and majority current assumed as 10^5 amp/cm^2 for n-npn and p-pnp devices with N_e of 10^{18} cm^{-3} at 300 K.

The emitter bulk recombination current is approximated by assuming for the n-npn case

$$J_{p\_re\_bulk} = \frac{q\, n_{e\_t}(p_{xs\_e0}, w_{eqn}, N_e, S_{eht}, x_e, x_h, T)}{\tau_{p\_x}(N_e, x_e, T)} \qquad (3.42)$$

with for the p-pnp case

$$J_{n\_re\_bulk} = \frac{q\, n_{e\_t}(n_{xs\_e0}, w_{eqn}, N_e, S_{eht}, x_e, x_h, T)}{\tau_{n\_x}(N_e, x_e, T)} \qquad (3.43)$$

From figure 3.11 it is apparent that the escaping thermal emission current density is reduced far below that of the assumed surface recombination current density with increase in heterolayer alloy thus preventing the escape of minority carriers further down the

emitter.

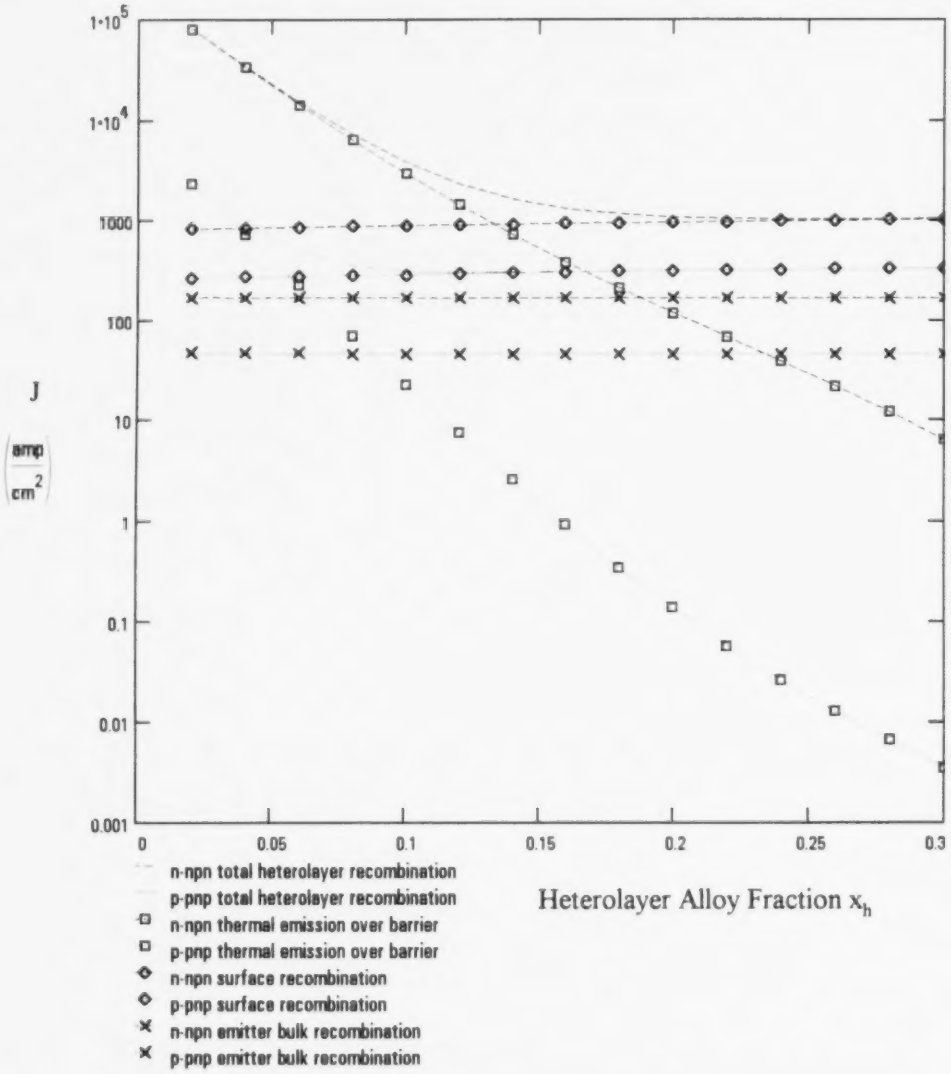

Figure 3.11: Estimated thermal emission current density at ($z = w_{eqn}$) as a function of x_h with w_e assumed as 200 nm and majority current assumed as 10^5 amp/cm^2 for n-npn and p-pnp devices with N_e of 10^{18} cm^{-3} and N_h of 2 x 10^{18} cm^{-3} at 300 K.

The ratio of majority to the sum of the minority current densities can be taken directly from figure 3.11, neglecting base bulk and surface recombination, giving figure 3.12.

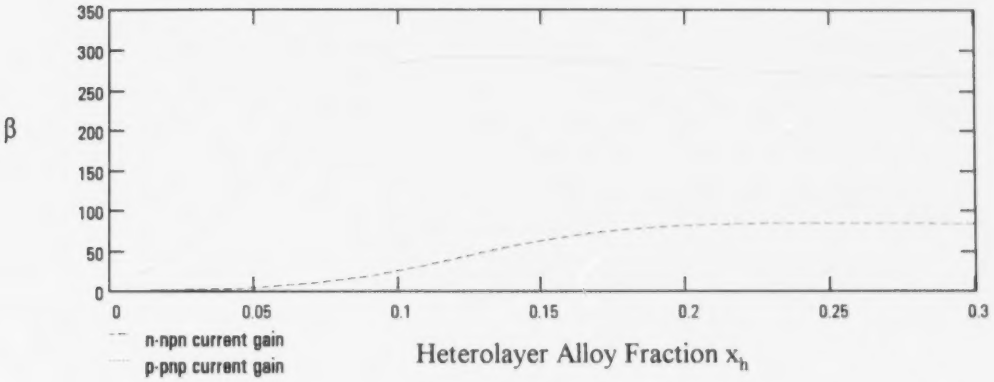

Figure 3.12: Estimated current gain as a function of x_h with w_e assumed as 200 nm and majority current assumed as 10^5 amp/cm^2 for n-npn and p-pnp devices with N_e of 10^{18} cm^{-3} and N_h of 2 x 10^{18} cm^{-3} at 300 K.

In summary, recalling the differences between the n-n and p-p isotype heterojunction emitter models as primarily indicated by the ratio of equation 3.32 to 3.33 combined with the ratio of equations 3.42 and 3.43 with the resultant difference in emitter quasi-neutral region width, the difference in current gain is clearly due to a combination of factors based on the fundamental difference in the thermal emission properties of holes vs. electrons.

Clearly at this point in the analysis the relationship between the heterolayer alloy fraction and the maximum frequency of oscillation is required in order to proceed with the overall comparison and formulation of device limitations.

3.3 **Heterostructure Emitter Small Signal Model**

The small signal equivalent circuit for the HEBT emitter, figure 3.13, follows from consideration of the HEBT emitter as two junctions in series, figure 3.4, each with parallel resistive and capacitive components.

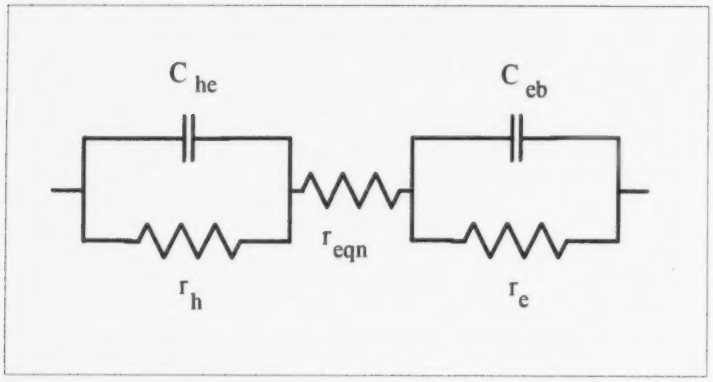

Figure 3.13: Small signal lumped element model of the heterostructure emitter

This model is incorporated into the intrinsic version of τ_{ec} of previous sections where only the depletion capacitance and other intrinsic parameters of τ_{ec} are considered for comparative purposes and the HEBT emitter charging time τ_e is given by

$$\tau_{e\_hebt} = r_h C_{he} + (r_h + r_e)(C_{eb} + C_{bc}) \qquad (3.44)$$

The effective resistances r_h and r_e are obtained by differentiating with respect to

current density J giving for the n-npn device

$$r_{h\_n} = \frac{V_{th}(T)}{J_{nhe0}(x_h, x_e, N_h, N_e, T) \cdot \left(\frac{J}{J_{nhe0}(x_h, x_e, N_h, N_e, T)} + 1 \right)} \tag{3.45}$$

and for the p-pnp device

$$r_{h\_p} = \frac{V_{th}(T)}{J_{phe0}(x_h, x_e, N_h, N_e, T) \cdot \left(\frac{J}{J_{phe0}(x_h, x_e, N_h, N_e, T)} + 1 \right)} \tag{3.46}$$

with for present purposes both n-npn and p-pnp r_e assumed for the nongraded base heterotype homojunctions as

$$r_e = \frac{V_{th}(T)}{J} \tag{3.47}$$

giving figure 3.14. From figure 3.14 it is apparent that the n-n isotype heterojunction has a higher low bias effective resistance than the p-p isotype heterojunction. It should be noted that at high current density the magnitudes of the isotype heterojunctions and heterotype homojunctions effective resistances become more comparable as heterolayer alloy fraction is increased as indicated in figure 3.15.

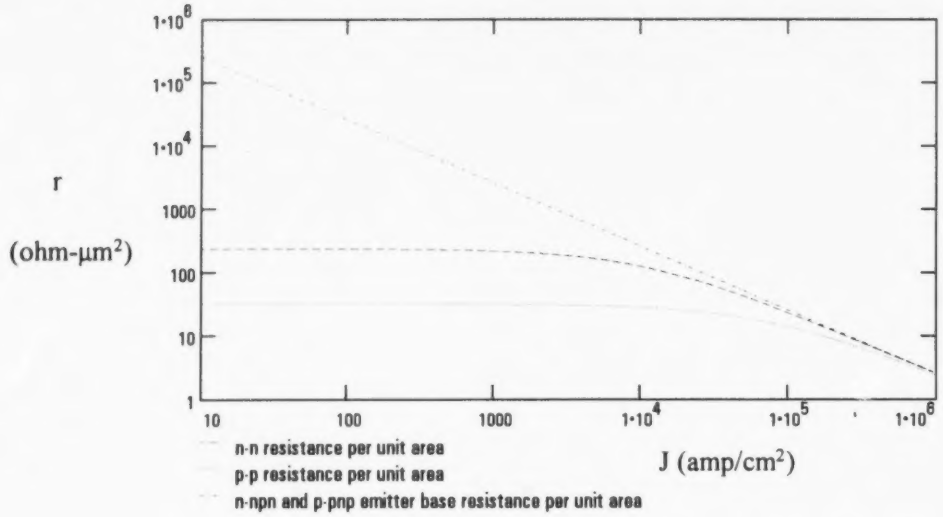

Figure 3.14: Estimated small signal effective resistance as a function of majority carrier current density for n-npn and p-pnp devices with heterolayer alloy $x_h = 0.2$ and $x_e = 0$ with N_e of 10^{18} cm^{-3} and N_h of 2 x 10^{18} cm^{-3} at 300 K.

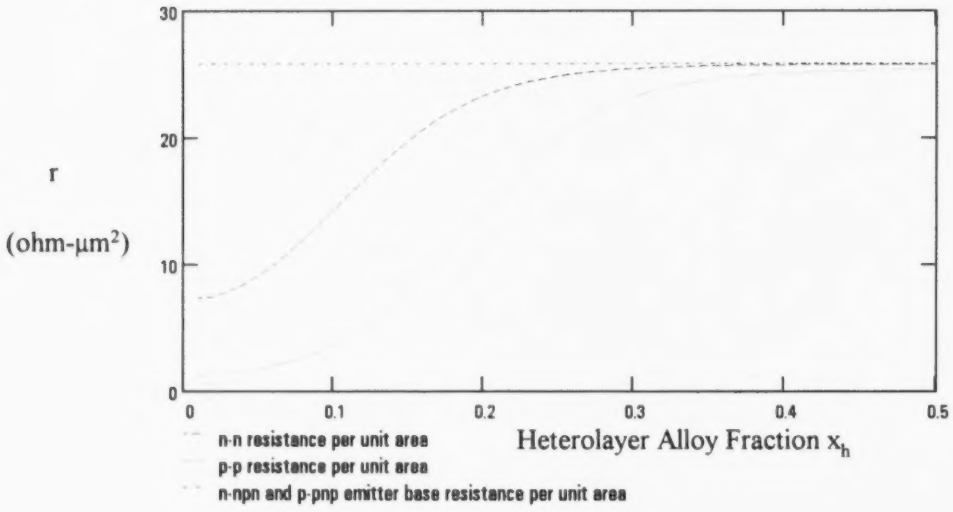

Figure 3.15: Estimated small signal effective resistance for n-npn and p-pnp devices as a function of heterolayer alloy fraction (x_h) with $J_{c\_he} = 10^5$ amp/cm^2 and $x_e = 0$ with N_e of 10^{18} cm^{-3} and N_h of 2 x 10^{18} cm^{-3} at 300 K.

The isotype heterojunction capacitance C_{he} of figure 3.13, is modeled after Cserveny [96] where the voltage drop across each scr is estimated by simultaneously solving

$$\frac{V_{\beta h}}{\left[V_{th}(T_r)\cdot\left(\exp\left(\frac{V_{\beta e}}{V_{th}(T_r)}\right)-1\right)-V_{\beta e}\right]}=\frac{\varepsilon_{s\_x}(x_e)\cdot N_e}{\varepsilon_{s\_x}(x_h)\cdot N_h} \qquad (3.48)$$

and

$$V_{\beta h}+V_{\beta e}=V_{\beta t}(V_{he},x_h,x_e,N_h,N_e,T) \qquad (3.49)$$

for $V_{\beta h}$ and $V_{\beta e}$, which are the voltage drops across the heterolayer scr and the emitter scr respectively for a given total potential $V_{\beta t}$ which is the V_β at thermal equilibrium minus V_{he} the off equilibrium applied bias. The situation is somewhat different from a

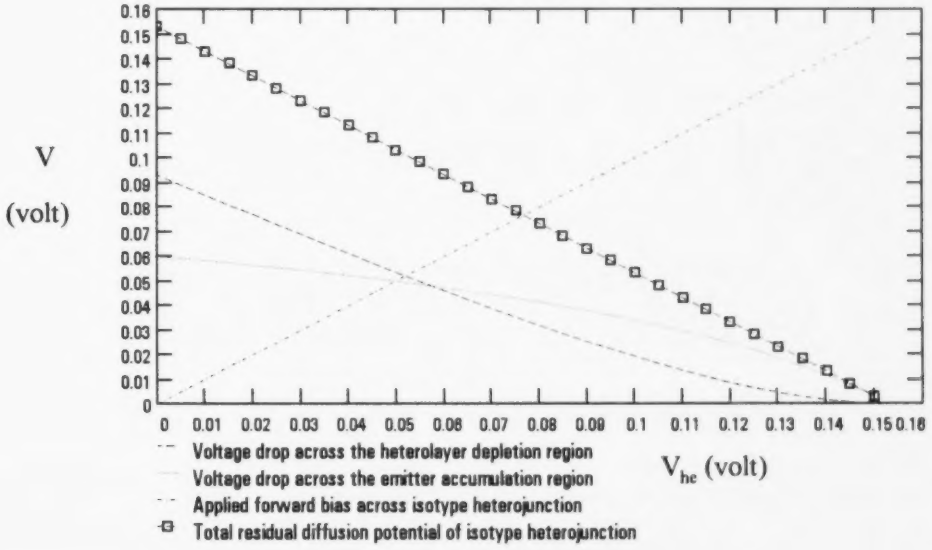

Figure 3.16: Estimated depletion ($V_{\beta h}$) and accumulation ($V_{\beta e}$) voltage drops for n-npn and p-pnp devices as a function of forward bias (V_{he}) with heterolayer alloy $x_h = 0.2$ and $x_e = 0$ with N_e of 10^{18} cm^{-3} and N_h of 2×10^{18} cm^{-3} at 300 K

heterotype junction in that the counterbalancing charge to the ions in the depletion region is composed of an accumulation of majority carriers rather than a depletion region of oppositely charged ions. The depletion and accumulation voltages of figure 3.16 are then used to model the junction capacitance by using the thermal voltage normalized potentials

$$\psi_t = \frac{V_{\beta t}(V_{he}, x_h, x_e, N_h, N_e, T)}{V_{th}(T)} \tag{3.50}$$

and

$$\psi_e = \frac{V_{\beta e}(V_{he}, x_h, x_e, N_h, N_e, T)}{V_{th}(T)} \tag{3.51}$$

giving, modified after [35]

$$\xi = \frac{1 - \left[\psi_t(V_{he}, x_h, x_e, N_h, N_e, T) - \psi_e(V_{he}, x_h, x_e, N_h, N_e, T)\right] \cdot \left(1 - \frac{\varepsilon_{s\_x}(x_e) \cdot N_e}{\varepsilon_{s\_x}(x_h) \cdot N_h}\right)^{-1}}{\left(\psi_t(V_{he}, x_h, x_e, N_h, N_e, T) - \psi_e(V_{he}, x_h, x_e, N_h, N_e, T) - 1\right)^{\frac{1}{2}}} \tag{3.52}$$

with

$$C_{he} = \left(\frac{1}{2} \cdot \frac{q^2}{k \cdot T} \cdot \varepsilon_{s\_x}(x_h) \cdot N_h\right)^{\frac{1}{2}} \cdot \xi(V_{he}, x_h, x_e, N_h, N_e, T) \tag{3.53}$$

giving figure 3.17 where the capacitance is plotted at high current density with heterolayer alloy fraction as the independent variable.

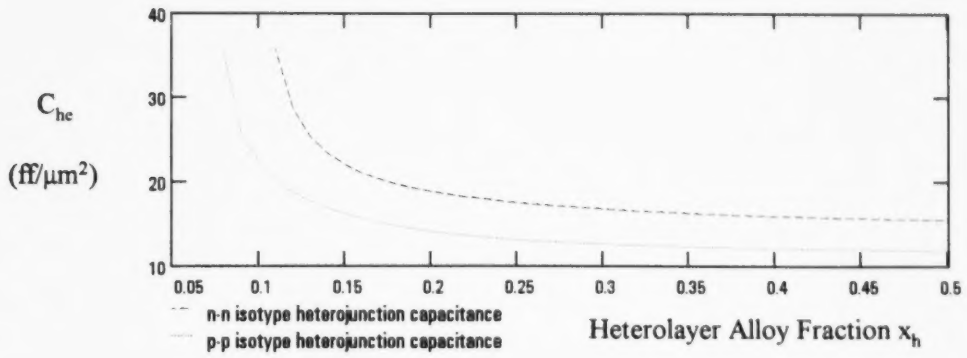

Figure 3.17: Estimated isotype heterojunction capacitance for n-npn and p-pnp devices as a function of heterolayer alloy fraction at a majority carrier current density (J_{c_he}) of 10^5 amp/cm^2 with heterolayer alloy $x_h = 0.2$ and $x_e = 0$ with N_e of 10^{18} cm^{-3} and N_h of 2×10^{18} cm^{-3} at 300 K.

Figure 3.17 and 3.18 are plotted using equation 3.30 combined with equations 3.32 and 3.33.

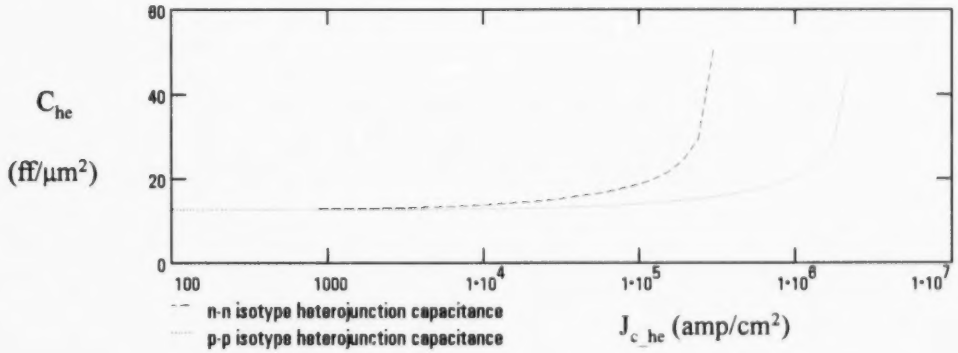

Figure 3.18: Estimated isotype heterojunction capacitance for n-npn and p-pnp devices as a function of majority carrier current density (J_{c_he}) with heterolayer alloy $x_h = 0.2$ and $x_e = 0$ with N_e of 10^{18} cm^{-3} and N_h of 2×10^{18} cm^{-3} at 300 K.

Now combining the resistive and capacitive components of equations 3.45, 3.46, 3.47 and 3.53 the comparative total HEBT emitter charging time for the n-npn and p-pnp devices

is plotted as frequency compared to the same emitter heterotype homojunction alone in figure 3.17 from equation 3.44 using

$$C_{eb\_ho\_x} = \frac{\varepsilon_{s\_x}(x_e)}{w_{ebt\_ho\_x}(V_{eb}, N_e, N_b, x_e, T)} \tag{3.54}$$

and assuming a base collector capacitance equivalent to equation 2.67 on a per unit area basis.

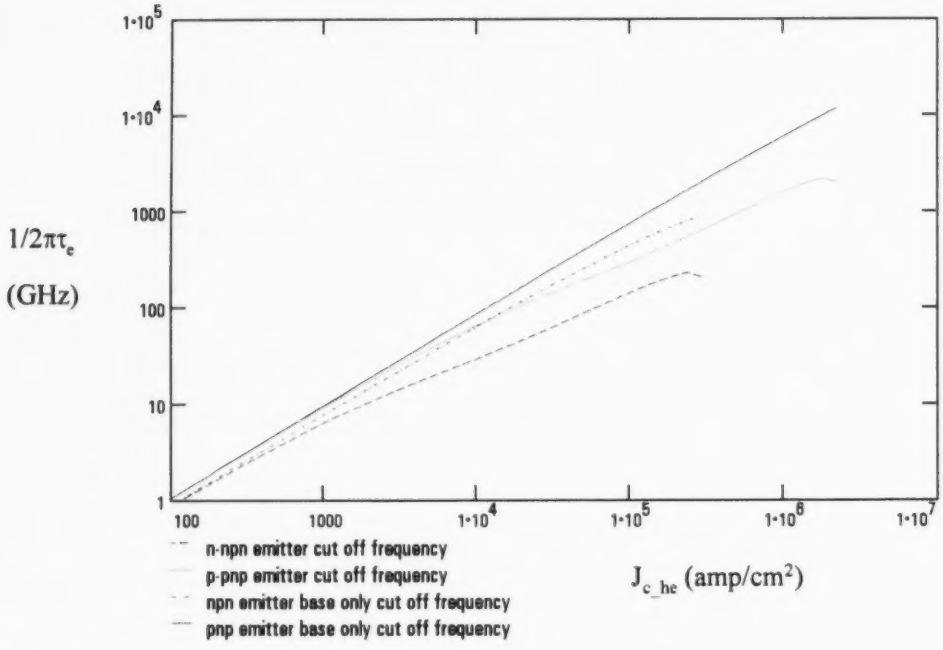

Figure 3.19: Estimated emitter cut off frequency for n-npn and p-pnp devices as a function of majority carrier current density (J_{c_he}) with $V_{bc} = 0$ volts heterolayer alloy $x_h = 0.2$ and $x_e = 0$ with N_e of 10^{18} cm^{-3} and N_h of 2×10^{18} cm^{-3} at 300 K.

Using $J_{c\_he} = 10^5$ amp/cm^2 of figure 3.17 as a reference current density figure 3.18 indicates the change of emitter charging time cut off frequency with heterolayer alloy fraction x_h.

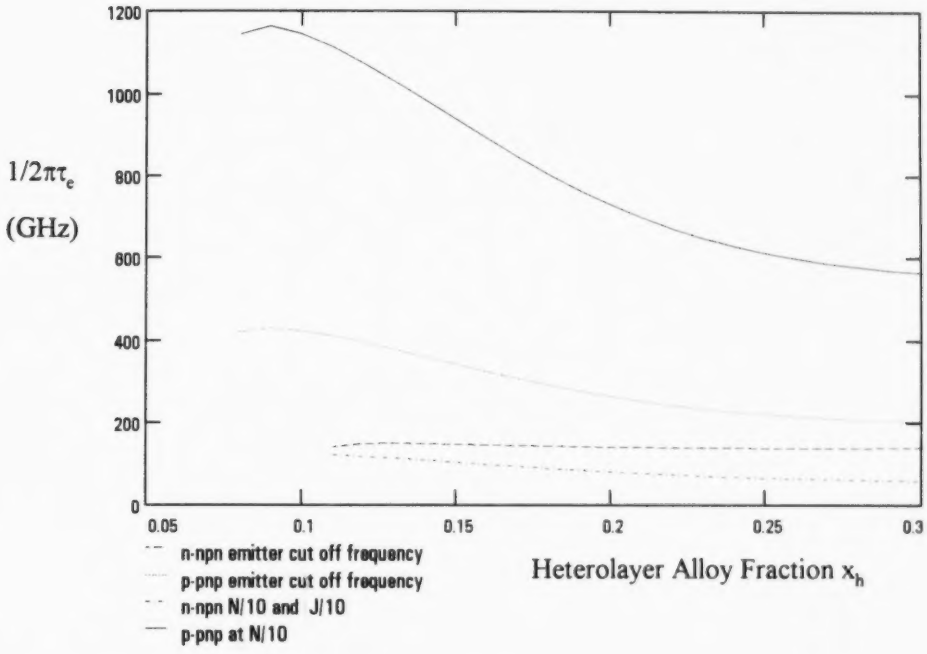

Figure 3.20: Estimated emitter cut off frequency for n-npn and p-pnp devices as a function of heterolayer alloy fraction (x_h) with $J_{c\_he} = 10^5$ amp/cm^2 and $V_{bc} = 0$ volts, $x_e = 0$ with N_e of 10^{18} cm^{-3} and N_h of 2×10^{18} cm^{-3} at 300 K.

Clearly from figure 3.20 both traces peak as a result of the resistance capacitance characteristic of the isotype heterojunction, indicating a possible optimization with consideration of the current gain characteristic of figure 3.12. The effect of heterolayer doping is plotted in figure 3.21 at a fixed value of heterolayer alloy mole fraction corresponding to the maximum frequency of figure 3.18.

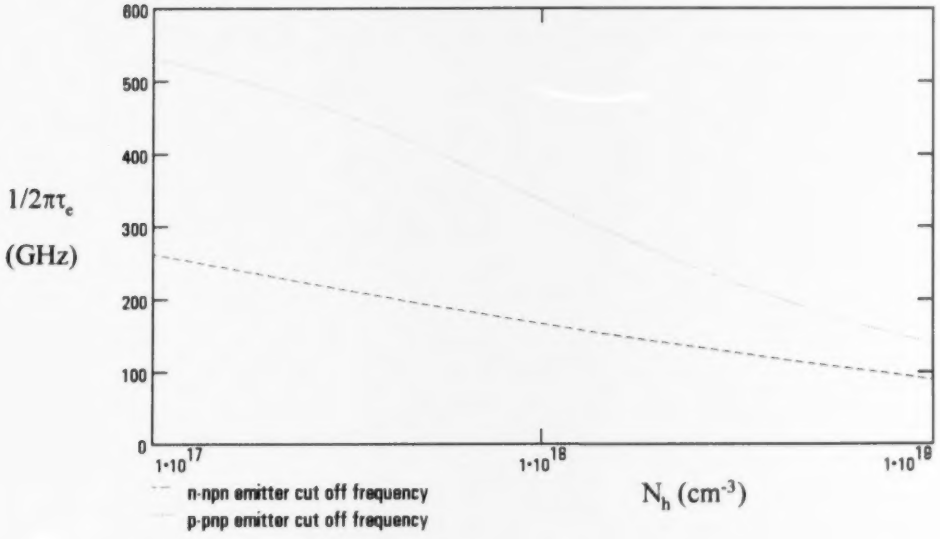

Figure 3.21: Estimated emitter cut off frequency for n-npn and p-pnp at $x_h = 0.2$ devices as a function of heterolayer doping (N_h) with $J_{c\_he} = 10^5$ amp/cm^2 and $V_{bc} = 0$ volts, $x_e = 0$ with N_e of 10^{18} cm^{-3} at 300 K.

Clearly from figures 3.19 through 3.21 the heterolayer alloy fraction and dopant ion concentration have a significant effect on the cut off frequency of the emitter and as such they can be used as optimization parameters.

The approach to optimization is from the perspective of maximizing the gain bandwidth product for the emitter in the form of

$$GBP_e = \frac{\beta_e}{2 \cdot \pi \cdot \tau_e} \qquad (3.54)$$

for a typical emitter doping level of 10^{18} cm^{-3} using the β characteristic and parameters of figure 3.12 for figure 3.22.

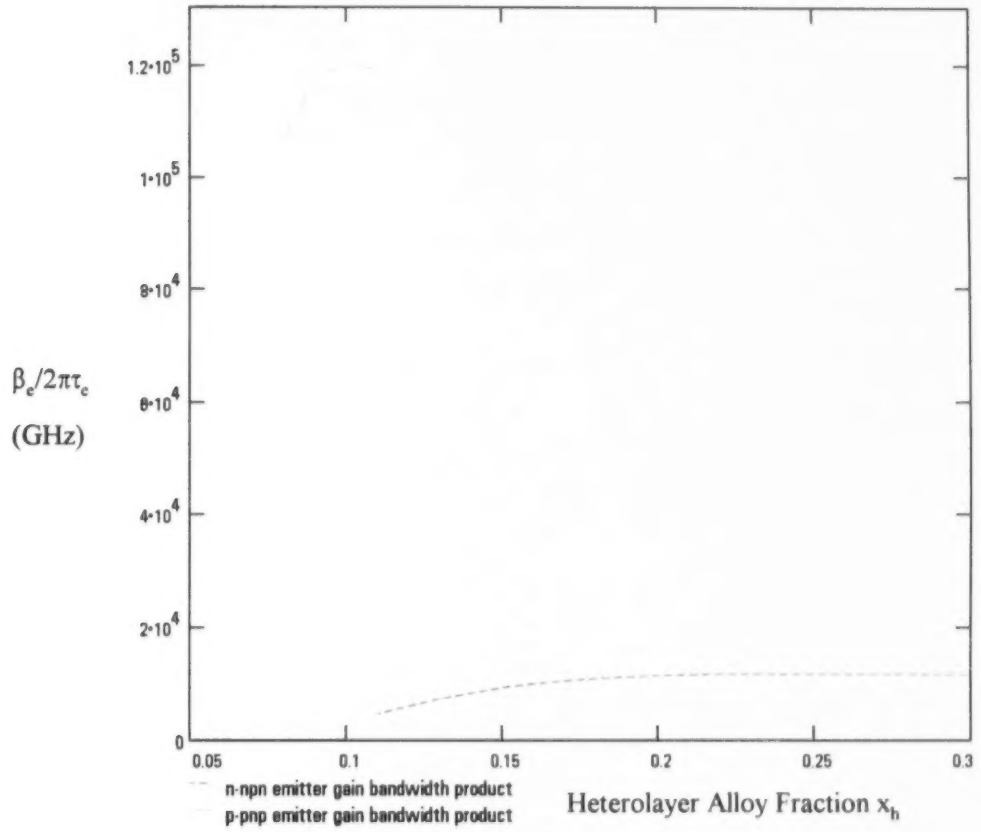

Figure 3.22: Estimated emitter gain bandwidth product for n-npn and p-pnp devices as a function of heterolayer alloy fraction (x_h) with $J_{c\_he} = 10^5$ amp/cm^2 and $V_{bc} = 0$ volts, $x_e = 0$ with N_e of 10^{18} cm^{-3} and N_h of 2×10^{18} cm^{-3} at 300 K.

From consideration of figure 3.22 the optimization of the p-pnp heterostructure emitter appears clearly a matter of selecting the maximum gain bandwidth product.

3.4 Comparison with HEBT Experimental Data

Experimental data extracted from [89] were used to parametrically simulate [97] a large area passivated device and predict the relative performance of an equivalent graded HBT. The experimentally derived ideality factor of 1.63 was assumed for both the HEBT and HBT with J_o being used to fit the current gain characteristic indicated in figure 3.23, where the solid trace includes the $J_{p\_eh\_s}$ surface recombination component and dashed trace does not. The maximum β of the passivated devices was determined from [89] as approximately 100 and is indicated in figure 3.23 by the dotted horizontal line.

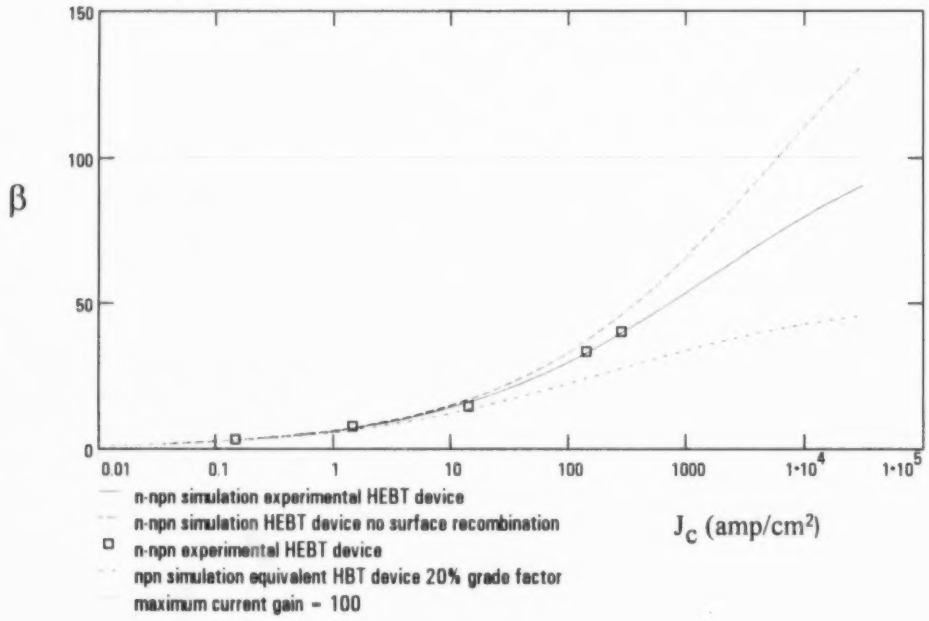

Figure 3.23: Estimated current gain for n-npn simulated and large area passivated experimental devices as a function of collector current density using $V_{bc} = 0$ volts, $x_e = 0$ with N_e of 5×10^{17} cm^{-3} at 300° K.

The HEBTs of figure 3.23 include a full simultaneous solution of the heterosurface recombination current densities. Figure 3.24 indicates the relative current density components for the devices of figure 3.23. The HEBT with no heterosurface recombination current, of figure 3.23 is missing $J_{p\_eh\_s}$ of equation 3.54 as indicated by the last trace in figure 3.24.

$$\beta = \frac{J_c}{J_{p\_eh} + J_{p\_eh\_s} + J_{re} + J_{rb} + J_{2kT}} \tag{3.55}$$

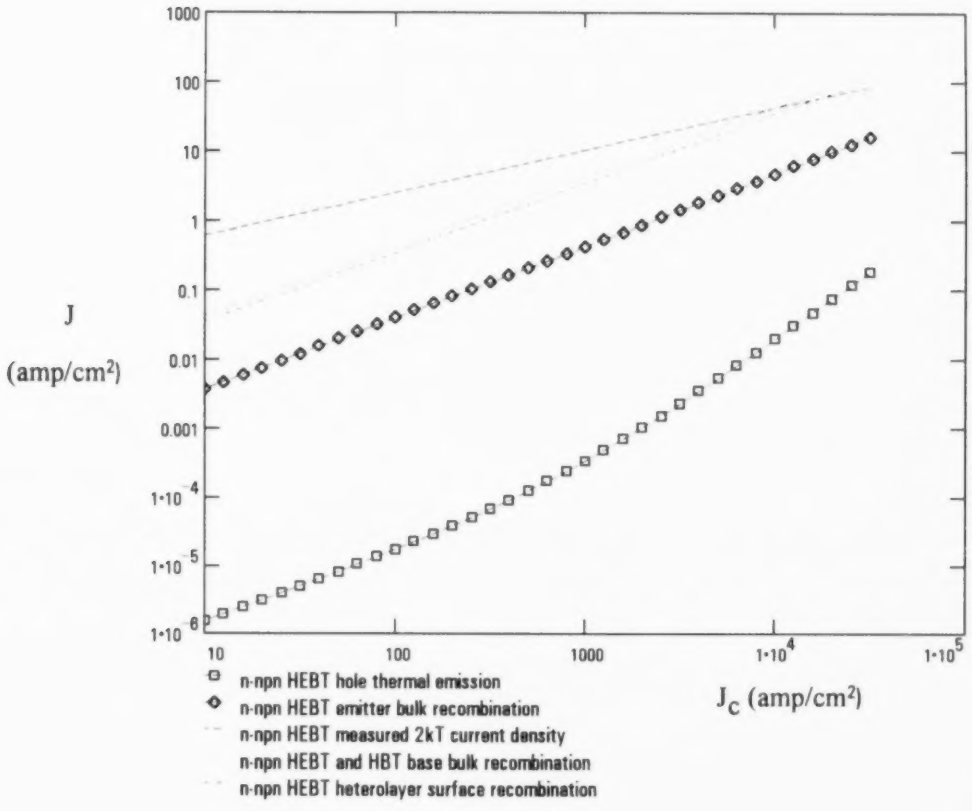

Figure 3.24: Estimated current density components for the simulated experimental n-npn HEBT of figure 3.23 as a function of collector current density.

It is assumed that the empirical fit of J_o from equation 3.56 to the experimental data, demonstrated by the close correspondence of the HEBT in figure 3.23, serves as a basis for comparative current density component decomposition.

$$J_{2kT}=J_o \cdot \exp\left(\frac{V_{eb}}{\eta \cdot V_{th}}\right) \qquad (3.56)$$

In the interests of equivalent comparison, the graded HBT device of figure 3.23 includes the same J_{2kT} current as the HEBT devices. Also a graded emitter HBT approach has been assumed with a grade factor of 20%. With these simulation parameters the maximum β of the simulated experimental HEBT, which matches the experimental data of [89] closely, is about double that of the simulated equivalent parameter graded emitter HBT.

Base bulk recombination current density is in the dominant position for the flat zero alloy HEBT simulated experimental device, while simulation of the same device with a graded base with critical built in quasi-electric field, indicates that heterosurface recombination current density has taken over that role. This implies that a graded base HEBT current gain characteristic may be more sensitive to variations in heterointerface surface conditions across the wafer.

The heterolayer thermal emission component of the simulated experimental HEBT is several orders of magnitude below the other major current densities with $x_h = 0.3$, even

when the isotype heterojunction forward bias increases at higher current levels.

3.5 HEBT vs. HBT Cut Off Frequency and Gain Bandwidth Comparison

Using the small signal equivalent circuit for the HEBT emitter of figure 3.13 in combination with the junction capacitances of figure 3.25 the relative cut off frequency

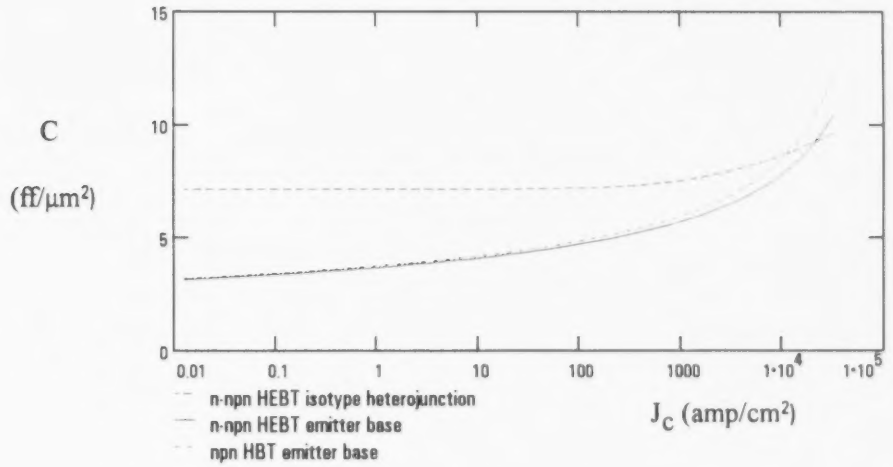

Figure 3.25: Estimated junction capacitances for the experimental HEBT and equivalent HBT devices of figures 3.22 and 3.23.

of the simulated experimental device and an equivalent graded HBT are indicated in figure 3.26. The following figure 3.27 indicates the product of the current gain of figure 3.23 and the cut off frequency of figure 3.26 for the n-npn HEBT experimental device and the equivalent graded emitter HBT. From figure 3.27 it is clear that the HEBT has a somewhat better gain bandwidth profile compared to the graded emitter HBT, at high current.

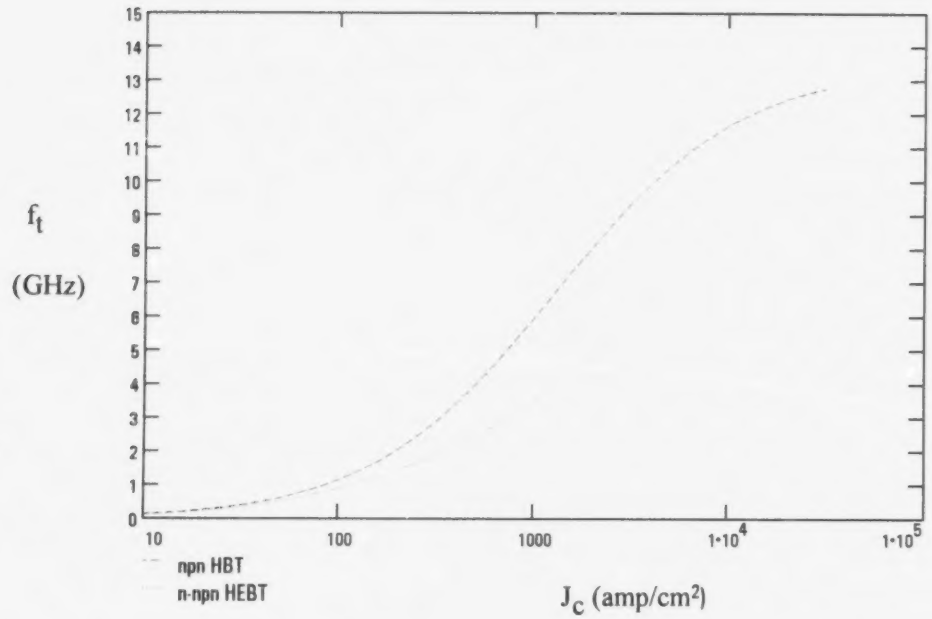

Figure 3.26: Estimated cut off frequency for equivalent HBT and simulated experimental HEBT devices as a function of collector current density with $V_{bc} = 0$ volts at 300° K.

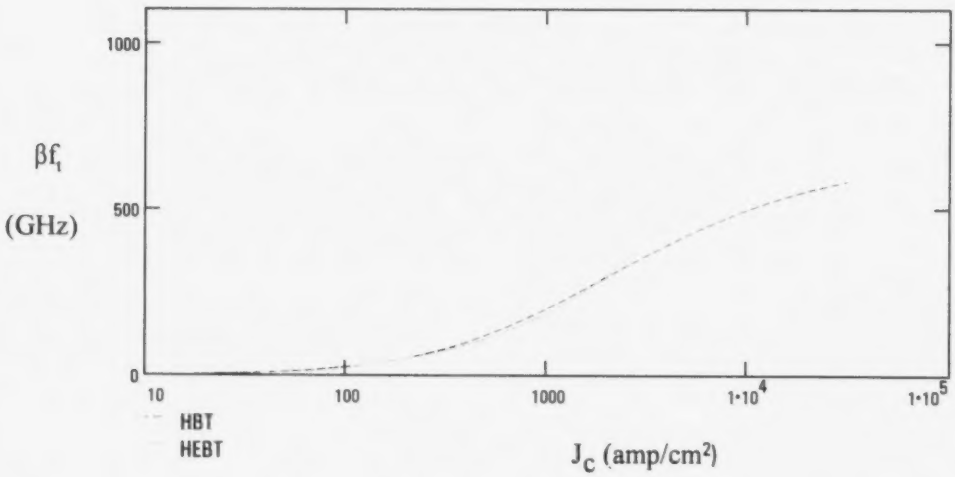

Figure 3.27: Estimated gain bandwidth products for experimental n-npn HEBT device and an equivalent HBT as a function of collector current density with $V_{bc} = 0$ volts at 300° K.

Chapter 4

CONCLUSIONS

In summary from consideration of the n-npn and p-pnp HEBT as an alternative to the graded emitter HBTs, several advances, heretofore seemingly unknown have been made. A one dimensional model of the heterostructure emitter has been created to approximate the quasi-static electrical performance of the n-npn and p-pnp HEBTs including a small signal lumped element model to calculate the resultant frequency performance.

The application of the model using compound semiconductor parameters derived from the literature has enabled new insight into the potential relative performance of the $Al_xGa_{1-x}As$ n-npn and p-pnp HEBT devices. Similarly, the application of the new n-npn HEBT model to an experimental device has yielded with parametric matching the first published prediction [97] of HEBT cut off frequency as a function of collector current density. Further, comparison to an equivalent parameter graded emitter HBT has yielded new data affecting the relative position of the HEBT vs. graded HBT architecture in terms of a significantly improved gain bandwidth product at high current density for an equivalent configuration.

Some of the more specific new insights gained from the use of the new HEBT model includes the superior performance of the p-pnp heterostructure emitter with respect to the n-npn device combined with cut off frequency optimization by consideration of the gain

bandwidth product of the heterostructure emitter as a function of alloy fraction and dopant concentration. Clearly this result combined with the relative f_{max} performance of the HBT pnp vs. npn configuration implies that the HEBT p-pnp device will exhibit the most favorable overall performance characteristics, for analog design, of the set of devices considered here.

4.1 **Future Research Directions**

From the perspective of future research on the relative performance of bipolar devices with the focus on compound semiconductor band gap engineered devices for analog design, it is likely that other new configurations are possible. Clearly a somewhat evolutionary approach is being facilitated by covariant developments in materials and fabrication technology, however, also clearly the control of atomic species location in the device and the structure of the surfaces are factors that could use improvement. An obvious extension of the current work would be to do more extensive characterization of the $Al_xGa_{1-x}As$ HEBT characteristics including high injection effects, collector-emitter offset voltage optimization, high temperature optimization, diffusion capacitance effects, reverse bias of the heterostructure emitter with negative differential resistance effects and other similar simulations. Clearly the HEBT simulation model could also be applied to other semiconductor systems. The HEBT model could be enhanced by, for example, considering other than rectangular heterolayer profiles or using higher dimensional or Monte Carlo simulation.

REFERENCES

[1] Bert K. Oyama and Brian P. Wong, "GaAs HBT's for Analog Circuits," Proc. IEEE , vol. 81, No. 12, pp. 1744-1760, 1993.

[2] P. M. Asbeck, Mau-Chung F. Chang, J. A. Higgins, N. H. Sheng, G. J. Sullivan and Keh Chung Wang, "GaAlAs/GaAs Heterojunction Bipolar Transistors, Issues and Prospects for Application," IEEE Trans ED, Vol. 36, pp. 2032-2041, 1989.

[3] P. M. Asbeck, Mau-Chung F. Chang, Keh Chung Wang, Gerald. J. Sullivan and Derek T. Chung, "GaAs-Based Heterojunction Bipolar Transistors for Very High Performance Circuits," Proc. IEEE , vol. 81, No. 12, pp. 1709-1726, 1993.

[4] R. L. Van Tuyl, V. Kumar, D. C. D'Avanzo, T. W. Taylor,V.E. Peterson, D. P. Hornbuckle, R. A. Fisher, D. B. Estreich, "A Manufacturing Process for Analog and Digital Gallium Arsenide Integrated Circuits," IEEE Trans. MTT, MTT-30, pp. 935-941, 1982.

[5] T. Andrade, "Manufacturing Technology for GaAs Monolithic Microwave Integrated Circuits," Solid State Technology, (1985).

[6] Klaus Fricke, Hans L. Hartnagel, Woo-Yong Lee and Joachim Würfl, "AlGaAs/GaAs HBT for High-Temperature Applications," IEEE Trans ED Vol. 39, No. 9, 1992.

[7] Shiyuan Yang, Toru Mizunami and Keiji Takagi, "Low Frequency Noise in GaAs," Jpn. J. Appl. Phys., Vol. 29, No. 7, 1990.

[8] S. M. Sze, *Physics of Semiconductor Devices*, 2nd Edn, Wiley-Interscience, New York p. 343 (1981).

[9] Eitan Michael Azoff, "Energy Transport Numerical Simulation of Graded AlGaAs/GaAs Heterojunction Bipolar Transistors," IEEE Trans ED Vol. 36, No. 4, 1989.

[10] Ch. S. Harder, B. J. Van Zeghbroeck, M. P. Kesler, H. P. Meier, P. Vettiger, D. J. Webb, P. Wolf, "High-speed GaAs/AlGaAs optoelectronic devices for computer applications," IBM J. RES. DEVELOP., Vol. 34, No. 4, 1990.

[11] Nobuyuki Hayama, Mohammad Madihian, Aikihiko Okamoto, Hideo Toyoshima and Kazuhiko Honjo, "Fully Self Aligned AlGaAs/GaAs Heterojunction Bipolar Transistors for High-Speed Integrated Circuits Application," IEEE Trans ED, Vol. 35, pp. 1771-1776, 1988.

[12] Young-Kai Chen, Richard N. Nottenburg, Morton B. Panish, R. A. Hamm and D. A. Humphrey, "Subpicosecond InP/InGaAs Heterostructure Bipolar Transistors," IEEE Electron Device Lett, Vol. 10, 1989.

[13] J. L. Zilko, L. J. P. Ketelsen, Y. Twu, D. P. Wilt, S. G. Napholtz, J. P. Blaha, K. E. Strege, V. G. Riggs, D. L. Van Haren, S. Y. Leung, P. M. Nitzsche, J. A. Long, C. B. Roxlo, G. Przyblek, J. Lopata, M. W., M. W. Focht and L. A. Koszi, "Growth and Characterization of High Yield, Reliable, High-Power, High-Speed, InP/InGaAsP Capped Mesa Buried Heteostructure Distributed Feedback (CMBH-DFB) Lasers", IEEE Journal of Quantum Electronics, Vol. 25, No. 10, 1989.

[14] W. Shockley, U.S. Patent No. 2,569,347 issued 1951

[15] H. Kroemer, "Theory of a wide gap emitter for transistors," Proc. IRE 45, pp.1535-1537, 1957.

[16] T. Hirose, A. Ryoji and M. Inada, "A Small Collector-Up AlGaAs/GaAs Heterojunction Bipolar Transistor Fabricated Using H^+ Implantation," Jpn. J. Appl. Phys., Vol. 30, No. 10A, 1991.

[17] Ralph E. Williams, "*Gallium Arsenide Processing Techniques*," Artech House, 1984.

[18] V. I. Rideout, "A Review Of The Theory And Technology For Ohmic Contacts To Group III-V Compound Semiconductors," Solid-St. Electron. Vol. 18, pp. 541-550, 1975.

[19] Anatoly A. Grinberg, Michael S. Shur, Russel J. Fischer and Hadis Morkoc, "An Investigation of the Effect of Graded Layers and Tunneling on the Performance of AlGaAs/GaAs Heterojunction Bipolar Transistors," IEEE ED Vol. 31, No. 12, 1984.

[20] A. A. Grinberg, "Thermionic emission in heterosystems with different effective electronic masses," Phys. Rev. B. 33, 7256 1986.

[21] S. M. Sze, *Physics of Semiconductor Devices*, 2nd Edn, Wiley-Interscience, New York, pp. 182-183 (1981).

[22] H. Kroemer, "Heterostructure Bipolar Transistors and Integrated Circuits," Proc. IEEE Vol. 70, No. 1, 1982.

[23] Marc H. Brodsky and A.R. Peaker, *Properties of Gallium Arsenide*, 2nd Edn, INSPEC, London and New York 1990.

[24] Cheng T. Wang, "*Introduction to Semiconductor Technology, GaAs and Related Compounds*," John Wiley & Sons, 1990.

[25] S. Dindo, "*GaAs Material Investigation for Integrated Circuits Fabrication*," M.A.Sc. Thesis, University of British Columbia, (1985).

[26] Sandip Tiwari and David J. Frank, "Analysis of the Operation of GaAlAs/GaAs HBT's," IEEE Trans ED, Vol. 36, No. 10, 1989.

[27] S. C. M. Ho and D. L. Pulfrey, "The Effect of Base Grading on the Gain and High Frequency Performance of AlGaAs/GaAs Heterojunction Bipolar Transistors," IEEE Trans ED, Vol. 36, No. 10, pp. 2173-2181, 1989.

[28] J. S. Blakemore, "Semiconducting and other major properties of gallium arsenide", J. Appl. Phys. **53**, R123 (1982).

[29] Sadao Adachi, "GaAs, AlAs, and $Al_xGa_{1-x}As$: Material parameters for use in research and device applications," J. Appl. Phys. **58**, R1 (1985).

[30] H. S. Bennett and J. R. Lowney, "Physics for Numerical Simulation of Silicon and Gallium Arsenide Transistors," Solid-St. Electron. Vol. 33, No. 6, pp. 675-691, 1990.

[31] S. M. Sze, *Physics of Semiconductor Devices*, 2nd Edn, Wiley-Interscience, New York, p. 18 (1981).

[32] Esther M. Conwell, *High Field Transport in Semiconductors*, Academic Press, New York, (1967).

[33] J. J. Liu and J. S. Yuan, "Surface Recombination Current of AlGaAs/GaAs Heterojunction Bipolar Transistors," Solid-St. Electron. Vol. 35, No. 6, pp. 805-813, 1992.

[34] S. Tiwari, S. L. Wright and D. J. Frank, "Compound semiconductor heterostructure bipolar transistors", IBM J. RES. DEVELOP. **34,** 550 (1990).

[35] C. H. Henry, R. A. Logan, and F. R. Merrit, " The effect of surface recombination on current in AlGaAs heterojunctions," J. Appl. Phys., Vol. 49, No. 6, pp. 3530-3542, 1978.

[36] William C. Rutherford, "*Gallium Arsenide Integrated Circuit Modeling, Layout and Fabrication*," M.A.Sc. Thesis, U.B.C., 1987.

[37] Kouhei Morizuka, Masayuki Asaka, Norio Iizuka, Kunio Tsuda and Masao Obara, "AlGaAs/GaAs HBT's Fabricated by a Self Alignment Technology Using Polyimide for Electrode Separation," IEEE Electron Device Lett., Vol. 9, No.11, 1988.

[38] Won-Seong Lee, Daisuke Ueda, Tony Ma, Yi-Ching Pao and James S. Harris, Jr., "Effect of Emitter-Base Spacing on the Current Gain of AlGaAs/GaAs Heterojunction Bipolar Transistors", IEEE Electron Device Lett. Vol. 10, No. 5, pp. 200-202, 1989.

[39] W. Liu and J. S. Harris, "Parasitic Conduction Current In Passivation Ledge Of GaAlAs/GaAs Heterojunction Bipolar Transistors," Solid-St. Electron. Vol. 35, No. 7, pp. 891-895, 1992.

[40] Paul E. Dodd, Theresa B. Stellwag, Michael R. Melloch and Mark S. Lundstrom, "Surface and Perimeter Recombination in GaAs Diodes: An Experimental and Theoretical Investigation," IEEE Trans ED, Vol. 38, No. 6, pp. 1253-1261, 1991.

[41] Sandip Tiwari, D. J. Frank and Steven L. Wright, "Surface recombination in GaAlAs/GaAs heterostructure bipolar transistors", J. Appl. Phys., Vol. 64, No. 10, pp. 5009-5012, 1988.

[42] M. S. Lundstrom, M. E. Klausmeier-Brown, M. R. Melloch, R. K. Ahrenkiel and B. M. Keyes, "Device-Related Material Properties of Heavily Doped Gallium Arsenide," Solid-St. Electron. Vol. 33, No. 3, pp. 693-704, 1990.

[43] H. H. Berger, "Models For Contacts To Planar Devices," Solid-St. Electron. Vol. 15, pp. 145-158, 1972.

[44] H. R. Chen, C. Y. Chang, K. L. Tsai, J. S. Tsang and C. P. Lee, "Novel AlGaAs/GaAs Heterostructure Bipolar Transistors Fabricated By Two-Stage Molecular Beam Epitaxy" Solid-St. Electron. Vol. 36, No. 4, pp. 485-487, 1993.

[45] Robert M. Fox and Sang-Gug Lee, "Scalable Small-Signal Model for BJT Self-Heating", IEEE Electron Device Lett. Vol. 12, No. 12, pp. 649-651, 1991.

[46] Kazushige Horio and Hisayoshi Yanai, "Numerical Modeling of Heterojunctions Including the Thermionic Emission Mechanism at the Heterojunction Interface," IEEE Trans ED, Vol. 37, No. 4, pp. 1093-1098, 1990.

[47] R. L. Anderson, "Experiments on Ge-GaAs Heterojunctions" Solid-St. Electron. Vol. 5, pp. 341-351, 1962.

[48] William Liu, Damian Costa and J. S. Harris Jr., "Derivation of the Emitter-Collector Transit Time of Heterojunction Bipolar Transistors", Solid-St. Electron. Vol. 35, No. 4, pp. 541-545, 1992.

[49] Jeffrey C. -N. Huang and Ibrahim M. Abdel-Motaleb, "A Comprehensive Non-Quasi-Static Capacitance Model For Graded Heterojunction Bipolar Transistors", Solid-St. Electron. Vol. 36, No. 11, pp. 1583-1592, 1993.

[50] Q. M. Zhang, G. L. Tan, Jing Ming Xu and D. J. Day, "Current Gain and Transit-Time Effects in HBT's with Graded Emitter and Base Regions", IEEE Electron Device Lett. Vol. 11, No. 11, pp. 508-510, 1990.

[51] Juin J. Liou, Lee L. Liou, Chern I. Huang and Burhan Bayraktaroglu, "A Physics-Based, Analytical Heterojunction Bipolar Transistor Model Including Thermal and High Current Effects," IEEE Trans ED, Vol. 40, No. 9, pp. 1570-1577, 1993.

[52] Haosheng Zhou and D. L. Pulfrey, "Computation of Transit and Signal Delay Times for the Collector Depletion Region of GaAs-Based HBTs", Solid-St. Electron. Vol. 35, No. 1, pp. 113-115, 1992.

[53] Riichi Katoh and Mamoru Kurata, "Self-Consistent Particle Simulation for (AlGa)As/GaAs HBT's Under High Bias Conditions," IEEE Trans ED, Vol. 36, No. 10, pp. 2122-2128, 1989.

[54] James J. Chen, Guang-Bo Gao, Jen-Inn Chyi and Hadis Morkoç, "Breakdown Behavior of GaAs/AlGaAs HBT's," IEEE Trans ED, Vol. 36, No. 10, pp. 2165-2171, 1989.

[55] J. J. Liou, "Modeling the Cutoff Frequency of $Al_xGa_{1-x}As$/GaAs/GaAs Heterojunction Bipolar Transistors with Proton-Implanted Collector Region", Solid-St. Electron. Vol. 33, No. 10, pp. 1329-1331, 1990.

[56] J. S. Yuan, "Modeling the Current-Dependent f_t for AlGaAs/GaAs Heterojunction Bipolar Transistor Design", Solid-St. Electron. Vol. 34, No. 10, pp. 1103-1107, 1991.

[57] William Lui, Damian Costa and J. S. Harris Jr., "A Simplified Model for the Distributed Base Contact Impedance in Heterojunction Bipolar Transistors", Solid-St. Electron. Vol. 35, No. 4, pp. 547-552, 1992.

[58] Guang-Bo Gao, David J. Roulston and Hadis Morkoç, "Is Npn or Pnp the Better Choice for Millimeter-Wave AlGaAs/GaAs Heterojunction Bipolar Transistors ?", Solid-St. Electron. Vol. 33, No. 9, pp. 1209-1210, 1990.

[59] David B. Slater, Jr., Paul M. Enquist, Fayez E. Najjar, Mary Y. Chen, James A. Hutchby, Arthur S. Morris and Robert J. Trew, "Experimental Values for the Hole Diffusion Coefficient and Collector Transit Velocity in P-n-p AlGaAs/GaAs HBT's", IEEE Electron Device Lett. Vol. 12, No. 2, pp. 54-56, 1991.

[60] David B. Slater, Jr., Paul M. Enquist, Mary Y. Chen, James A. Hutchby, Arthur S. Morris and Robert J. Trew, "Millimeter-Wave AlGaAs/GaAs P-n-p HBT", IEEE Electron Device Lett. Vol. 12, No. 7, pp. 382-384, 1991.

[61] J. S. Yuan, "High Performance P-n-p Heterojunction Bipolar Transistor Design", Solid-St. Electron. Vol. 34, No. 12, pp. 1347-1352, 1991.

[62] William Liu and Changhong Dai, "An Advantage of Pnp over Npn AlGaAs/GaAs Heterojunction Bipolar Transistors for Microwave Power Applications," Jpn. J. Appl. Phys., Vol. 31, No. 4B, pp. 452-454, 1992.

[63] C. L. Allyn, A. C. Gossard and W. Wiegmann, "New rectifying semiconductor structure by molecular beam epitaxy", Appl. Phys. Lett. Vol. 36, No. 5, 1980.

[64] W. G. Oldham and A. G. Milnes, "Interface States in Abrupt Semiconductor Heterojunctions", Solid-St. Electron. Vol. 7, pp. 153-165, 1964.

[65] L. L. Chang, "The Conduction Properties of Ge-$GaAs_{1-x}P_x$ *n-n* Heterojunctions", Solid-St. Electron. Vol. 8, pp. 721-728, 1965.

[66] C. M. Wu and E. S. Yang, "Carrier Transport Across Heterojunction Interfaces", Solid-St. Electron. Vol. 22, pp. 241-248, 1979.

[67] Ambitabh Chandra and Lester F. Eastman, "A Study of the Conduction Properties of a Rectifying nGaAs-n(Ga,Al)As Heterojunction", Solid-St. Electron. Vol. 23, pp. 599-603, 1980.

[68] Gregory B. Tait and Charles R. Westgate, "Electron Transport in Rectifying Semiconductor Alloy Ramp Heterostructures," IEEE Trans ED, Vol. 38, No. 6, pp. 1262-1270, 1991.

[69] "*Gallium Arsenide Materials Devices and Circuits*," edited by M.J. Howes and D.V. Morgan, John Wiley & Sons, 1985.

[70] "*Properties of Gallium Arsenide*," INSPEC, Unwin Brothers, 1986.

[71] Michael Shur, "*GaAs Devices and Circuits*," Plenum Press, 1987.

[72] Neil Sclater, "*Gallium Arsenide IC Technology Principles and Practice*," Tab Books, 1988.

[73] David C. Look, "*Electrical Characterization of GaAs Materials and Devices*," John Wiley & Sons, 1989.

[74] "*GaAs Technology and Its Impact on Circuits and Systems*," edited by D. Haigh and J. Everard, IEE 1989.

[75] Marc H. Brodsky and A.R. Peaker, *Properties of Gallium Arsenide*, 2nd Edn, INSPEC, London and New York, 1990.

[76] Madjid E. Hafizi, Clarence R. Crowell, Leszek M. Pawlowicz and Michael E. Kim, "Improved Current Gain and f_t Through Doping Profile Selection in Linearly Graded Heterostructure Bipolar Transistors," IEEE Trans ED, Vol. 37, No. 8, pp. 1779-1787, 1990.

[77] P. M. Asbeck, Mau-Chung F. Chang, J. A. Higgins, N. H. Sheng, G. J. Sullivan and Keh Chung Wang, "GaAlAs/GaAs Heterojunction Bipolar Transistors, Issues and Prospects for Application," IEEE Trans ED, Vol. 36, pp. 2032-2041, 1989.

[78] Hiang-Cheong Chan and Tsay-Jiu Shieh, "A Three Dimensional Semiconductor Device Simulator for GaAs/AlGaAs Heterojunction Bipolar Transistor Analysis," IEEE Trans ED, Vol. 38, No. 11, pp. 2427-2432, 1991.

[79] Chushirou Kusano, Hiroshi Masuda, Kazuhiro Mochizuki, Masahiko Kawada and Katsuhiko Mitani, "The Effect on Turn-On Voltage (V_{BE}) of AlGaAs/GaAs HBT's due to the Structure of the Emitter-Base Heterojunction," Jpn. J. Appl. Phys., Vol. 29, No. 8, pp. 1399-1402, 1990.

[80] Madjid Hafizi, Robert A. Metzger, William E. Stanchina, David B. Rensch, Joseph F. Jensen and William W. Hooper, "The Effects of Base Dopant Diffusion on DC and RF Characteristics of InGaAs/InAlAs Heterojunction Bipolar Transistors," IEEE Electron Device Lett., Vol. 13, No. 3, pp. 140-142, 1992.

[81] E. J. Prinz, P. M. Garone, P. V. Schwartz, X. Xiao and James C. Sturm, "The Effects of Base Dopant Outdiffusion and Undoped $Si_{1-x}Ge_x$ Junction Spacer Layers in $Si/Si_{1-x}Ge_x/Si$ Heterojunction Bipolar Transistors," IEEE Electron Device Lett., Vol. 12, No. 2, pp. 42-44, 1991.

[82] Dwight C. Streit, Majid E. Hafizi, Donald K. Umemoto, J.R. Velebir, Liem T. Tran, Aaron K. Oki, Michael E. Kim, Shing K. Wang, C.W. Kim, Larry P. Sadwick and R.J. Hwu, "Effect of Exponentially Graded Base Doping on the Performance of GaAs/AlGaAs Heterojunction Bipolar Transistors," IEEE Electron Device Lett., Vol. 12, No. 5, pp. 194-196, 1991.

[83] Koki Saito, Makoto Konagai and Kiyoshi Takahashi, "Theoretical Analysis of Heavy Doping Effects on AlGaAs/GaAs HBT's," Jpn. J. Appl. Phys., Vol. 29, No. 10, pp. 1900-1907, 1990.

[84] Kazuhiro Mochizuki, Shigeo Goto, Hiroshi Kakibayashi and Chuushiro Kusano, "Substrate Misorientation Effect on Be Transport during MBE Growth of GaAs ," Jpn. J. Appl. Phys., Vol. 29, No. 7, pp. 1235-1239, 1990.

[85] Kazuhiro Mochizuki, Seiichi Isomae, Hiroshi Masuda, Tomonori Tanoue and Chuushiro Kusano, "Stress Effect on Current Induced Degradation of Be-Doped AlGaAs/GaAs Heterojunction Bipolar Transistors ," Jpn. J. Appl. Phys., Vol. 31, Part 1, No. 3, pp. 751-756, 1992.

[86] Yang-Hua Chang and G. P. Li, "Resolving Degradation Mechanisms in Ultra-High Performance N-p-n Heterojunction Bipolar Transistors," IEEE Trans ED, Vol. 40, No. 4, pp. 692-696, 1993.

[87] Shin-ichi Tanaka, Hidenori Shimawaki, Kensuke Kasahara and Kazuhiko Honjo, "Characterization of Current-Induced Degradation in Be-Doped HBT's Based in GaAs and InP," IEEE Trans ED, Vol. 40, No. 7, pp. 1194-1201, 1993.

[88] L. F. Luo, H. L. Evans and E. S. Yang, "A Heterojunction Bipolar Transistor with Seperate Carrier Injection and Confinement," IEEE Trans ED, Vol. 36, No. 9, pp. 1844-1846, 1989.

[89] X. Wu, Y. Q. Wang, L. F. Luo and Edward S. Yang, "An AlGaAs/GaAs Heterostructure-Emitter Bipolar Transistor," IEEE Electron Device Lett., Vol. 11, No. 6, pp. 264-266, 1990.

[90] Wen-Chau Liu and Wen-Shiung Lour, "AlGaAs/GaAs Heterostructure-Emitter Bipolar Transistor (HEBT) Prepared by Molecular Beam Epitaxy", Solid-St. Electron. Vol. 34, No. 7, pp. 717-722, 1991.

[91] Wen-Shiung Lour, Wen-Chau Liu and Yeong-Her Wang, "Investigation of Heterostructure-Confinement-Emitter Transistors", Solid-St. Electron. Vol. 35, No. 2, pp. 117-124, 1992.

[92] H. R. Chen, C. P. Lee, C. Y. Chang, K. L. Tsai and J. S. Tsang, "Evidence of Zero Potential Spike Energy in AlGaAs / GaAs Heterostructure Emitter Bipolar Transistors ," Jpn. J. Appl. Phys., Vol. 32, Part 2, No. 10A, pp. 1397-1399, 1993.

[93] S. -P. Lee and D. L. Pulfrey, "Modelling the d.c. Performance of GaAs Homojunction Bipolar Transistors", Solid-St. Electron. Vol. 29, No. 7, pp. 713-723, 1986.

[94] X. Correig, J. Calderer, E. Blasco and R. Alcubilla, "Comments on the Use of the Surface Recombination Velocity Concept", Solid-St. Electron. Vol. 33, No. 5, pp. 477-484, 1990.

[95] S. M. Sze, *Physics of Semiconductor Devices*, 2nd Edn, Wiley-Interscience, New York, p. 126 (1981).

[96] S. I. Cserveny, "Potential distribution and capacitance of abrupt heterojunctions", Int. J. Electron. Vol. 25, No. 1, pp. 65-80, 1968.

[97] William C. Rutherford, "Comparative Modelling of Current Gain and Cutoff Frequency for Heterostructure Confinement and Heterojunction Bipolar Transistors", Solid-St. Electron. Vol. 37, No. 10, pp. 1783-1785, 1994.